Continuous and Forced Dynamic Operation to Achieve Kinetically Controlled Crystallization

by

JACOB CLYDE CRISLIP

Submitted to the Graduate School of

WORCESTER POLYTECHNIC INSTITUTE

in partial fulfillment of the requirements for the degree of

DOCTOR OF PHILOSOPHY

November 2023

Department of Chemical Engineering

Approved as to style and content by:

Dr. Andrew R. Teixeira, Advisor
Chemical Engineering, WPI

Dr. N. Aaron Deskins, Member
Chemical Engineering, WPI

Dr. Michael Timko, Member
Chemical Engineering, WPI

Dr. Wei Fan, Member
Chemical Engineering, UMass Amherst

ACKNOWLEDGEMENTS

First, my deepest gratitude goes to my loving partner, Debbie Tran. Much like the marathon I ran back in 2019, none of this would have been possible without her love and support at every step of the way. She pushed me to always try my hardest while making sure I always kept my physical and mental health as a top priority. As I conclude my PhD, I am grateful for how much we have both grown as individuals and as a team over the last five years and am excited to see where our future takes us.

Next, my family deserves thanks for always keeping me grounded and reminding me there is life outside of grad school. Being able to do my PhD alongside watching my nieces grow up has been a privilege that I'll never forget.

A special thank you must go out to my advisor, Prof. Teixeira, for refining my approach to solving the world's problems. Rather than approach learning from an exploratory perspective, his training has engrained in me the principle that every discovery should be built on a hypothesis driven argument that can be boiled down to a clear set of causes and effects. This has helped tremendously in turning around Chapter 4 in the span of a few days. He once told me by the end of my PhD I should be able to look back on the five years of work and be confident that I could complete it in one… I took this to the extreme and did it in four months.

Thank you to my committee members for your patience along the way as these last few months have not been conventional. Your support over these last five years has helped me hone my focus to become a better scientist as I enter the world of industrial research.

To Cam and Heather, my Day 1's: Now that I stand at the threshold of post graduate life, I think back on what a journey it's been and want you both to know how much you inspire me to put my best foot forward in everything I do. We have cut our teeth for the past five years, and now each of us has our own prize to show for it. I look forward to meeting you both on the other side to celebrate.

To keep it brief because there are so many of you: CEGO has been a foundational component of my grad school experience. Watching this community grow over my time at WPI and knowing that I had a direct role in it is an honor that I take seriously. I'm so proud of each and every one of you, specifically not in the work you do but the people you're becoming. You are good, kind people who look out for each other, and you have made my life better having met you.

To Doug, Ian, Alex, Geoff, Tiffany, and Justina (and anyone else on faculty and staff I have met along the way), thank you for always being there to lend a helping hand in a time of need. You guys keep the metaphorical roof above our heads, and I am confident that I would have been completely lost along the way without your help.

To everyone, this is our triumph, and I am proud to share it with you.

ABSTRACT

Crystallization is a vital step in nearly every field of chemical manufacturing including production of refinery catalysts, isolation of active pharmaceutical ingredients, and purification of specialty materials. While centuries of research have defined what crystals are down to the atomic level, the field continues to be challenged by the fundamental questions of what physical and chemical pathways occur during synthesis, why certain morphologies are favored over others, and how these processes and properties can be controlled. In particular, the common thread in each of these barriers is the ambiguity in scaling relationships from the formation of a single crystal to the macroscopic behavior throughout the body of the crystallizer. This work answers each of these questions through the lens of reaction engineering by transforming the way crystallization is performed. Rather than synthesizing individual batches that are prone to nonuniform internal conditions, the cutting-edge reactor designs described herein demonstrate how highly reproducible crystals can be made continuously using segmented flow microfluidics. Each self-contained microdroplet acts as a mobile batch reactor whose temperature can be rapidly and isothermally changed by virtue of fast heat and mass transfer at the minimized length scale. These near step changes in reaction environment unlock operating regimes that would otherwise be impossible. Quickly oscillating between hot and cold environments prevents the system from reaching equilibrium, and this work proves through population balance modeling that operating within this kinetically limited window facilitates the inverse ripening of seed crystals into highly monodisperse fine crystallites. This approach to continuous bottom-up crystallization substitutes the numerous unit operations typically required in traditional crystallizers for an elegant continuous reactor design that eliminates wasted material and excessive solvents.

TABLE OF CONTENTS

TABLE OF FIGURES

TABLE OF TABLES

CHAPTER 1

INTRODUCTION

Classical crystallization occurs through simultaneous nucleation and growth, which together competitively deplete supersaturation driving the system toward equilibrium. This work details a series of studies that reveal highly transient behavior within kinetically limited operating windows. Each case demonstrates unique instances in which kinetically favored products could be isolated before their thermodynamically favored counterparts could be formed. This kinetic locking was achieved by imposing dynamic operating conditions that slowed or completely prevented the system from reaching equilibrium. It is shown in each study that micro-scale crystallization is the key to accessing these operating windows as fast heat and mass transfer allow for near step changes in temperature and facilitate uniform reaction environments.

The following three chapters each focus on a specific approach to crystallization: reactive crystallization via encapsulated sol-gel micro-batches, design and fabrication of fully continuous cooling and sono-crystallization, and crystal ripening through fast thermal oscillations. Zeolites are aluminosilicate microporous crystals that are traditionally synthesized in autoclave batch reactors. By constructing a series of reactors that experience different rates of heat transfer, we demonstrated that the initial nucleation reaction is heavily limited by heat transfer highlighting the dangers of nonuniform reaction environments and uncontrolled kinetics. A regime map for reactive crystallization was then constructed from theoretical calculations and validated with experimental results to develop criteria for fast and predictable crystallization kinetics. These principles were then applied to the design of a flow crystallizer capable of resolving concentration and crystal habit within single microdroplets in flow using in situ UV-Vis spectroscopy and optical microscopy. Lastly, a population balance modeling study revealed how periodically shifting temperature in a well-mixed crystallizer can produce different outcomes based on the amount of time the system spends in either the hot or cold environment. The key lessons learned from these experiments are recapitulated in a final reflection section before concluding the thesis with a look toward the future of STEM education. As the field of crystallization and chemical engineering at large expands, our ability to train the next generation of engineers and researchers must evolve as well to match the challenge.

CHAPTER 2

DOMINANCE OF HEAT TRANSFER LIMITATIONS IN CONVENTIONAL SOL-GEL SYNTHESIS OF LTA REVEALED BY MICROCRYSTALLIZATION

2.1 ABSTRACT

The non-classical nucleation and growth mechanism for hydrothermal zeolite synthesis is a complex convolution of thermodynamic phase transformations, kinetic chemical condensations, three-phase mass transfer and spatial-temporal thermal gradients. The process is typically studied in batch autoclaves heated with laboratory ovens before being scaled in high temperature batch crystallizers. The experimental and theoretical work presented here contests that elucidation of the underlying crystallization mechanism and the ability to achieve kinetically controlled, scalable crystallization requires careful consideration of transport limitations which dominate the batch process. A segmented microdroplet crystallizer is used to remove internal and external heat transfer gradients during the synthesis of LTA zeolite crystals. The heat transfer regimes are carefully mapped, and specific criteria are established for overcoming thermal limitations.

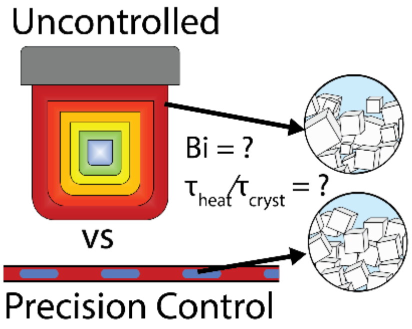

Figure 2.1: Graphical abstract detailing the contrast between the internal environments and outputs of traditional batch crystallizers with those of a microdroplet crystallizer specifically raising the question of the scalability of heat transfer and reaction kinetics.

2.2 INTRODUCTION

Zeolites are microporous crystalline aluminosilicates that have been widely used as molecular sieves, catalysts and sorbents for nearly a century in a variety of industrial and consumer applications. Tetrahedrally coordinated silica and alumina centers form repeated networks of molecular rings that result in highly-ordered nanometer-sized channels and cages with extremely high surface area.[1] While all zeolite crystals are technically metastable, the careful control over the crystallization environment including the use of organic structure directing agents (SDAs) and multiphase sol-gel syntheses have enabled researchers to create laboratory environments that can form 253 unique frameworks.[2]

Over 50 years of research has illuminated phenomenological pathways for zeolite crystallization, including foundational works by Mobil Research Labs[3,4] and Union Carbide[4], seminal works by Tsapatsis[5–8], Davis[9–11], Corma[12–15], Vlachos[16,17], Thompson[18,19], and recent works by Roman[15,20] and Rimer[20–22]. There are markedly fewer studies into the kinetics of the rate limiting steps in this process, as it is extremely challenging to measure the individual events involved in the non-classical nucleation and growth. Among other reasons, this is owing to the fact that elementary events are often convoluted with both transients and local gradients in heat and mass transfer at both the macroscopic reactor-level and microscopic molecular-level environments. This has led to an active debate in the community as to the role of aging[23–25], effect of mixing[25–27], contributions from epitaxial molecule-by-molecule versus colloidal agglomerate-mediated growth[25–29], and recently, whether condensed materials can rearrange into structured materials post synthesis.[29,30]

Crystallization is driven by the formation, delivery, and incorporation of molecular building blocks within the sol-gel process. As the aluminosilicate gel dissolves, the constituent ions oligomerize via condensation reactions.[31] Nanoparticle aggregates and agglomerates are then stabilized by electrostatic and van der Waals interactions according to DLVO theory.[16] Scattering and microscopy work by Kumar et al. confirms the formation of key amorphous “worm-like particle” (WLP) intermediates from these colloidal precursors.[32] Precursor composition, atomic arrangement, and kinetic behavior change over the course of both aging and crystallization until the system reaches a metastable equilibrium state.[33] The fate of the final zeolite framework is determined by the collective history of the multiphase reaction mixture, and this layered complexity has led to zeolite synthesis often being regarded as an art rather than a science.[22]

Classical nucleation theory suggests the rate at which precursors are incorporated at the crystal surface follows an Arrhenius temperature dependence.[34] Therefore, reactor heating must be rapid to minimize both spatial and temporal temperature gradients that drive nonuniform crystallization rates.[35] Maintaining isothermal operation reduces product heterogeneity and pinpoints the formation of the various morphologies present over the course of the synthesis.[36] Traditional autoclave batch reactors are plagued with slow heat up times, and in situ visualization of reactor contents is often difficult.[37] In contrast, tubular microfluidic reactors are ideal for removing transport limitations making it possible to discern between intrinsic reaction kinetics and transport limitations with respect to observed reaction rates.[38] In segmented flow microcrystallization, microdroplets are dispersed into an inert medium allowing for each microdrop to experience identical reaction conditions across exponentially shorter diffusional length scales, effectively eliminating heat delay.[39] Kinetically-limited micro-scale syntheses will more accurately reflect simulation models and uncover the chemical pathways for converting amorphous aluminosilicates to zeolites.

We propose that the use of large batch autoclaves for the study of mechanistic growth is contributing to the conflicting and shifting mechanistic theories as they allow for temporal and spatial gradients in crystallization environment for both concentration and temperature. Despite the extensive mechanistic research into how zeolites form, there remains an apparent deficiency in our quantitative understanding of the thermal and mass transport effects that dominate the synthesis. The typical batch synthesis using template-free approaches is conducted under hydrothermal conditions (50 – 300 °C and autogenous 1-100 bar) in 10-1000 mL autoclaves placed within a well-controlled laboratory oven. The solution then undergoes a series of aging, nucleation and growth stages with potential species additions, heating cycles or induction times pursuant to the particular recipe. Moreover, the lack of one-to-one correspondence between SDA and product zeolite across synthesis recipes contributes variability and ambiguity. This results in a dynamic environment that contains reaction transients in temperature and concentration as the reactor is first heated then as the reagents are consumed into the solid/crystal phase. The following work will outline a strategy that uses segmented flow microdroplets to remove these heat transfer limits and identifies criteria needed to overcome transport limitations during batch zeolite synthesis.

2.3 MATERIALS AND METHODS

2.3.1 PRECURSOR PREPARATION

All raw material reagents were used as received for sol-gel synthesis of Linde type A (LTA) zeolite with stoichiometric composition $\mathbf{1\,SiO_2 : 1.41\,Al_2O_3 : 9.30\,NaOH : 135\,H_2O}$ as described by Yu et al.[40] A 3.8 M solution was prepared by dissolving 9.14 g of anhydrous sodium hydroxide pellets ($\mathbf{NaOH}$, ≥ 97 %, MilliporeSigma, CAS: 1310-73-2) in 60 mL of deionized water. Silica and alumina feedstocks were each prepared by dissolving 3.00 g of sodium metasilicate (Na_2O_3Si, MilliporeSigma, CAS: 6834-92-0) and 6.44 g of sodium aluminate ($Na_2OAl_2O_3$, ≥ 99.95 %, MilliporeSigma, CAS: 11138-49-1), respectively, into 30 mL volumes of the prepared sodium hydroxide solution. Equal volumes of silica and alumina were slowly combined according to the reactor scale being tested taking care to preserve the integrity of the gel while ensuring sufficient contact between the solid and liquid phases. The static sol-gel mixture then aged at room temperature for 12 hours.

2.3.2 REACTOR DESIGN

Traditional batch reactions were performed in sealed 50 mL polypropylene bottles at ambient pressure containing approximately 10 mL of sol-gel and allowed to crystallize in a conventional laboratory oven (Cole Parmer Laboratory Oven, Model 5015-50), convective oven (HP 5890 Series GC System) or recirculating water bath (Thermo Electron, Autorefill). Tubular micro-batch reactors were constructed from 0.125 inch outside diameter (0.03 inch wall thickness) perfluoroalkoxy tubing (PFA 350 Grade, Swagelok, P/N PFA-T2-030-100) and IDEX flat-bottom flangeless fittings. Fluids were loaded into BD 60 mL Luer-Lok syringes and fed to the microdroplet generator by a concentric tube-in-tube nozzle design by two Harvard Apparatus PHD ULTRATM syringe pumps. Transfer lines were primed with mineral oil to remove all air bubbles and form a protective oil layer on the walls ($C_{16}H_{10}N_2Na_2O_7S_2$, Pure, Acros Organics, 8042-47-5).[40] The reagents flowed through a sequence of PFA tubing, stainless steel needle (Air-Tite Products Co., Inc., 22G x 4”, sealed with Marathon Septa, Shimadzu, item no. 239488), and IDEX PEEK assemblies (Tee Assembly PEEK for 1/8” OD, 0.62” thru hole, Cross Assembly PEEK 0.050” thru hole) while the droplet generator (Figure 2.2) was submerged in a Branson 2200 (BRANSONIC® Ultrasonic Cleaner, B-2200R-4) ultrasonication water bath to prevent solid deposition and accumulation. Silica (annular space) and alumina (inside needle) feedstocks were separately fed at equal flow rates (0.2 mL/min each) to the droplet generator where two perpendicular oil streams (0.6 mL/min each) sheered them together into 1.7 µL ± 0.275 µL microdroplets (Appendix 1 Figure A1.5). Once droplet generation reached steady state, a designated 1 m length of tubing was filled with sol-gel microdroplets where it was then allowed to age for 12 hours before being placed into the heat source at time t = 0.

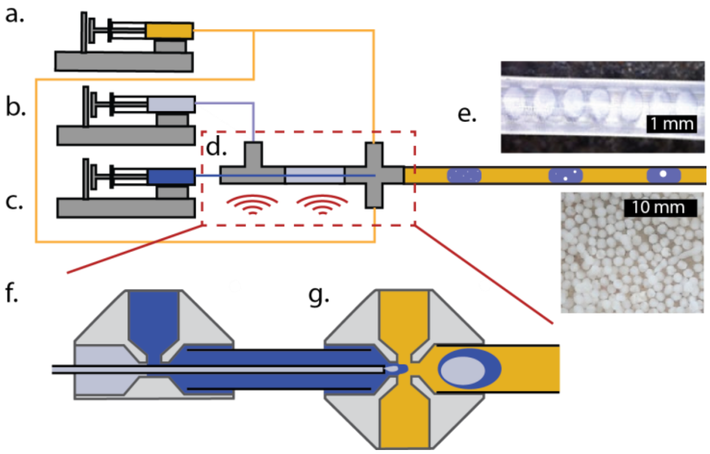

Figure 2.2: Microdroplet generation was achieved by combining (b) silica and (c) alumina precursors in a micro-tee (d,f) before shearing the combined droplet into a continuous oil phase (a) in a micro-cross (g). The final dispersed droplets (inlay micrographs) were collected in a microreactor tube (e).

2.3.3 CRYSTALLIZATION AND WORKUP

Upon completion of the aging cycle, reactors were submerged in their respective heating media (t = 0) and allowed to progress until a designated end time for workup to construct time-resolved crystallinity curves. Upon removal from the respective heating medium, each reaction mixture was immediately quenched with 50 mL of deionized water to rapidly reduce supersaturation, pH, and temperature. To account for the large sample volume and high pH, batch samples were further diluted into six 50 mL centrifuge tubes (1” diameter, 4.5” length) for a total wash volume of 300 mL. Samples were spun down at 1400 rpm for 20 minutes using a Sorvall Legend RT+ centrifuge, the supernatant was decanted, and the samples were washed twice more until the pH was below 9. Once recombined in a single tube, the solids underwent a final 50 mL wash and spin, and were collected in a covered glass PYREX® dish and dried overnight in a 65 °C oven. Five full 1 m long microdroplet tubes were collected for each reaction time sample and combined during the quenching step to ensure a sufficient product volume for SEM, physisorption, and XRD. Micro-batch syntheses were run in duplicate, while traditional batch-scale syntheses were run in triplicate. Characterization results of these sample trials were averaged, and descriptive statistics were calculated.

2.3.4 HEAT UP TIMES

Heat transfer effects were measured by comparing induction times, growth rates, and intermediate particle size distributions for the given synthesis recipe in response to varying reactor length scales and heating rates. External heating rates varied with the conductivity and convection of heating fluid with each set at 65 °C: recirculating water bath, convection oven, and natural convection oven. Heat up profiles were measured for each crystallization configuration by immersing 1/16" Type K thermocouple in the center of the crystallizer filled with deionized water as a model fluid. A thermocouple was fed through the cap of the polypropylene bottle and submerged in the water to simulate the batch reactor heat up. Similarly, a thermocouple was fed into a portion of water-filled PFA tubing and submerged in the corresponding heating media. The corresponding transient temperatures were recorded.

2.3.5 CHARACTERIZATION

X-ray diffraction (XRD) was performed using a Rigaku diffractometer with the Bragg-Bretano theta-theta configuration and a B PANalytical Empyrean x-ray diffractometer. Diffractions were taken with a Cu Kα at 37.5 kV and 25 mA and with a Cr Kα at 30 kV and 55 mA, respectively. Analysis was performed over 2θ range from 5°-35° with a 0.05° step size and 1 s dwell time, and over 2θ range from 10°-50° with a 0.03° step size and 15.24 s time per step, respectively. Reflectance data collected using Cr Kα radiation were later converted to Cu Kα radiation for uniform presentation. Percent crystallinity as calculated by summation of integrated intensities of diffraction peaks corresponding to reflections of (222), (420), (442), (620), (642), and (644) crystal planes. Each reflectance pattern and crystallinity measurement were normalized against a fully crystalline reference sample as specified by ASTM method D 5357-03.

N_2 physisorption was performed using an ASIQ iQ Quantachrome Instrument to determine BET surface area, pore size, and micropore volume. A sample mass of ~ 0.10 g was added to a glass bulb, and the sample was degassed following a temperature ramp of 2 °C min-1 with 15-minute temperature holds at 60, 80, 100, and 120 °C before increasing to 350 °C, where the temperature was maintained for 5 hours. The analysis procedure dosed N_2 as the adsorbate into the sample cell cooled with liquid N_2 and obtained 60 isothermal P/P0 points ranging from 1.41×10-4 to 1 followed by 15 desorption points between P/P0 of 1 to 0.1. BET surface area was determined by applying the t-plot method to model the adsorption isotherm between P/P0 of 0.05 to 0.3. Pore size and micropore volume were determined by applying the t-plot method to model the adsorption isotherm between P/P0 of 0.001 to 0.1.

Select LTA samples from each reactor system were analyzed using an A JSM 7000F scanning electron microscope operating at an accelerating voltage of 10 kV. Powder samples were ground using a mortar and pestle, oven-dried overnight, coated in gold, and mounted using double-sided carbon tape. Particle size distributions and corresponding descriptive statistics were calculated using ImageJ software to measure Feret diameters at 10,000x magnification.

2.4 RESULTS

The primary results presented in this work are the time-resolved crystallographic and textural properties of LTA powders obtained from the batch or microbatch hydrothermal synthesis with each of the three heating modes. Heating modes for each reactor were first characterized to establish their heat transfer rates. The transient heat up curves were measured at the center of each reactor and are shown in Figure 2.3 for each reactor placed into the oven, convection oven and recirculating bath. The experimental temperature profiling demonstrates a bounded exponential decay with asymptotic temperature approaching the heat source set point. The corresponding model fits were performed by least square regression of the exponential heat conduction model in equation 1 (see Appendix 1 for derivation) to determine the time constants for heating.

$$\frac{\bar{T}(t)-T_{\infty}}{T_i-T_{\infty}} = C \exp\left[-\frac{t}{\tau_{heat}}\right] \qquad (1)$$

Where $T_{\infty} = 65\ °C$ is the setpoint temperature, $T_i = 20\ °C$ is the initial fluid temperature, C is a pre-exponential describing the temperature driving force and contributions from internal gradients, and τ is the experimentally fit heat up time constant. The resulting radial-averaged temperature, $\bar{T}(t)$ is then fit to the experimental data.

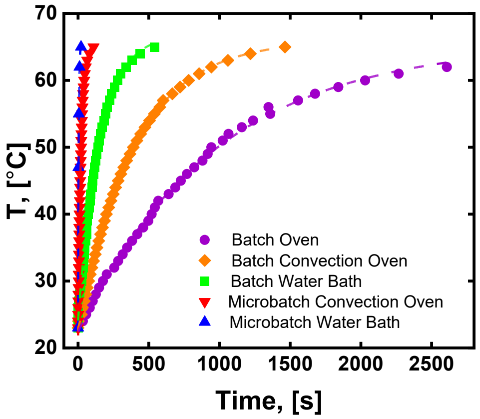

Figure 2.3: Heat up profiles showing progressively faster heat transfer rates in micro-batch crystallizers and with convective water heating. Exponential fits (dashed lines) define the characteristic heat up time constant.

The characteristic times followed the anticipated trend where the smallest characteristic lengths and fastest external heat transfer modes achieved the most rapid heat up: $\tau_{\mu} < \tau_{batch}$ and $\tau_{bath} < \tau_{conv} < \tau_{oven}$, respectively.

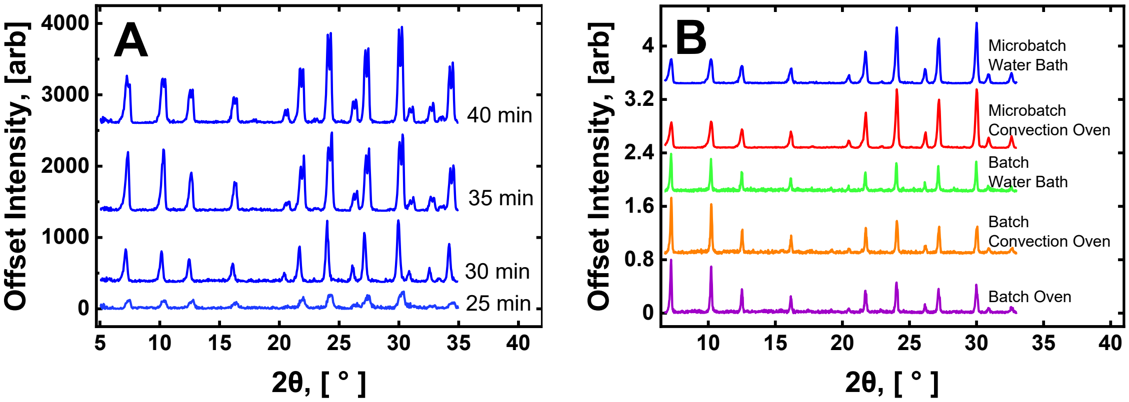

Figure 2.4A: Time progression of XRD patterns of microbatch bath crystallized LTA.
Figure 2.5B: Final XRD patterns for all reactor scales and heating modes demonstrating complete crystallinity to pure LTA at long times.

The raw XRD patterns for all experimental runs are shown in Appendix 1 Figure A1.2. Characteristic patterns demonstrating the temporal progression are shown here in Figure 2.4A for the fastest case, the micro-batch bath. An amorphous solid was observed throughout the initial induction period before small crystalline peaks were first observed at t = 25 min. A rapid progressive sharpening of the peaks then occurred as crystallization time increases over the next 15 minutes until complete crystallinity was observed. This same trend is observed in all heating modes. The location and relative intensities of all major reflections were consistent with the LTA framework, showing minimal presence of other crystalline frameworks such as FAU or SOD, especially in the final time samplings for all reactor configurations (Figure 2.4B).

The extent of crystallinity was measured by ratioing intensities at characteristic reflections to a reference standard as described earlier using standard methods. The relative crystallinity was then plotted versus crystallization time in **Figure 2.6**, normalized to the fully crystalline standard.

A typical S-shaped crystallization curve captured the transformation from amorphous aluminosilicate to crystalline zeolite. Classical nucleation theory identifies key regions of the S curve as induction and growth. Induction periods begin at time $t = 0$ and conclude at the first detection of crystallinity[34], $t_0 = 20 - 45$ minutes in this study. Notably, the induction period was narrowly defined in the microbatch systems with crystallization curves showing excellent reproducibility. The batch systems, however, required longer induction periods that were more stochastic in nature before triggering the similar rapid crystallization profile, as visualized by the more substantial error bars in **Figure 2.6**.

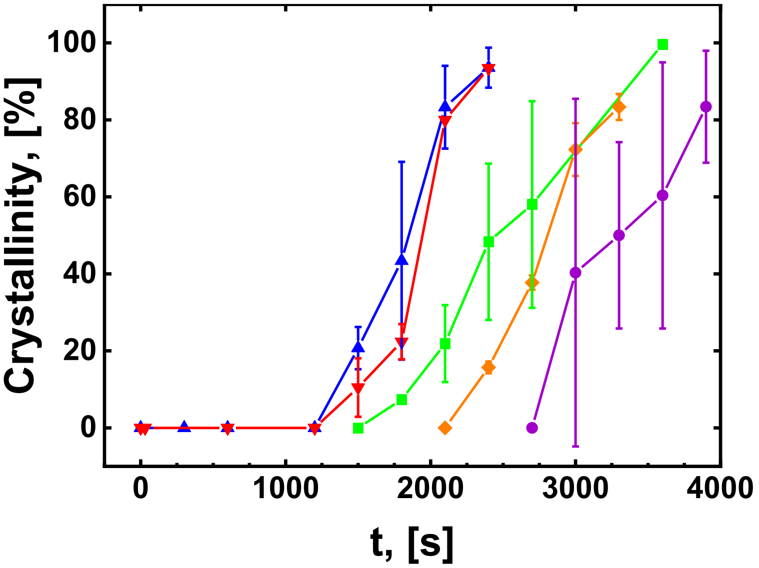

Figure 2.6: Transient crystallinity curves show shorter induction periods and faster overall crystallization by eliminating heat transfer limitations in micro-batch reactors. Batch oven (●), batch convection oven(◆), batch water bath (■), microbatch convection oven (▼), microbatch water bath (▲).

For greater kinetic understanding, growth rates were quantified using the Avrami equation[41]: $\alpha = 1 - e^{-k(t-t_0)^n}$, where α is the transformed fraction or crystallinity, k is the growth rate constant, and n is the mechanistic parameter. Linearized Avrami plots are shown in

Appendix 1 Figure A1.4 and used to numerically fit the original growth curves. While the proper linear trend was observed for each heating mode, the kinetic parameters varied by many orders of magnitude, further supporting the case in literature that the Avrami model can only be used to describe classical phase change kinetics and fails for the more complex sol-gel synthesis, particularly when convoluted with multiphase mass transfer and thermal gradients.[42,43] In this study, the linearization did serve useful for fitting the S-curve to determine the crystallization time t_{50} with greater accuracy than through interpolation (Table 2.2).

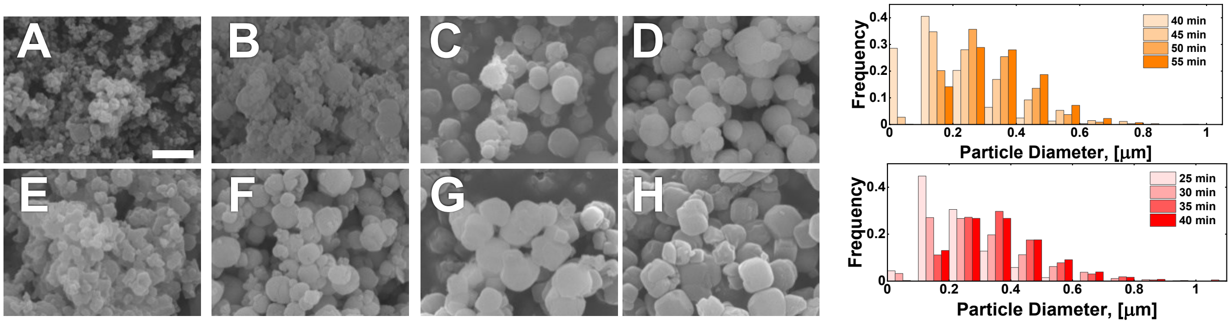

Figure 2.7: SEM micrographs of time progression of batch (top) and microbatch (bottom) LTA crystals in a convective air oven at 65 °C. A-D are batch 40, 45, 50, 55 minutes, respectively. E-H are microbatches 30, 40, 45 and 60 minutes, respectively. 10.0kV, x50,000, 500 nm scalebar. Particle size distributions for each system are shown to the right.

SEMs for batch and microbatch were collected for a number of crystallization times each heating mode, as seen in Figure 2.7. As has been shown previously, the morphology of the batch sample undergoes a transition from amorphous silica to amorphous wormlike particles (WLPs) to fully crystalline, discrete particles. Interestingly, the resulting size distribution was 200-600 nm for all fully crystalized samples, irrespective of configuration, indicating that the particle size distribution may be more sensitive to other parameters, not heat transfer (Figure 2.8).

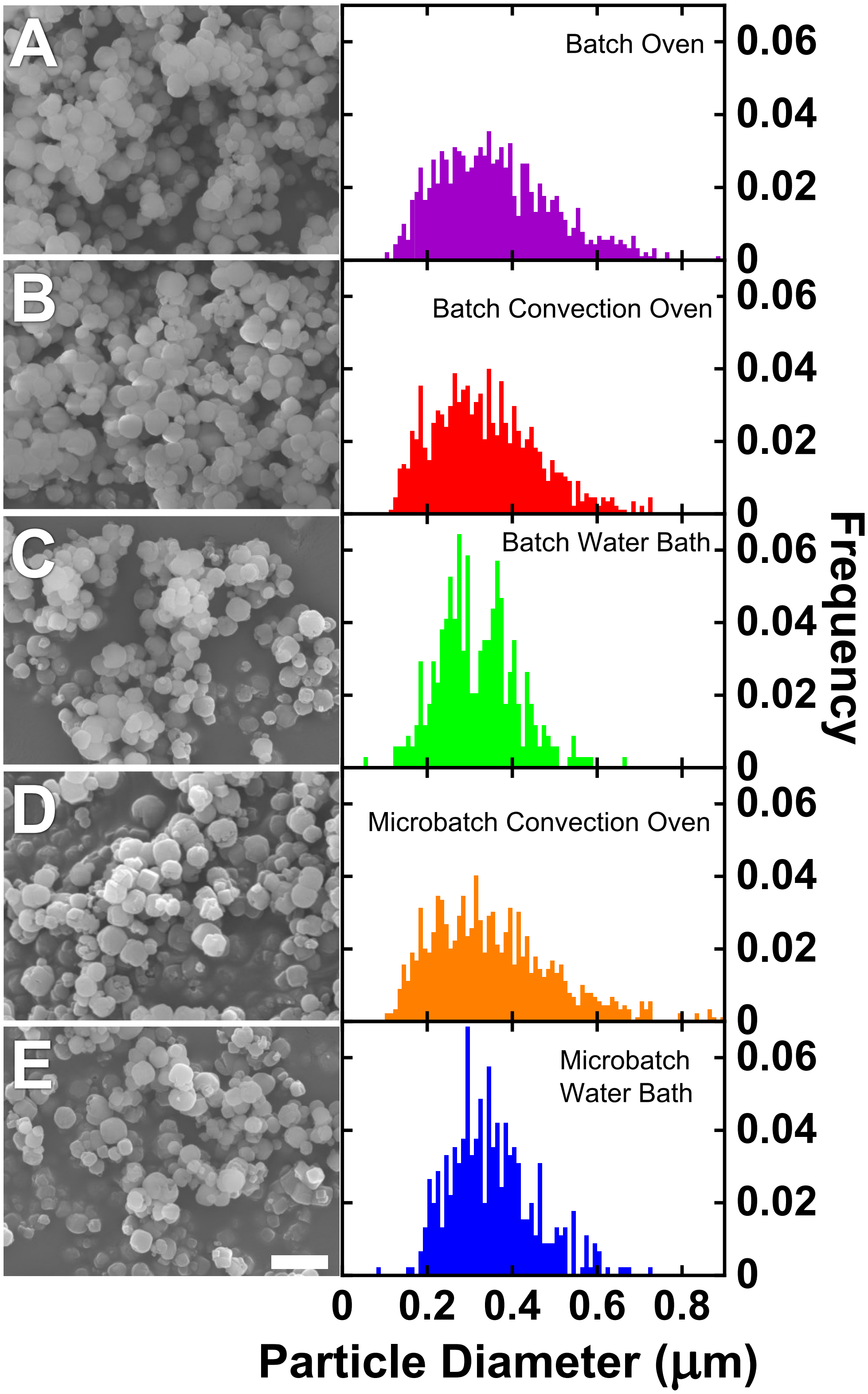

Figure 2.8: SEM micrographs and corresponding particle size distributions of fully crystallized LTA particles for (A) batch oven, (B) batch convection oven, (C) batch water bath, (D) microbatch convection oven, (E) microbatch water bath.10.0kV, x20,000, 1 µm scalebar.

Textural properties for all samples are summarized in **Table 2.1**, with error representing one standard deviation. Samples not reporting a standard deviation were run on a single characteristic sample identified by XRD. Clear time progressions in crystallinity were observed, though this was to the detriment of pore volume and total surface area as the particles transition from amorphous mesoporous WLPs to crystalline LTA framework. While particle size generally increased with the time and crystallinity, no noticeable difference in average particle size or polydispersity were observed when comparing the most crystalline samples from each heating mode, suggesting that heat transfer had little effect on final particle size distributions under the studies conditions.

Table 2.1: Textural properties of synthesized LTA crystals

Time (min)	**Particle Size[a] (nm)**	**BET[b] (m^2/g)**	**Pore Size[b] (nm)**	**Pore Volume[b] (cm^3/g)**	**Crystallinity[c] (%)**
Batch Oven					
50	-	44.8 ± 4.3	1.52 ± 0.04	0.016 ± 0.001	40.3 ± 45.2
55	-	34.6	1.54	0.013	50.0 ± 24.2
60	-	24.8 ± 10.0	1.58 ± 0.02	0.001 ± 0.004	60.4 ± 34.6
65	360 ± 140	19.2	1.62 ± 0.02	0.007	83.4 ± 14.5
Batch Convection					
40	170 ± 110	45.7 ± 0.2	1.61 ± 0.11	0.018 ± 0.001	15.7 ± 1.5
45	270 ± 140	44.0 ± 2.3	1.51 ± 0.05	0.017 ± 0.001	37.7 ±1.9
50	300 ± 110	26.8 ± 3.2	1.58 ± 0.00	0.010 ± 0.001	72.3 ± 6.9
Batch Bath					
30	-	45.1 ± 9.0	1.69 ± 0.20	0.017 ± 0.003	7.3
35	240 ± 120	44.9 ± 2.2	1.62 ± 0.23	0.016 ± 0.001	21.9 ± 10.0
40	300 ± 120	38.4 ± 1.8	1.46 ± 0.08	0.013 ± 0.003	48.3 ± 20.3
45	320 ± 93	32.5 ± 1.6	1.46 ± 0.05	0.011 ± 0.002	58.0 ± 26.8
Microbatch Convection					
25	230 ± 100	57.7	1.56	0.021	10.5 ± 7.6
30	300 ± 160	77.1	1.61	0.027	22.4 ± 4.6
35	360 ± 150	35.2	1.41	0.013	80.0 ± 0.1
40	360 ± 150	40.1	1.53	0.013	93.4 ± 0.5
Microbatch Bath					
25	-	-	1.557	0.770	20.7 ± 5.5
30	410 ± 200	74.9	1.632	0.026	43.4 ± 25.7
35	360 ± 120	28.2	1.601	0.011	83.3 ± 10.7
40	350 ± 100	28.7	1.557	0.010	93.6 ± 5.2

[a] Measured diameters by SEM analysis with one standard deviation error

[b] Measured by N_2 physisorption

[c] Relative crystallinity from XRD

2.5 DISCUSSION

Over a century of experimental crystallographic and phenomenological models have been able to describe the intricate mechanisms for self-assembly, spontaneous nucleation, heterogeneous nucleation, epitaxial growth, phase rearrangements, and a multitude of specific pathways to go from molecular precursors to ordered solid crystals.[44,45] Underlying thermodynamic foundations of crystalline phases have been coupled with kinetic, transport and population balance modeling to describe and accurately predict the complex dynamics *a priori*.[15,46] Despite this immense foundational knowledge, the mechanism for zeolite crystallization remains a highly contested amongst experts in the field.[47–49] With regard to nucleation, it remains disputed whether homogeneous[18,50,51], primary[52]/secondary[53] heterogeneous nucleation or most recently aggregation of nanoparticles[8,54,55] dominates the kinetics. Furthermore, the growth mechanism also remains unclear with consideration of direct crystalline surface growth from solution[56], or by nonclassical nanoparticle-aggregate-mediated intermediates.[57] Population balance modeling has shown that reaction temperature plays a crucial role in determining induction time, which combined with our observed substantial temporal gradients suggests that nucleation may be heat transfer limited.[43] The experimental and theoretical work presented here contests that it is challenging to elucidate the mechanism when many methods for batch analysis are severely heat transfer limited.

Heat transfer limitations can emerge either while applying heat to the system, for example by slow external convection, or by internal spatial and temporal gradients within the crystallizer itself, typically resulting from large reactor volumes. Many studies have shown how mixing[25,26,49,50], ultrasonication[27,50,58] or microwave[50,55,59,60] heating can lead to higher levels of control over zeolite synthesis with faster, monodisperse crystals. While it is clear that these methods work to promote the synthesis, the quantification of the underlying transport is typically neglected. In many of these cases, the benefit is known to arise from faster, more consistent heating which leads to more steady driving forces for the process. Similarly, high frequency ultrasonication induces acoustic cavitation, which can again promote nucleation by providing localized energy spikes[27], but can also induce mixing which disrupts the delicate gel suspension.[26] The quantitative role of transport is not described and intrinsic kinetics are not achieved. Recent studies have suggested that in highly intensified flow systems, it may be possible to crystallize zeolites on the order of seconds, rather than the more typical hours or days.[39,61] To realize this, ultrafast heating must first be achieved to ensure a well-controlled isothermal environment.

From a theoretical perspective, convective heating in classical batch reactors (e.g. Teflon-lined 300 mL stainless steel autoclaves) is characterized by calculating the time constant for conduction (τ_{cond}) through a cylindrical medium, while external heating is characterized by natural or forced convective heat transfer (τ_{conv}). The ratio of the two time constants allows for assessment of the Biot number ($Bi = hL/k = \tau_{cond} \,/\, \tau_{conv}$) for a range of reactor sizes (L) and external heat transfer coefficients (h). The internal conduction should evaluate the serial resistances from the vessel components and internal gel; as the contributions to the overall resistance from the thin-walled polypropylene bottles is anticipated to be small relative to the internal fluid, the internal conduction is taken to be described by the thermal conductivity of water as a surrogate for the gel phase. Analogous to the Damköhler number for mass transfer, the ratio of crystallization rate to heat transfer rate were calculated as $\tau_{heat} \,/\, \tau_{cryst}$ where τ_{heat} was taken to be the slower of the two, τ_{conv} or τ_{cond}; $\tau_{cryst} = 650$ s is the characteristic intrinsic crystallization time, taken to be the asymptotic value for $t_{50} - t_0$ as the heating rate increased. The resulting analysis is visualized in Figure 2.9 for a family of heat transfer coefficients ranging from

$h = 10^{-2} - 10^{7}$ W m^{-2} K^{-1} (lines) and characteristic lengths of $L = 10^{-5} - 10^{0}$ m (symbols and shaded regions). Heating is considered fast if $\tau_{heat}/\tau_{cryst} < 0.1$. The crystallizer is considered isothermal if the internal heat conduction is fast relative to external convection ($Bi < 0.1$).

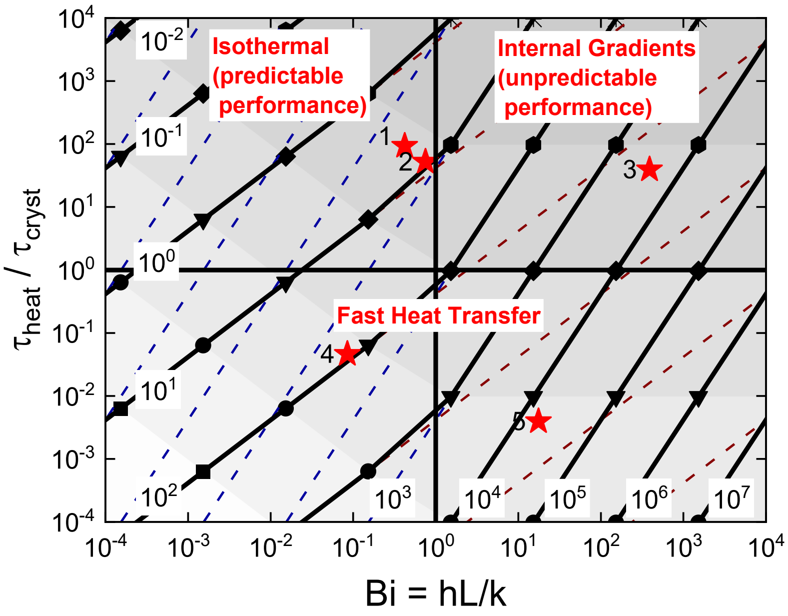

Figure 2.9: Kinetic regime map showing regions where batch reactors are anticipated to experience sufficiently fast heat transfer to be kinetically limited ($\tau_{heat}/\tau_{cryst} < 1$) and regions where slow internal heat conduction causes non-isothermal operation (Bi>1). Calculations performed with $\tau_{cryst} = 650\ s$ for a family of h values (inlaid labels) and reactor sizes L = 10^{-5} m (■), 10^{-4} m (●),10^{-3} m (▼),10^{-2} m (◆),10^{-1} m (⬢), 10^{0} m (✳). Experimental conditions are labeled with red stars (★) indexed to (1) batch oven, (2) batch convection oven, (3) batch bath, (4) microbatch convection oven, and (5) microbatch bath.

Experimental conditions for each crystallizer were evaluated using the data obtained in Table 2.2 and plotted on Figure 2.8 as red stars. The heat up time was taken to be the experimentally measured exponential time constant and heat transfer coefficients were calculated using conventional Nusselt number correlations as outlined in Appendix 1. The reactor configurations span the regime map between internal conduction, external convection, and reaction control. All batch reactors demonstrated insufficient heat transfer, with heating rates 10-100 times too slow relative to the crystallization time. Notably, conventional heating modes using ovens proved to exhibit heat transfer limitations by both external and internal heat transfer modes, while the heating bath was only internally limited. In contrast, the microbatch reactors achieved sufficiently fast heat transfer in both oven and water baths, with the optimal conditions achieving heat transfer rates 100-1000 times faster than the observed kinetic rates. This result suggests that microreactors, which typically have channel diameters of 0.1-1 mm, are sufficient to remove heat transfer limitations during zeolite crystallization and present a potential pathway toward achieving kinetically limited crystallization.

Table 2.2: Nondimensional analysis of convective heat transfer properties in crystallizers

Crystallizer	τ_{heat} [a] (s)	τ_{cond} [b] (s)	τ_{conv} [b] (s)	Bi	τ_0 [c] (s)	τ_{50} [c] (s)
Batch Oven	971	6.3×10^4	1.5×10^5	0.42	2700	3210
Batch Convection Oven	394	6.3×10^4	8.4×10^4	0.75	2100	2780
Batch Bath	154	6.3×10^4	1.6×10^2	389	1500	2680
Microbatch Convection Oven	21.1	6.3	7.4×10^1	0.085	1200	1950
Microbatch Bath	4.14	6.3	3.6×10^{-1}	17.6	1200	1810

[a] experimentally fit to transient heat up experiments.

[b] calculated based on empirical correlations for the internal conduction $\tau_{cond} = \rho c_P L^2 \,/\, k$ and external convection, $\tau_{conv} = \rho c_P L \,/\, h$. See Appendix 1.

[c] measured from XRD S-curve (t_0) and Avrami fits (t_{50})

From the kinetic analysis, it was observed that increasing the heating rate caused a corresponding decrease to the initial induction period, as observed in Figure 2.10. It should be noted that during slow heating, the induction period experienced a transient temperature profile, which when removed in the microbatch systems, gave rise to the intrinsic minimum induction period of $t_0 = 1200\ s$. Conversely, however, after the induction period is complete, the system has essentially stabilized at its steady temperature for all reactor configurations, causing the subsequent crystallization times ($\tau_{cryst} = t_{50} - t_0$) to be identical for all isothermal and fast configurations and representative of the intrinsic limit in the absence of heat transfer limitations, $t_{cryst} = 650\ s$. This is not unexpected, as the crystallization process is only weakly exothermic (~

-40 J/g-product[62]), which can be readily dissipated by the hydrothermal environment, especially over the tens of minutes of the crystallization step.

A significant outlier exists in the case of the batch water bath heated sample. In that scenario, the crystallization time is nearly double that of the other samples. Thermal gradients within the crystallization vessels are substantial at those conditions ($Bi = 389$), meaning that during the induction period, the outer shell likely reaches crystallization temperature substantially earlier than the center of the vessel. This non-uniformity means in the absence of mixing, each fluid parcel within the vessel experiences different temperature distributions, causing a convolution of slow and fast induction events. This in turn results in a bimodal distribution in particle size (Figure 2.8C) and a slower net rate of crystallization as observed in Figure 2.10 and quantified here as an outlier. It is interesting that in the slower batch heating modes, this distributed broadening of the crystallization time was not observed. The system acted as a transient isothermal crystallizer ($Bi < 1$), which was able to provide the same crystallization environment for all components in the reactor despite that environment changing with time. This criterion must be met to obtain a predictable crystallization performance.

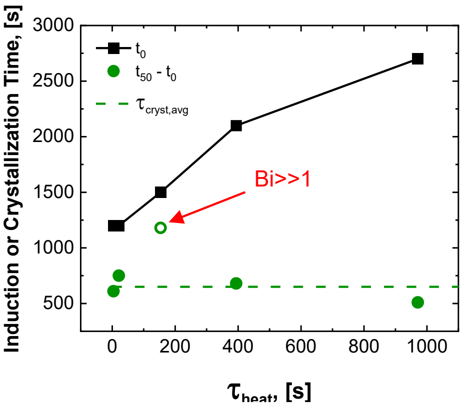

Figure 2.10: Induction time (t_0) and crystallization time ($t_{50} - t_0$) for each heating configuration demonstrating dominance of heat transfer limitations in batch reactors and conventional ovens. Outlier data point is labeled with an open circle.

2.6 CONCLUSION

A systematic reaction engineering evaluation of conventional batch and unconventional droplet-based microbatch crystallizations was performed for the hydrothermal sol-gel synthesis of LTA. The analysis revealed substantial external and internal heat transfer limitations, particularly during the initial induction period. Limits to the induction and crystallization times in the absence of heat transfer limitations were observed at 1200 and 650 seconds, respectively. In scenarios where internal heat transfer cannot occur sufficiently fast, caution is advised against using ultrafast external heating modes as internal gradients can induce poor uniformity of the crystallization environment, yielding unpredictable results. For this reason, it is suggested that when $\tau_{heat}/\tau_{cryst} < 1$ cannot be met, slower heating be used such that $Bi < 1$. The criteria are summarized as:

- To ensure heating is sufficiently fast: $\tau_{heat} / \tau_{cryst} < 1$
- To ensure uniformity within the reactor: $Bi < 1$

It was demonstrated that using a microdroplet generator, 1.7 μL microbatches could be generated that operate in the absence of internal and external heat transfer limitations. It is noted, however, that the rate-controlling phenomena was not explored further to delineate if this is a kinetic limit or if other limiting phenomena such as mass transfer amongst the three-phase sol-gel systems are present. While decreasing the characteristic length in the micro-system does typically also enhance diffusion ($\tau_D = L^2 / D$), the non-classical crystallization method is likely characterized by dimensions within the gel or boundary layers near the surface of the crystals. Further characterization of the mass transfer and intrinsic kinetics are required to truly leverage the potential for ultrafast zeolite synthesis.

Acknowledgements: The authors acknowledge the American Chemical Society Petroleum Research Fund for financial support, ACS PRF 58609-DNI5.

CHAPTER 3

IN SITU SEEDING AND CRYSTALLITE RIPENING VIA ULTRAFAST THERMAL OSCILLATIONS IN SEGMENTED FLOW MICRO-REACTOR

3.1 INTRODUCTION

Logistical barriers involving solids processing have hindered the commercial viability of continuous crystallization as concerns over clogging, access to in situ characterization[63], and control over the crystallizer environment limited the scalability of novel technologies.[64] Instead, traditional batch processes persist as the predominant method for crystal production despite being plagued by issues of polymorphic impurity and polydispersity, which can be traced back to the stirred tank reactor design. The excessively large thermal mass results in long heat up times and requires vigorous agitation to minimize gradients within the reactor body. Slow transport kinetics result in the inability to freely move around the phase diagram thereby locking the process out of operating windows capable of generating significant yields of kinetically favored polymorphs.[65] Furthermore, agitation within the crystallizer provides both a heterogeneous surface to facilitate primary nucleation and the kinetic energy required to promote secondary nucleation.[66] Continuous flow tubular crystallizers offer a plethora of tunable parameters that solve each of these problems to deliver a reactor design that is controllable and scalable.[67,68]

This work details the construction and implementation of a series of segmented flow microfluidic devices that were designed to rapidly traverse the phase diagram. Each self-contained microdroplet serves as a mobile batch reactor whose temperature can be rapidly and isothermally changed by virtue of fast heat and mass transfer at the minimized length scale.[69] It is demonstrated that establishing stable hydrodynamics prior to cooling is key for fully continuous operation.[70] Favorable interactions between inert carrier phase and the tube wall create a sheath around each microdroplet preventing deposition and undesired secondary nucleation that leads to bridging and clogging.[71] Photolithography was used for rapid prototyping of lab on chip devices to tune the size, forced internal convection, and residence time of microdroplets.[72,73] These microfluidic channels were then scaled up to a modular milli-fluidic press-fit design to incorporate ultrasonication for in situ seeding[74] to study the tunability and effects of high frequency temperature oscillations.[75] In line microscopy and UV-vis spectroscopy were implemented in tandem for further intensification to capture the changes in the crystallization mixture as they occurred in real time.[76] These design choices culminate in the successful ripening of paracetamol seed crystals that were generated in situ using indirect ultrasonication.

3.2 METHODS

3.2.1 FLOW REACTOR DESIGN

A continuous flow tubular crystallizer was composed of a CSTR, microdroplet generator, sonication bath, and temperature oscillation zone. The mother liquor was first prepared by fully dissolving 1.6 g of paracetamol (Thermo Scientific, 98%, CAS 103-90-2, received as used as is) in 40 mL of DI water inside a sealed 60 mL luer lock syringe to generate a 4 $wt\%$ stock solution. This mixture was then placed in a hot water bath and mixed with an internal magnetic stir bar until fully dissolved whereafter it was transferred to a Harvard syringe pump and wrapped with heating tape. Once the temperature stabilized at 70 $°C$, well above the solubility condition, the syringe was connected to the process line composed of PFA tubing. The tubing was then press-fit into the microdroplet generator shown in Figure 3.1A, which consisted of a series of perpendicular channels etched into a block of aluminum held isothermal by a cartridge heater and PID controller. Once inside, aqueous phase paracetamol (dispersed phase) was injected into the system at a flow rate of $0.05\ mL/min$ using a Harvard Apparatus syringe pump, where the solution perpendicularly intersected a stream of inert oil (mobile phase) at a T-junction. At this point the force of the continuous oil phase sheared the aqueous phase into a steady stream of $2\ \mu L$ microdroplets with an aspect ratio of nearly 1:1.

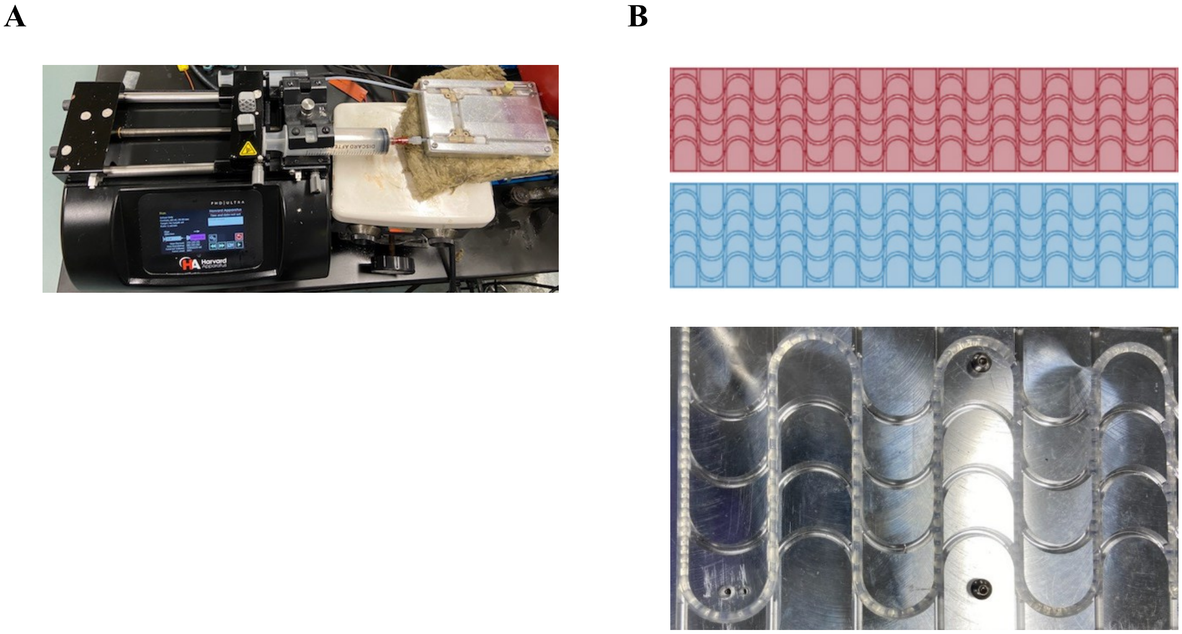

Figure 3.1: Photo of CSTR syringe pump connected to temperature-controlled microdroplet generator; schematic of continuous tubular crystallization designed for thermal oscillations with in-lab photo of experimental segmented flow droplets (B).

Upon exiting the droplet generator, the process line was immediately immersed in a water bath held at $10\ °C$ where the droplets were indirectly exposed to ultrasonic vibrations for approximately two minutes as shown in Figure 3.2. This residence time was sufficiently long for the sonication horn to induce nucleation of fine crystallites without also causing a coalescence of adjacent droplets. From here, the process line was press fit into a series of channels that were etched into two blocks of aluminum, each set to an individual isothermal temperature depicted in

Figure 3.1B. Throughout this section each microdroplet experienced the same thermal pathway and mixing profile until being quenched at the outlet where the solid products were washed with ice cold water and vacuum filtered.

Figure 3.2: In situ seeding via indirect ultrasonication.

3.2.2 IN SITU MICROSCOPY

Microdroplets in flow were observed and recorded with a TOMLOV USB microscope. When positioned above tubing locations corresponding to residence times greater than the induction time of paracetamol nucleation, crystallites of various sizes and shapes were detected. Crystal number, quality, and reproducibility could be tracked over a series of microscope positions and correlated to residence times for fitting nucleation kinetic models. Moreover, visually tracking the consistency of droplet size, crystal size, and number density could serve as an indicator for process upsets, such as particle deposition, secondary nucleation, and reactor hot spots.

3.2.3 UV-VIS SPECTROSCOPY FLOW CELL

The UV-Vis flow cell was the creative result of applying process intensification principles to Beer's law, which correlates the intensity of light transmitted through a solution to the concentration of particles within the solution. Mathematically, this relationship is represented by Equation (1) and **Figure 3.3**A, where A is absorbance, I_0 is the intensity of the reference sample,

I is the intensity of the measured sample, ϵ is the molar extinction coefficient of the solute in solution, l is the path length, and C is the concentration in solution:

$$(1)\ A = \log\frac{I_0}{I} = \epsilon \cdot l \cdot C$$

Continuous operation allows for high throughput data collection (20 scans per second) as concentration measurements can be taken for every droplet that flows through the cell. This simple tubular design depicted in **Figure 3.3**B is compatible with nearly every key position found on the crystallizer flow path. Reducing the path length by an order of magnitude in turn expands the threshold of detectable concentrations by an order of magnitude.

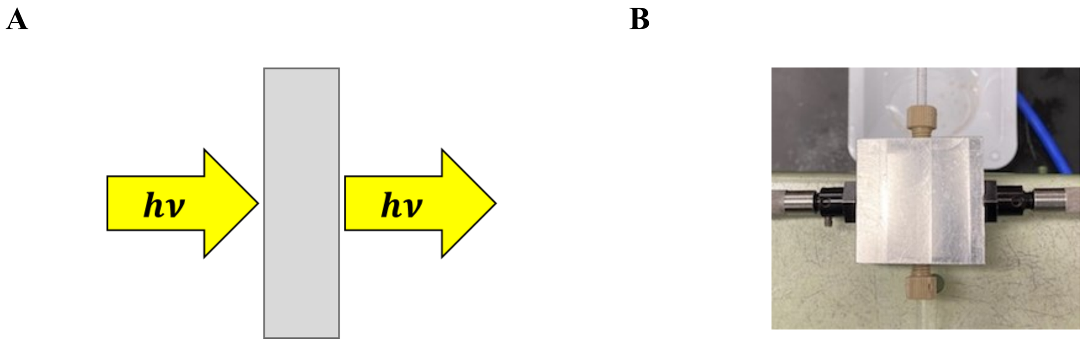

Figure 3.3: Illustration of Beer-Lambert Law where each yellow arrow represents a photon of a given frequency entering the path length denoted as a standard cuvette (A) and in line UV-Vis flow cell composed of an aluminum block stabilizing two colinear fiberoptic leads and a quartz tube fed through the path length.

3.3 RESULTS AND DISCUSSION

3.3.1 CAPTURING SECONDARY NUCLEATION IN FLOW

The USB microscope successfully captured still photos of microdroplets mid-crystallization demonstrating the ability to resolve entire droplets and quantify their contents. Studying the crystals displayed in Figure 3.4 reveals the high level of uniformity in crystal nucleation and growth that can be achieved under stable hydrodynamic flow conditions.

Interestingly, it appears that crystals consistently nucleate at the lagging droplet-oil interface and grow inward toward the center of the droplet suggesting the difference in surface tension between the two fluids is high enough to act as a surface for heterogeneous nucleation.

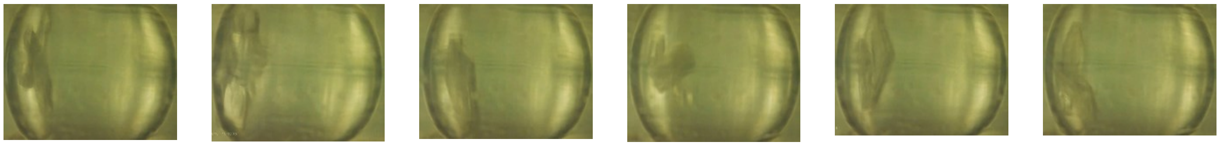

Figure 3.4: Collection of micrographs showcasing slow, controlled secondary nucleation in flow.

Despite dropwise reproducibility within a single synthesis, persistent challenges between runs stemming from cleaning procedures and transience on startup make uncontrolled secondary nucleation a major barrier to the efficacy of this technology. Fresh solution colliding with rogue crystals leftover from previous runs can cascade into hydrodynamic failure as exemplified in Figure 3.5. In contrast with the previous set of photos, this collection shows not only higher number density and variance in particle size but also the complete disappearance of segmented flow. Instead, this is most likely the annular flow where the oil phase coats the tube walls entirely surrounding the aqueous stream and forcing it into a centerline channel. Without the oil boundary separating the droplets, crystals are able to move freely throughout the continuum of the aqueous phase resulting in more collisions and faster nucleation. This autocatalytic effect runs the risk of causing catastrophic clogging ruining the reproducibility that is the hallmark of continuous operation. Furthermore, chaotic hydrodynamics introduce radial variability within the reactor body defeating the purpose of operating on such a small length scale.

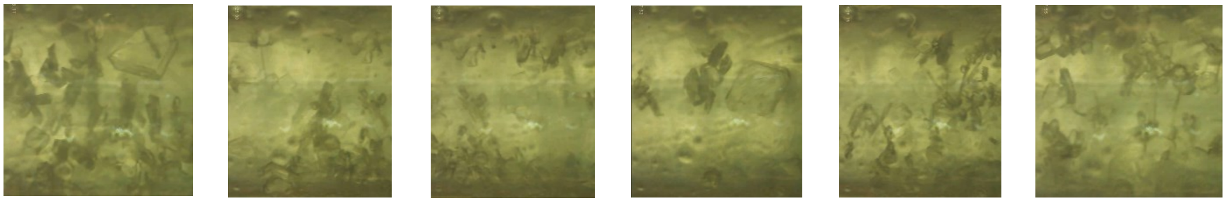

Figure 3.5: Collection of micrographs highlighting chaotic nature of uncontrolled secondary nucleation.

3.3.2 RESOLVING PARACETAMOL CONCENTRATION ON A DROPWISE BASIS

Segmented flow crystallization separates the mother liquor into a series of self-contained microbatches that follows the designated path of the crystallizer. Phase boundaries separating each of the droplets and the surrounding oil phase act as barriers to prevent crystal overgrowth, droplet coalescence, and solids expulsion. Confining the crystallization mixture to a volume of a single microliter significantly reduces the characteristic time for diffusion increasing the rate of mass transfer and physically restricting the maximum size to which crystals are able to grow.

Furthermore, as seen in the optical microscopy results of the previous subsection, crystals tend to nucleate along the edge of this interface and grow inward toward the center of the droplet. Altogether, micro-scale mixing should kinetically outpace the slow crystal growth thereby minimizing gradients in the radial direction, and small aspect ratios should eliminate gradients in the axial direction. Establishing liquid phase uniformity throughout the droplet provides the precision needed for an in-line spectroscopy probe to measure the concentration as droplets pass through the path length. Performing this analysis in flow facilitates rapid high throughput data collection within the small hardware footprint of a microfluidic device.

Figure 3.6A shows spectra of aqueous paracetamol at a series of concentrations to highlight the nonlinear nature of the absorbance signals. Notably, subsections of the spectra can be transformed to exhibit linearity at different concentration ranges making them candidates for applying Beer's law. Those corresponding to crystallization, i.e. $C = 1.5\,kg/kg$ to $C =$

$4.0\ kg/kg$, show linearity when averaging signals from $\lambda = 310\ nm$ to $\lambda = 315\ nm$. Figure 3.6B shows a collection of time-resolved intensity readings for a series of concentrations specifically chosen to be in the subsaturation zone to prevent scattering by any solids in suspension.

The consistency of intensity across the plateaus verifies the ability to resolve dropwise concentration; this confidence is bolstered by the similarity between calibration curves shown in Figure 3.6C, which shows great agreement between single phase and segmented flow measurements for a set of concentrations. The accuracy of the data fit allows for extrapolation in dropwise measurements, meaning the in situ UV-Vis flow cell has the potential to capture real time changes in solution occurring in each droplet as crystals are nucleated and grown for time on stream spans on the order of hours.

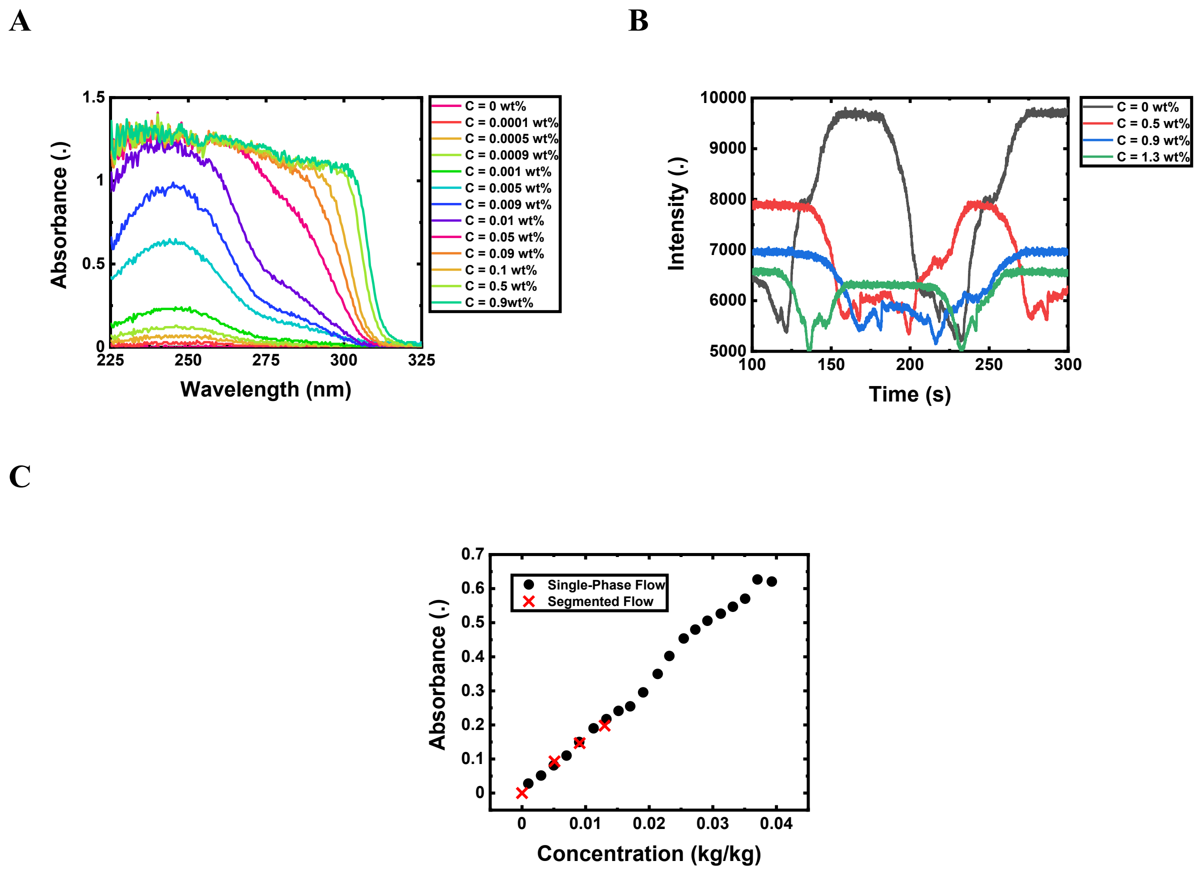

Figure 3.6: UV-Vis spectra (A), dropwise intensity readings (B), and calibration curve for single phase and segmented flow (C).

3.3.3 SONOCRYSTALLIZATION AND RIPENING IN FLOW

Microdroplets containing supersaturated paracetamol solution were indirectly exposed to ultrasonication whose vibrations successfully induced nucleation without causing the coalescence of adjacent droplets. These droplets then underwent a series of unique thermal oscillations by varying the duty cycle and amplitude of the waveform. Micrographs displayed in Figure 3.7A and Figure 3.8A revealed the occurrence of classical ripening taking place during dynamic crystallization, where small particles were dissolved in the high temperature zone, and their mass was subsequently taken up by the remaining crystals upon entering the low temperature zone. This cycling back and forth across the solubility boundary was designed to reduce number density and make the population more monodisperse.

While ripening did occur, it appears the extreme amount of nucleation induced by the ultrasonics may have introduced mass transfer limitations within the newly formed seeds. This was evident in the broadening of the particle size distributions following thermal oscillations shown in Figure 3.7B and Figure 3.8B. Under these operating conditions, a concentration gradient formed within the cluster of seeds limiting which crystals were capable of ripening. Those at the surface of the seed cluster had direct access to the nutrient-rich solution and grew faster, while those deeper in the cluster grew slower as they relied on the solution to slowly permeate through the densely packed solids.

Particle size distributions showed that as amplitude was increased, the distribution of crystals broadened with a net increase in the average particle size. Similarly, as duty decreased, the system also grew in average particle size. Each of these results can be traced back to the mechanistic effects induced by each of the dynamic parameters. When the cold temperature is held constant, increasing the amplitude means increasing the temperature in the hot zone, which increases the thermodynamic driving force for dissolution and speeds up the process. By spending a sufficiently long time spent in the cold zone, there was net growth of crystals as the solution approached equilibrium again. Shifting the duty cycle lower meant introducing a kinetic bias toward growth such that the mixture spent more time in the cold zone resulting in greater amounts of conversion. If dynamic ripening is to be made broadly effective, higher mixing rates must be achieved while also minimizing the amount of agitation in the system to prevent secondary nucleation from dominating over growth.

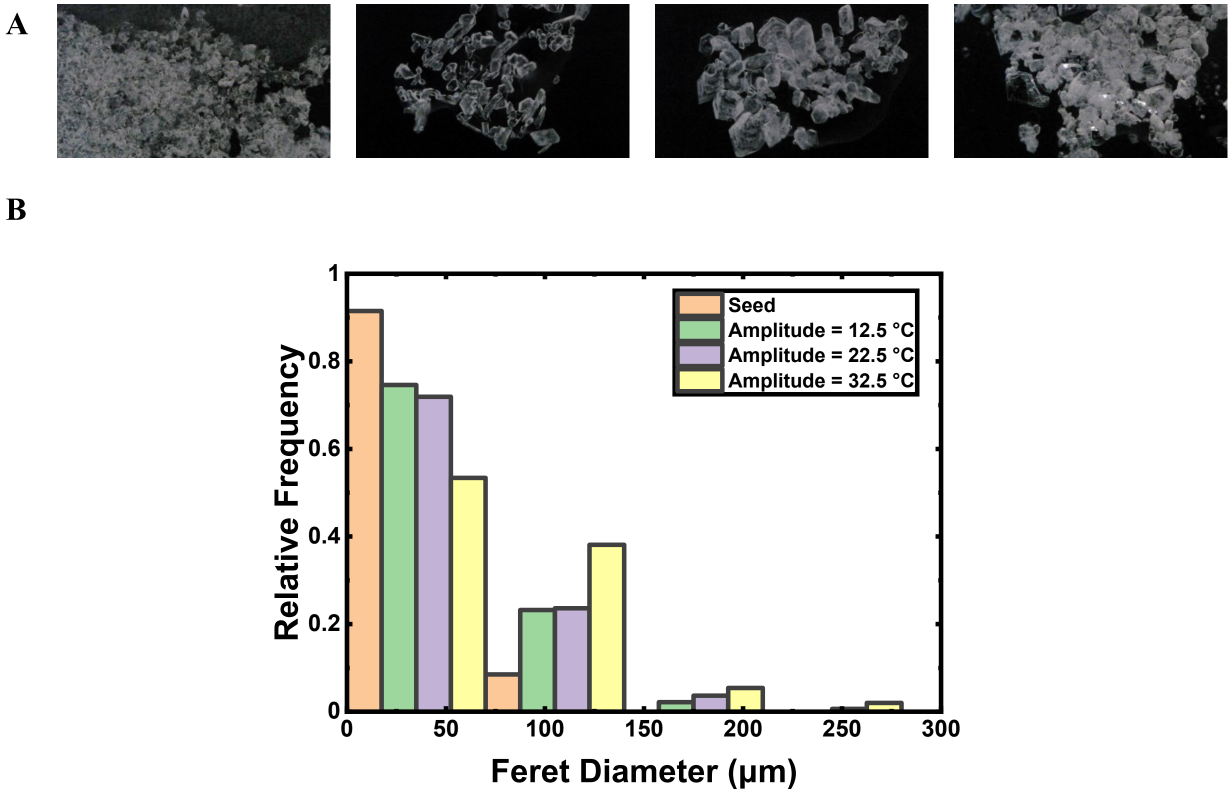

Figure 3.7: Micrographs of seed transformations (A) and particle size distributions for dynamic ripening of seed crystals at a series of amplitude settings (B).

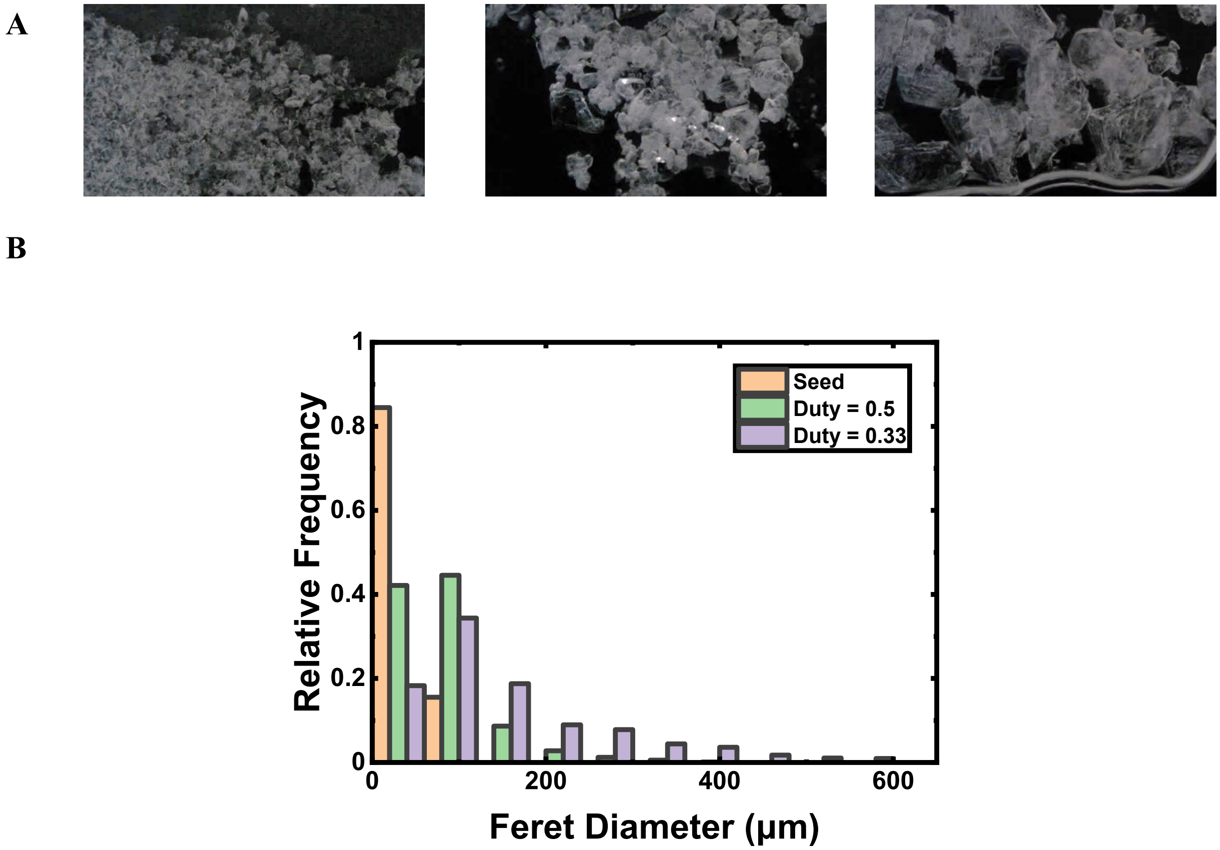

Figure 3.8: Micrographs of seed transformations (A) and particle size distributions for dynamic ripening of seed crystals at a series of duty cycle settings (B).

3.4 CONCLUSION

This work details the construction and implementation of a micro-scale flow crystallizer equipped with multiple temperature-controlled zones, in line optical microscopy, and in situ UV-Vis spectroscopy. The modular design of the crystallizer flow path allowed for temperature oscillations as large as $65\ ^\circ C$ in addition to the capability to change the flow path and residence time within each isothermal zone. Dynamic thermal oscillations combined with in situ nucleation induced by ultrasonic vibrations created a system where forced crystal ripening could be performed. Changes occurring within a single droplet between the solid and liquid phase can be tracked down to a fraction of a second by pairing microscopy with spectroscopy. Currently, challenges surrounding mass transfer limit the scalability of this design because of the difficulty of achieving high degrees of mixing at the microliter scale. Insufficient mixing lacks the energy for molecules to collide and organize into the crystal lattice preventing nucleation in the first place. Conversely, excessive mixing by ultrasonication causes uncontrolled nucleation where crystallites become densely and incapable of receiving nutrients from the surrounding solution.

CHAPTER 4

CONTROLLING THE RIPENING FATE OF SEED CRYSTALS THROUGH DYNAMIC TEMPERATURE OSCILLATIONS

4.1 ABSTRACT

Inverse ripening is the process by which a population of small crystallites is nucleated and grown at the expense of larger seed crystals. This upward thermodynamic climb is achieved through rapid oscillations in temperature to drive competitive amounts of dissolution (N_X) and nucleation (N_B). Applying a series of square waveforms to the temperature profile has direct effects on the ratio $\left(\frac{N_B}{N_X}\right)$, whose value proves to be a reliable indicator for the occurrence of inverse ripening. By utilizing population balance modeling to simulate dynamic crystallization, a systematic scan of duty ($10\ \% - 90\ \%$), frequency ($0.005\ Hz - 0.02\ Hz$), and amplitude ($10\ °C - 20\ °C$) yielded values for $\left(\frac{N_B}{N_X}\right)$ ranging from over 372,000 down to less than 0.05. These results served as frame for a regime map based predictive model for determining the occurrence and growth rates of inverse ripening populations.

4.2 INTRODUCTION

Traditional ripening is a dynamic process that aims to directly control the particle size distribution of a crystal population by eliminating small particles to drive the growth of larger particles.[77] This is achieved through temperature cycling where the system shifts between environments that favor dissolution/disappearance and growth/nucleation according to classical crystallization theory.[78,79] Thermodynamics and kinetics together dictate which of the two processes is dominant within their respective environments.[80] However, there have been a handful of studies predicting and fewer demonstrating the occurrence of inverse ripening, where a collection of large particles are sacrificed in favor of more small particles. This reversal is most often observed in metallurgy by exposing particles to ion irradiation thereby inducing atomic mixing, which disrupts the normally immiscible separated components.[81] In contrast, this work provides broad, substantial evidence that explains how oscillatory temperature profiles capitalize on the inherent transience of crystallization processes to offer enhanced control over the chemical environment. Applying a variety of waveforms unlocks the tunability of the phenomena that control the average particle size, number density, and polydispersity of a crystal population.

Thermodynamic interactions between particles determine the solubility curve, and thus by periodically changing temperature, the system can move back and forth across the equilibrium boundary.[82] With each temperature change, the equilibrium concentration changes as well thereby repeatedly regenerating the thermodynamic driving force known as super- and subsaturation.[83] When a system is held at a constant temperature, the driving force is depleted over time according to the kinetics of the system. Under high temperature conditions, subsaturation causes all particles to shrink with the smallest particles potentially disappearing completely, which increases the concentration in solution and lowers the number density of the population.[84] This increase generates new supersaturation when the temperature shifts lower allowing the remaining large particles to grow. As supersaturation is consumed, nucleation of new particles and growth of existing particles are occurring simultaneously.[85] Typically, ripening is most effective when supersaturation maintained at relatively low levels as this kinetically limits the rate of nucleation in favor of only growth.[86,87] Closely monitoring the transient behavior of the solid and liquid phases has allowed researchers to measure nucleation, growth, and dissolution rates and construct models detailing their temperature and concentration dependence. Kinetic models can then be fed into simulation software that continually solves the mass balance within the multiphase mixture through a technique known as population balance modeling.[88] Understanding these relationships has proven effective in designing dynamic temperature profiles for a variety of crystallization applications.

Since the turn of the century, temperature cycling has been applied to numerous chemistries with the goal of controlling particle size, polydispersity, and morphology. A priori control over these factors is highly sought after because of their impact on the bioavailability of active pharmaceutical ingredients, flowability of solids in chemical manufacturing, and the overall chemical behavior of crystalline materials. Researchers at Bristol-Myers Squibb reported on the effects of consecutive rounds of ultrasonication and temperature cycling on their proprietary drug molecule. Their work demonstrated that crystals could be transformed from a fibrous needle-like habit to a denser brick- and rod-like morphology in addition to becoming more monodisperse via the elimination of small granules.[89] Further control over crystal shape was revealed by the Doherty Research Group out of University of California Santa Barbara. Results showed that the time on stream and phases of the temperature cycle can be tuned to introduce a kinetic bias in the growth and dissolution regimes allowing for varying degrees of crystal smoothening and elongation.[90] Mechanism manipulation was taken a step further by Li et al. as they elucidated the temperature sensitivity of nucleation and growth steps in polymer recrystallization and the many possible growth pathways that arise in different kinetic regimes.[91] In the last decade Professors Nagy and Rielly have made significant advancements in thermal cycling by introducing control schemes to regulate the crystallization trajectory. In situ particle sizing and spectroscopy were used to detect polymorphism and deliver the real time information required to close the feedback loop. Maintaining a low level of supersaturation through precise temperature control facilitated the removal of fines, control over particle size, and improvement in morphological purity.[92,93] Each of these components have been combined in the work by Besenhard et al. where polymorphs of varying stability were successfully nucleated and ripened through the use of a microfluidic segmented flow crystallization setup.[94] While each incremental step forward in temperature cycling technology has opened up new layers of control, oscillations have thus far taken place on the order of hours effectively constraining the ripening process to the thermodynamic limits of their respective systems.

Wave frequency, duty, and amplitude together determine whether the dynamic system is thermodynamically or kinetically limited. If the waveform has an adequately long period and is allowed to reach equilibrium, then the system has reached its thermodynamic limit, and no further changes will occur. Otherwise, if temperature changes before equilibration, the system is kinetically limited. Frequency sets the number of cycles that occur within a given timespan, which defines a hard limitation on whether the system has enough time to reach equilibrium. Duty further establishes the kinetic capabilities of the system by denoting the fraction of a cycle that is spent in the high temperature region verses the low temperature region. Lastly, amplitude drives the kinetics themselves as shifts in temperature and solubility directly influence the supersaturation required to move the system toward equilibrium.

First, we hypothesize that the bias toward nucleation and growth associated with a low duty cycle is the key to preventing the elimination of small particles. Furthermore, implementing low duty cycles should cause the long-term behavior of the distribution to resemble the equilibrium conditions at the low temperature than those at the high temperature resulting in a stable high yield particle size. Second, we hypothesize that high frequency oscillations drive competitive amounts of growth and dissolution between each hot and cold cycle. This kinetically limited temperature cycling should promote the formation prevent of fine crystallites while simultaneously preventing their complete elimination alongside the disappearance of the initial seed subpopulation. Third, we hypothesize that lower amplitudes will restrict the overall operating window resulting in narrower ranges in supersaturation, which will in turn limit the kinetic rates of crystallization processes. Prohibiting the full dissolution of the solid phase by adjusting the thermodynamics of the system should ensure stable nucleation rates required for inverse ripening. Our final hypothesis is an amalgamation of the prior three: operating dynamically under high amplitude, high frequency, and low duty waveforms drives the formation new crystal nuclei at the expense of large seed crystals thereby achieving inverse ripening through kinetic locking. Kinetically limited dissolution prevents full elimination of new nuclei, while kinetically limited nucleation and growth consumes the liberated solute but not so much that the new population broadens out of control.

This work demonstrates how operating in kinetically limited heating and cooling regimes unlocks a myriad of possibilities for controlling the fate of solute particles. Assigning a square wave to the temperature profile provides sufficiently high precision when changing between environments; step changes are preferred over temperature ramping as this avoids introducing further undesired transience into the transformation kinetics.[95] Each successive temperature cycle generates a new set of operating conditions as particle shrinkage and disappearance within the hot interval is offset by the competitive depletion of supersaturation by growth and nucleation in the cold interval. The periodic release and uptake of solute results in a particle size distribution that is constantly changing, which in turn generates unique concentration profiles and kinetics that have a cascade effect on each cycle that follows. Quantifying the impacts of the waveform parameters and building a predictive model around them are crucial steps for understanding how to exercise kinetic control over the crystallization trajectory. Dynamic crystallization represents a bottom-up approach to achieving inverse ripening by creating a new population of fine crystals through the reformation of stable seeds.

4.3 METHODS

4.3.1 POPULATION BALANCE MODELING

Population balance modeling describes how the number distribution changes over time with nucleation, growth, dissolution, and disappearance.[96] A simplified population balance equation, i.e. one-dimensional size-independent growth ($G \neq G(n) = dL/dt$), with accompanying initial and boundary conditions is shown in Equations (1) – (3):

$$(1)\ \frac{\partial n}{\partial t} + G\frac{\partial n}{\partial L} = 0$$

$$(2)\ n(t = 0, L) = n_0$$

$$(3)\ n(t, L = 0) = \begin{cases} \frac{B}{G}\ for\ S \geq 1 \\ 0\ for\ S < 1 \end{cases}$$

This partial differential equation characterizes the phase behavior of constant density, single morphology crystals within an ideal stirred tank crystallizer such that the internal environment is uniform. Agglomeration and breakage have been neglected in favor of lumped growth and nucleation models. Qualitatively, Equation 1 states that the time-resolved number density of a given particle size increases or decreases because of growth into or dissolution out of the specific subset of the overall population, respectively. The initial condition described in Equation 2 simply defines the seed particle size distribution; the hypothetical seeds used in this study were initially equilibrated with the surrounding solution at $20\ °C$ with the particle size distribution reflecting a mass of crystals that will fully dissolve at $60\ °C$ shown in Figure 4.1.

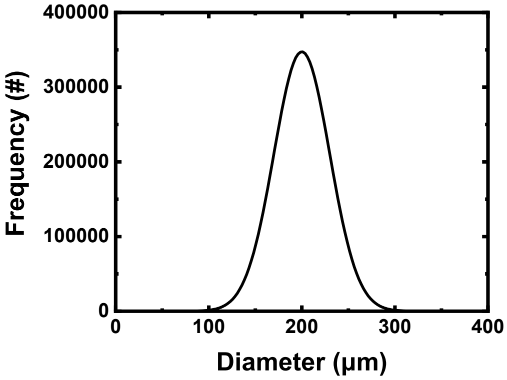

Figure 4.1: Number distribution for seed crystals follows a Gaussian fit with average particle size of $200\ \mu m$ and full width half max value of $70.65\ \mu m$.

The boundary condition listed in Equation (3) denotes the point at which shrinking particles vanish and new particles are born. This distinction lies in the value of the supersaturation defined in Equation (4) where C designates the concentration in solution and C_{Eq} specifies the concentration at equilibrium. Equilibrium concentration, also termed solubility, is a strong function of temperature, T, and is described quantitatively by the exponential function[88] shown in Equation (5) and **Figure 4.2**:

$$(4)\ S = \frac{C}{C_{Eq}} \,[=]\, Dimensionless \qquad (5)\ C_{Eq} = 0.129 \exp[0.0194 \cdot T(°C)] \,[=]\, kg/kg$$

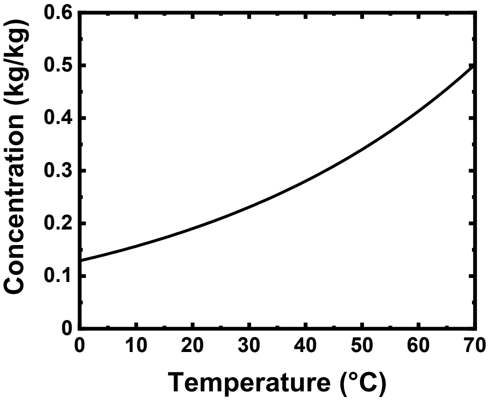

Figure 4.2: Solubility function for paracetamol in ethanol with supersaturation and subsaturation zones above and below the curve, respectively.[97]

The method of moments is a transformation-based numerical method that solves Equation (1) for each particle size in the distribution at a series of time steps based on changes in the solid and liquid phases. The graphical user interface for solving the population balance equation and corresponding user-defined inputs is described at length in Appendix 2. Applying the definition of a moment (μ_j) in Equation (6a – d), mathematical expressions are connected to a set of physical dimensions revealing several relationships that can be used to measure the state of the solid phase. Applying the time derivative to μ_0 and μ_3 listed in Equation (7a – b) creates a system of ordinary differential equations whose solutions describe the time-resolves trajectory of the crystallization:

$$(6)\ \mu_j = \int_0^\infty L^j n(L)dL\,, for\ j = 0,1,2,\ldots$$

$$(a)\ \mu_0 \propto Number\ Density$$

$$(b)\ \mu_1 \propto Diameter$$

$$(c)\ \mu_2 \propto Surface\ Area$$

$$(d)\ \mu_3 \propto Volume$$

$$(7)\frac{d\mu_j}{dt} = jG\mu_{j-1}$$

$$(a)\ \frac{d\mu_0}{dt} = B$$

$$(b)\frac{d\mu_3}{dt} = -\frac{1}{k_v\rho}\frac{dC}{dt} = G\mu_2$$

Nucleation (B) and growth (G) rates are heavily dependent on supersaturation and inter- and intramolecular interactions between solute and solvent particles. Kim et al.[98] have recently published a study focusing on extracting kinetic parameters for primary and secondary nucleation and growth and dissolution using temperature cycling to construct the kinetic models listed in Equations (8) – (11), respectively. Parameters for each equation are listed in **Table 4.1** and **Table 4.2**.

$$(8)\ B_1 = k_{b1}\exp\left[-\frac{16\pi v^2\sigma^3}{3k^3T^3(\ln S)^2}\right][=]\ \#/kg\ solvent \cdot s$$

$$(9)\ B_2 = k_{b2}(S-1)^\alpha m_s^\beta\ [=]\ \#/kg\ solvent \cdot s$$

$$(10)\ B = B_1 + B_2\ [=]\ \#/kg\ solvent \cdot s$$

$$(11)\ G = \begin{cases} \frac{k_g}{C_{Eq}^{\gamma_g}} \exp\left(\frac{-E_{A_g}}{RT}\right)(S-1)^{\gamma_g}\ for\ S \geq 1 \\ \frac{k_d}{C_{Eq}^{\gamma_d}} \exp\left(\frac{-E_{A_d}}{RT}\right)(1-S)^{\gamma_d}\ for\ S < 1 \end{cases} \quad [=]\ \mu m/s$$

Table 4.1: Kinetic parameters for primary and secondary nucleation referenced from Kim et al.[98]

Parameter	Symbol	Value	Units
Rate Constant	k_{b1}	10.6	$(\#/min \cdot kg\ solvent)$
Molecular Volume	v	2×10^{-28}	(m^3)
Interfacial Energy	σ	3.83×10^{-3}	(J/m^2)
Boltzmann Constant	k	1.38×10^{-23}	(J/K)
Rate Constant	k_{b2}	1.39×10^{6}	$(\#/min \cdot kg\ solvent)$
Experimental Model Fit	α	2.39	$(-)$
Experimental Model Fit	β	0.41	$(-)$

Table 4.2: Kinetic parameters for growth and dissolution referenced from Kim et al.[98]

Parameter	Symbol	Value	Units
Rate Constant	k_g	2.26×10^{8}	$(\mu m/min)(kg/kg)^{-\gamma}$
Activation Energy	E_{A_g}	3.62×10^{4}	(J/mol)
Supersaturation Parameter	γ_g	1.14	$(-)$
Rate Constant	k_d	-4.08×10^{4}	$(\mu m/min)(kg/kg)^{-\gamma}$
Activation Energy	E_{A_d}	9.80×10^{3}	(J/mol)
Supersaturation Parameter	γ_d	0.93	$(-)$

Solid crystal mass, m_S, is continually updated using Equation (12) by performing a mass balance on the initial seed distribution at equilibrium and comparing it to the concentration in solution at the given time:

$$(12)\ m_S(t,T) = m_{Seed} + m_{Solvent} \cdot C_{Eq,20°C} - m_{Solvent} \cdot C_{Eq}(T) \cdot S(t,T)$$

A sensitivity analysis was performed on a series of square wave temperature profiles that were input into the population balance model described in the previous section. Oscillating between isothermal temperature zones ensured consistency in each of the equilibrium conditions. This allowed for supersaturation profiles to be constructed for each temperature zone throughout the simulation, which were subsequently fed into kinetic models described by Equations (8) – (11) to visualize any transient dynamic effects and to understand the competitive nature of the processes. Particle size distributions were measured at the ends of each temperature zone to track the behavior of particle subpopulations. This set of parameter sweeps was designed to systematically isolate the conditions that promote either traditional or inverse ripening. The waveform parameters described in Equations (13) – (15) have direct impacts on the kinetics and thermodynamics of dynamic crystallization.

$$(13)\ D = \frac{t_H}{t_H + t_C} \cdot (100\%)\ [=]\ \%$$

$$(14)\ f = \frac{1}{t_H + t_C}\ [=]\ Hz$$

$$(15)\ A = \frac{T_H - T_C}{2}\ [=]\ ^{\circ}C$$

4.3.2 HYPOTHESIS 1: TEMPERATURE PROFILES FOR DUTY

Duty (D) specifies what percentage of the cycle is spent in the hot temperature region. Amplitude and frequency were set to constant values of $A = 20\ ^{\circ}C$ and $f = 0.01\ Hz$, respectively, and duty was allowed to vary to quantify the effects of altering the relative amounts of growth/nucleation and dissolution/death. Temperature profiles for the duty parameter sweep are illustrated as a waterfall plot in Figure 4.3.

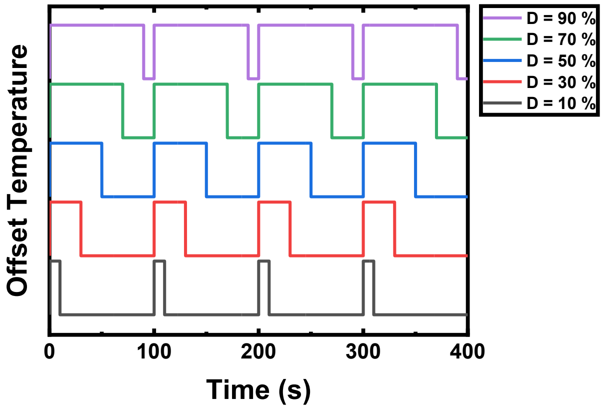

Figure 4.3: Varying duty cycle redistributes time within a given period which introduces a bias such that the dynamic system favors growth over dissolution, or vice versa, according to the kinetics. High duty cycles favor the hot temperature, while low duty cycles favor the cold temperature.

4.3.3 HYPOTHESIS 2: TEMPERATURE PROFILES FOR FREQUENCY

Wave frequency (f) controls how often the system undergoes a full thermal cycle and thus determines whether a dynamic system can ever reach equilibrium. Duty and amplitude were held constant at $D = 30\ \%$ and $A = 20\ °C$, respectively, to measure the effects of varying frequency on the crystallization trajectory. Temperature profiles were fitted to three different wave frequencies as shown in **Figure 4.4**.

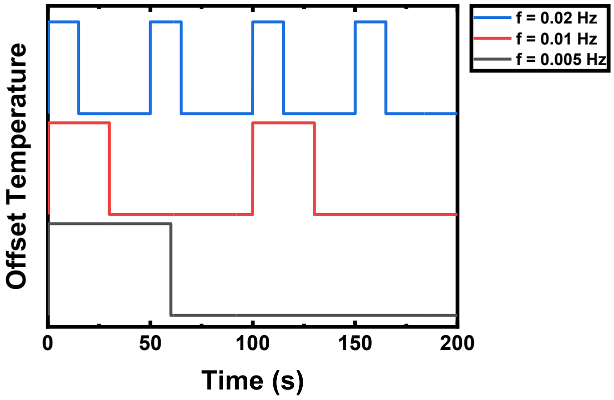

Figure 4.4: Frequency controls the time duration of a single cycle. By varying frequency, a system that was initially thermodynamically limited can become kinetically limited, and vice versa.

4.3.4 HYPOTHESIS 3: TEMPERATURE PROFILES FOR AMPLITUDE

The amplitude (A) of thermal oscillations defines the upper and lower bounds of the temperature cycle. Control over these isothermal zones is crucial for consistency in the equilibrium conditions when determining the effects of wave form parameters. Duty and frequency were held constant at $D = 30\ \%$ and $f = 0.01\ Hz$, respectively, to isolate the significance of changing the equilibrium condition in the high temperature region. These alterations to the temperature profile are shown in **Figure 4.5**.

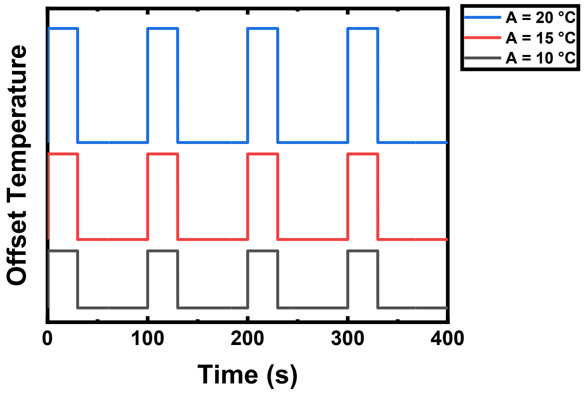

Figure 4.5: Amplitude controls the temperature change that occurs between regions within a cycle. By varying amplitude, the equilibrium condition can change in at least one of the temperature zones having direct impacts on process kinetics.

4.4 RESULTS

4.4.1 HYPOTHESIS 1: DUTY RESULTS

A parameter sweep of duty cycles revealed surprising trends in the shapes of supersaturation, nucleation, and growth rate profiles. While conventional wisdom correctly predicted super- and subsaturation depletion in each isothermal zone, as shown in **Figure 4.6**, comparing profiles from lowest to highest duty demonstrates how operating under thermodynamically limited conditions in the low temperature zone depleted the solute concentration in solution. This in turn continually regenerated high levels of subsaturation in the high temperature zones that follow. Increasing the duty cycle reallocated time for more dissolution, which replenished the concentration in solution resulting in higher levels of supersaturation. As time in the hot zone surpassed that in the cold zone, the shape of the depletion curve transitioned from a simple decay curve to a downward linear trend to finally a near square-shaped pulse. The path of supersaturation depletion had direct impacts on the crystallization kinetics as shown in **Figure 4.7**, which in turn determined the fate of the particle size distribution.

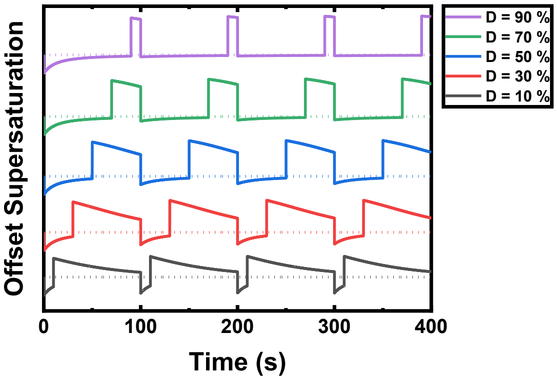

Figure 4.6: Studying the effect of duty (D) on the supersaturation profile reveals (1) there is a kinetic bias toward dissolution; (2) low duties favor thermodynamically limited nucleation/growth and kinetically limited dissolution (and vice versa); (3) increased duty kinetically limits growth and dissolution to the extent that supersaturation is nearly constant within the cold zone.

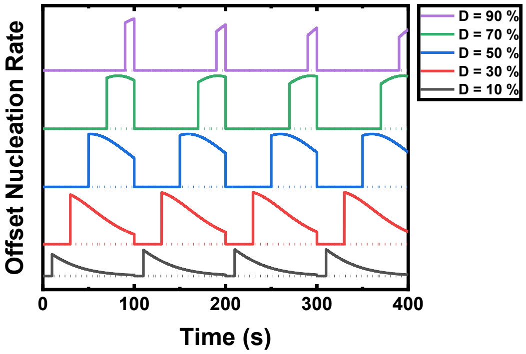

Figure 4.7: Allowing the duty (D) to vary reveals the fluidity of the nucleation rate as (1) low duty results in a standard decay profile; (2) moderate duty yields a more pronounced S curve, (3) higher duty creates a somewhat parabolic profile; (4) high duty has a complete inverse effect on rate where supersaturation depletion coincides with faster nucleation.

Nucleation kinetics reflect the amalgamation of intermolecular interactions and the supersaturation of the system. It is clear from duties $D = 10\ \%$ and $D = 30\ \%$ that kinetically limited dissolution results in generally predictable kinetics, but as time is reallocated to the hot zone, the kinetic curves become parabolic and eventually upwardly linear. This fluctuation is attributable to the loss in crystal mass overpowering increased levels of supersaturation fewer solid particles are present in the system to collide and trigger secondary nucleation. The parabolic shapes exhibit autocatalytic behavior as transience is observed in replenishment of crystal mass. Nucleation is initially slow, speeds up as more crystallites are nucleated, and finally slows again as supersaturation is depleted. Supporting data regarding secondary nucleation can be found in Appendix 2 Figure A2.3.

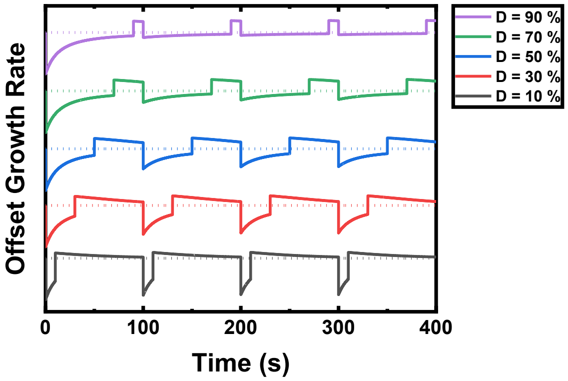

Figure 4.8: Slow growth kinetics result in a wider window of conditions that closely approach equilibrium, while options for kinetically limited dissolution are quite limited. All growth rate profiles follow a downward linear trend, while kinetically limited dissolution rates experience nonlinearity in each oscillation across all duty cycles.

Inverse ripening demands balanced amounts of growth and dissolution while simultaneously promoting a net increase in population size. Growth and dissolution each follow Arrhenius style kinetics mirroring each other across the solubility boundary as shown in **Figure 4.8**. Dissolution is much faster than growth because its activation energy is lower by an order of magnitude. Consequently, more time must be spent in the cold zone than the hot to achieve equal levels of conversion meaning a dynamic steady state is only possible when a sufficiently low duty cycle is implemented. Time resolved profiles of the zeroth moment, μ_0, shown in **Figure 4.9**, reveal trends in the population size and the effects of duty on the distribution itself. Duties of $D = 10\% - 50\%$ show a constant upward trend in population size meaning there is always a net increase in particles with each oscillation. However, results from $D = 70\ \%$ and $D = 90\ \%$ show a more unstable profile where the total population size either periodically or constantly dips below the initial population size, respectively. These results suggest that high duty cycles result in a loss of particle number density akin to isothermal dissolution, while low duty cycles drive the formation of new particles alongside competitive amounts of growth and dissolution of seed crystals setting the stage for inverse ripening and validating Hypothesis 1.

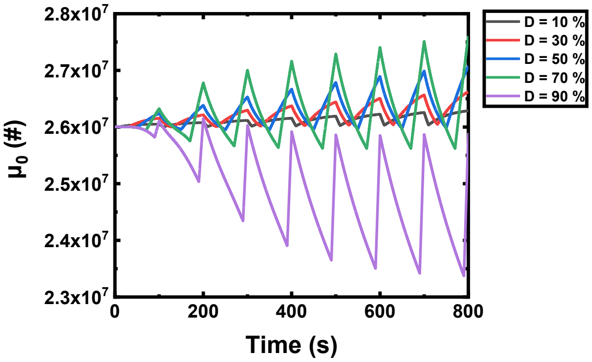

Figure 4.9: Measuring the effect of duty cycle on μ_0 illustrates the conditions that favor inverse ripening. Low duty introduces a bias to favor growth and nucleation while also providing sufficient time for dissolution to replenish supersaturation to drive the cycle indefinitely.

To further confirm the occurrence of inverse ripening, the particle size distribution was deconvoluted separating the subpopulation of initial seed crystals and the emergence of new crystallites. Individual population sizes were calculated by integrating portions of the full number density distribution as shown in **Figure 4.10**A and B solidifying evidence that lower duties produce new nuclei at the expense of seed crystals (Transient points are denoted as open symbols and are not incorporated into the model to be discussed later in the Discussion section). Raw data for particle size distributions of both hot and cold temperature cycles can be found in Appendix 2 Figure A2.4 through Figure A2.9.

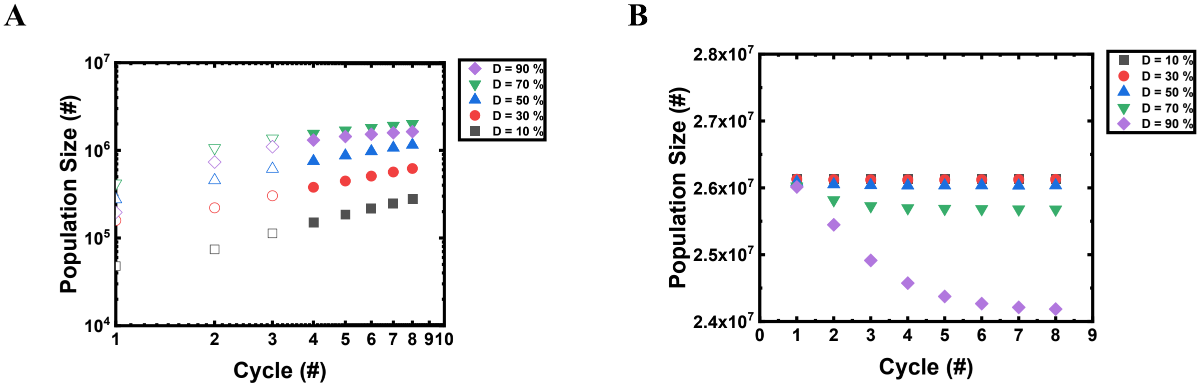

Figure 4.10: Deconvoluted population trends for a variety of duties reveals the simultaneous growth and disappearance of new nuclei and seed crystals, respectively, supporting the hypothesis that low duty cycles promote inverse ripening.

4.4.2 HYPOTHESIS 2: FREQUENCY RESULTS

Varying frequency across a series of thermal oscillations created a range of kinetically and thermodynamically limited environments. High frequency oscillations prevented the system from reaching equilibrium, which resulted in a narrow span of possible super- and subsaturation values as shown in **Figure 4.11**. This kinetically limited regime eliminated the biases in either isothermal zone yielding precise and predictable crystallization rates.

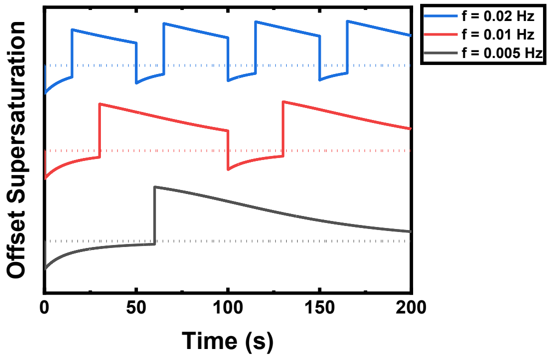

Figure 4.11: High frequency oscillations resulted in kinetically limited heating and cooling; moderate frequency oscillations had the potential for a single isothermal zone to be kinetically

limited with the other thermodynamically limited; low frequency oscillations can force each isothermal zone to become thermodynamically limited.

Nucleation profiles shown in **Figure 4.12**, followed the trends observed in the duty parameter sweep where lower frequencies allocated more time to both isothermal zones, which resulted in a wider range of super- and subsaturation values. Secondary nucleation was once again partially inhibited by excessive dissolution taking place in the hot zone and transiently restimulated throughout the cold zone. However, **Figure 4.13** demonstrates how high frequency oscillations facilitated reproducible rates of dissolution and growth alongside steady nucleation kinetics. Altogether, this supports the second hypothesis that kinetically limited high frequency thermal cycling generates rapidly changing environments that drive the nucleation needed to support inverse ripening, while thermodynamically limited slow oscillations favor traditional ripening through the complete dissolution of fine crystallites.

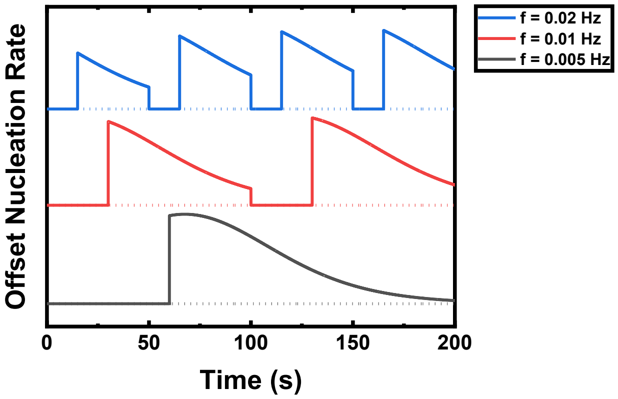

Figure 4.12: Nucleation rates varied across different oscillation frequencies depending on how close the system approached equilibrium. High amounts of dissolution generated high levels of supersaturation at the cost of dramatically reducing the crystal mass leading to nonlinear profiles.

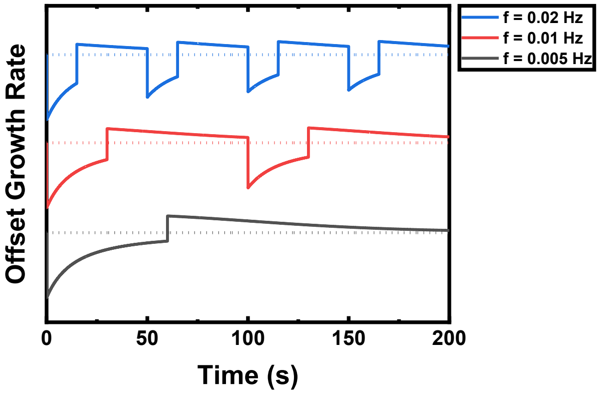

Figure 4.13: High frequency oscillations restrict the system from reaching equilibrium resulting in consistent near linear rate profiles for both dissolution and growth. Maintaining a sufficiently high driving force during each hot and cold period allows their respective kinetics to be tuned as they are constantly experiencing transience.

The zeroth moment and deconvoluted subpopulation trends shown in **Figure 4.14** and **Figure 4.15**, respectively, solidify the relationship between kinetically limited operation and number density variability across cycles. High frequency oscillations yielded small net increases in number density, while low frequency oscillations caused number density to rapidly explode. Both phenomena are again linked to the proximity to equilibrium where nearly full dissolution provides the driving force that feeds unbridled nucleation. Subpopulation trends reveal the relative stability of the seed population thereby implying the changes observed in the zeroth moment profile are mostly the result of periodic nucleation and the persistence of newly formed particles. Although the rate of growth for the nuclei subpopulation is slow, these findings suggest that repeated oscillations will continue to eliminate the seed subpopulation and feed the formation of the new nuclei. It is anticipated that the system would reach a dynamic steady state as the number of cycles approaches infinity, which would provide further evidence that kinetically limited regimes promote inverse ripening.

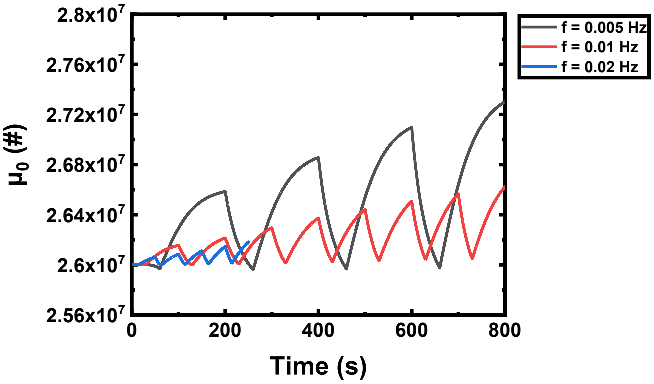

Figure 4.14: Kinetically limited operation restricts super- and subsaturation thereby constraining growth and dissolution kinetics to a controllable window resulting in a near standing wave profile for population density. When equilibrated, the population density oscillates wildly and increases without bound due to uncontrolled nucleation.

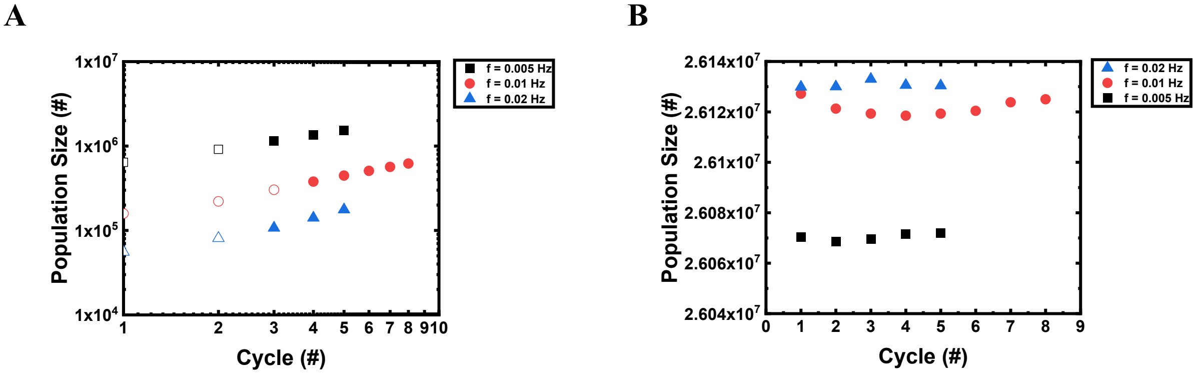

Figure 4.15: Net growth of the new nuclei subpopulation when compared against changes in the initial seed subpopulation explains upward trends in zeroth moment. Relatively consistent population size for the seed subpopulation suggests the net increase is due to particles that survived were born from nucleation and survived beyond the dissolution cycles.

4.4.3 HYPOTHESIS 3: AMPLITUDE RESULTS

Varying wave amplitude actively redefines the high temperature equilibrium condition that until this point had been fixed at a constant value. Gradually downshifting this thermodynamic endpoint narrowed the gap between the hot and cold equilibrium conditions causing three distinct effects on the processes that influence the particle size distribution. First, the degree to which a regime is kinetically or thermodynamically limited could be changed not by the time spent in each zone but solely by varying the amplitude of the wave as shown in **Figure 4.16**. Reducing the gap between the two equilibrium conditions minimizes the kinetic delay associated with releasing bound solute particles into solution resulting in a system that equilibrates faster. Second, because the initial conditions were left unchanged, a surplus, rather than deficit, of solid crystal mass was present when the system reached equilibrium at the high temperature ensuring consistently fast secondary nucleation rates as depicted in **Figure 4.17**. Furthermore, crystal mass was maintained at a high level because particle shrinkage overwhelmed elimination during hot cycles. Third, growth and dissolution rates depicted in **Figure 4.18** underwent faster decay under low amplitude oscillations because the total span of driving forces was reduced in turn severely restricting possible changes in particle size.

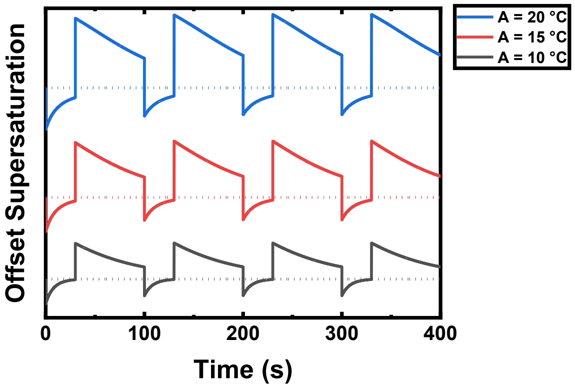

Figure 4.16: Equilibrium was reached in less time during low amplitude cycles than those with high amplitude. Despite maintaining the same frequency and duty, dissolution could be made either kinetically or thermodynamically limited depending on the amplitude.

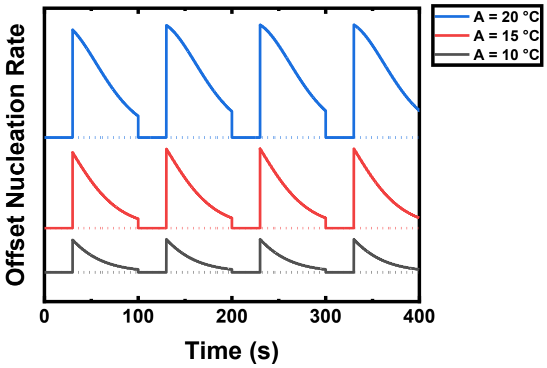

Figure 4.17: Nucleation profiles become more predictable at lower amplitudes following a decay-like downward trend as the amount of solid crystal mass remained more consistent across the span of the dynamic crystallization.

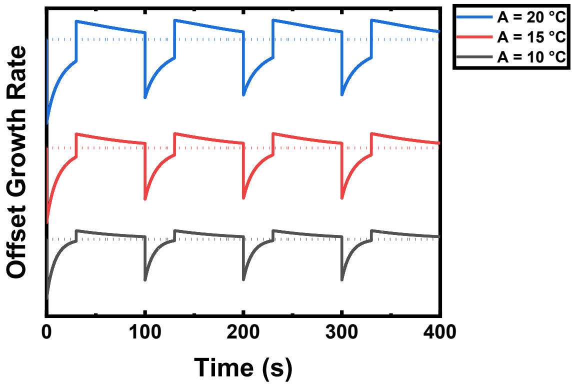

Figure 4.18: Smaller amplitude oscillations caused growth and dissolution kinetics to stall out faster as the gap between equilibrium conditions was significantly smaller.

The sum of these effects describes a nearly stable system that continually generated new particles through the gradual dissolution of seeds while avoiding significant elimination of fine crystallites. This is demonstrated in tandem between the total population size described by the zeroth moment and the number density curves for each subpopulation in **Figure 4.19** and **Figure 4.20**, respectively. Reducing wave amplitude constrained the variability in number density while maintaining an upward trend. Similarly, the subpopulation of new nuclei exhibited steady growth, while the number density of the seed subpopulation remained relatively stagnant with minor noise fluctuation. This evidence supports the third hypothesis that under low amplitude oscillations, nucleation has the potential to outpace the elimination of small particles resulting in the inverse ripening of seed crystals to fine crystallites.

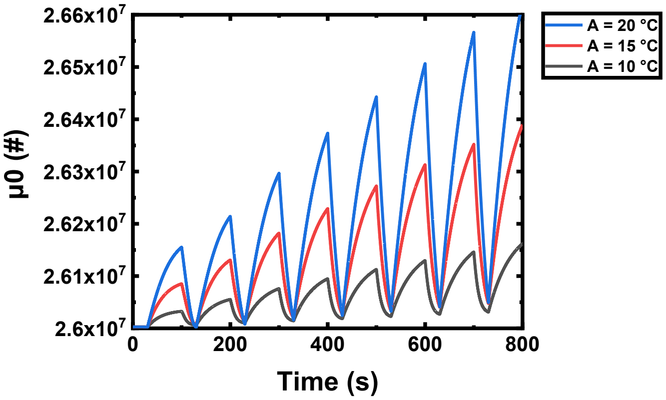

Figure 4.19: Time-resolved trends of the zeroth moment reveal how the amplitude of a square wave temperature profile directly impacted the amplitude of number density between hot and cold cycles.

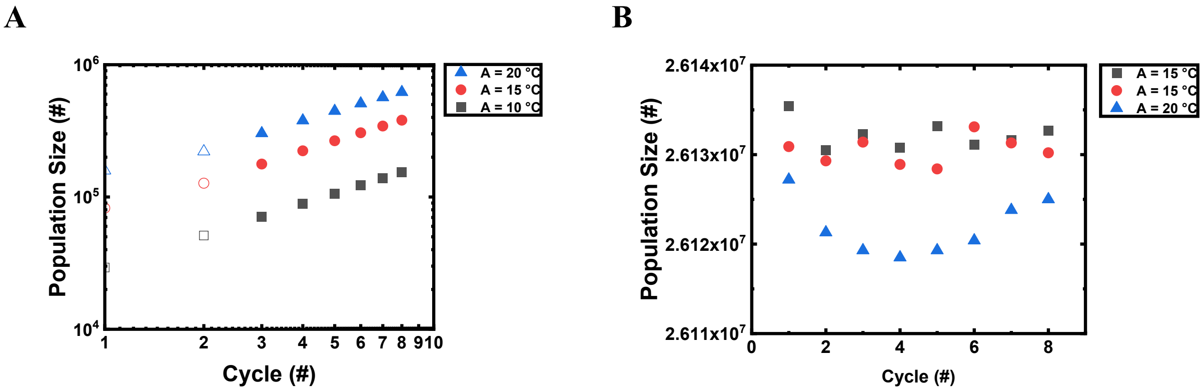

Figure 4.20: Deconvoluted population sizes prove both consistent growth of the new nuclei subpopulation and stable population size for the initial seed subpopulation.

4.5 DISCUSSION

As discussed in the Introduction section, the fourth hypothesis draws on the findings of the prior three to isolate the dynamic conditions required to induce inverse ripening. It is known that thermal oscillations in the absence of nucleation result in traditional ripening where the mass released from dissolved seeds is redeposited onto the remaining crystals resulting in a net decrease in number density and increase in average volume. In contrast, as demonstrated by Hypotheses 1 through 3, inverse ripening can be achieved by timing the high temperature zone to be kinetically limited to strategically constrain the amount of dissolution. Curtailing dissolution immediately ensures that a limited amount of supersaturation is available for nucleation and growth thus requiring that they also be kinetically limited. This high frequency loop creates an operating window of only fast kinetics and an environment that is always in flux. While these heuristics are helpful for interpreting simulation data after the fact, a more cohesive model is necessary for bridging the underlying theory to broader applications for dynamic crystallization.

Supersaturation and kinetic profiles shown in the Results section broadly demonstrate that the first oscillation generated the fastest rates and determined the initial thermodynamic position for the remainder of the simulation. This phenomenon occurred because a system that never completely equilibrates back to the low temperature condition is incapable of regenerating a driving force as high as that of the first cycle. Isolating this initial period presents an opportunity to link changes in the first cycle to the long-term behavior of the distribution. A model that uses wave parameters to make this connection has the potential to predict the trajectory of any square wave dynamic crystallization.

Determining the ratio of particles birthed (N_B) to particles eliminated (N_X) is the key to predicting if a system will undergo inverse ripening. Fortunately, calculating the number of particles added to the distribution is simply the product of the nucleation rate and the amount of time spent in the cold zone. In contrast, since oscillations begin with a shift to the hot temperature zone, it is important to calculate the number of particles that vanish upon reaching the minimum size threshold, where they are then removed from the particle size distribution.[98] Applying the average concentration in the first cycle to the dissolution rate and multiplying it by the time spent in the hot zone yields the size cutoff for particle death ($G \cdot \Delta t$). Isothermal dissolution data can be found in Appendix 2 Figure A2X. To calculate the exact number of particles removed, each bin, i, in the particle size distribution must be compared against the calculated cutoff; if the bin size, $D_{P,i}$, falls below the cutoff, then its contents, f_i, are eliminated. This process is performed using a series of dimensionless quantities whose sum can be used to quantify particle death as described by Equations (17) – (19):

$$(17)\ \alpha_i = \left[\frac{(G \cdot \Delta t) - D_{P,i}}{D_{P,i+1} - D_{P,i}}\right] [=]\ Dimensionless$$

$$(18)\ \beta_i = \begin{cases} 1\ if\ \alpha_i > 1 \\ \beta_i\ if\ 0 < \alpha_i \leq 1 \\ 0\ if\ \alpha_i < 0 \end{cases}$$

$$(19)\ N_X = \sum_{i=1}^{N} \beta_i f_i\ [=]\ \#$$

Inverse ripening is contingent upon the system experiencing a net gain in number density thus making $\left(\frac{N_B}{N_X}\right)$ an ideal predictor for dynamic system's fate. As explained in prior sections, inverse ripening is the consequence of nucleation surpassing the rate of elimination, which occurs because of a positive flux of particles into the subpopulation of fine particles. Therefore, $\left(\frac{N_B}{N_X}\right)$ can be used as a criterion for determining the mode of ripening that a dynamic crystallization system will undergo:

- $\left(\frac{N_B}{N_X}\right) > 1$: number density of the new nuclei subpopulation increases resulting in inverse ripening;

- $\left(\frac{N_B}{N_X}\right) \leq 1$: subpopulation of new nuclei does not exist causing the system to ripen traditionally.

As an aside, while the condition $\left(\frac{N_B}{N_X}\right) = 1$ is an absolute boundary, approaching this value from the right has been shown to yield elimination rates that are nearly competitive with nucleation. These antagonistic processes occurring simultaneously with extreme oscillations in growth and dissolution can cause the initial seed peak and the subpopulation of new nuclei to become convoluted. This becomes a significant, immediate issue that limits the effectiveness of the inverse ripening process. However, convolution does not necessarily spell the end for inverse ripening despite not forming a bimodal distribution. It is suspected that the long-term path is one of repeated macroscale cycles where the largest particles of the distribution are continually subjected to net shrinkage and elimination. These changes should cause the width of the nuclei subpopulation to steadily narrow and grow in intensity over time until the particle size distribution resembles an impulse peak. Previews of the particle size distribution and time-resolved μ_0 profile after 1000 cycles are shown in **Figure 4.21**:

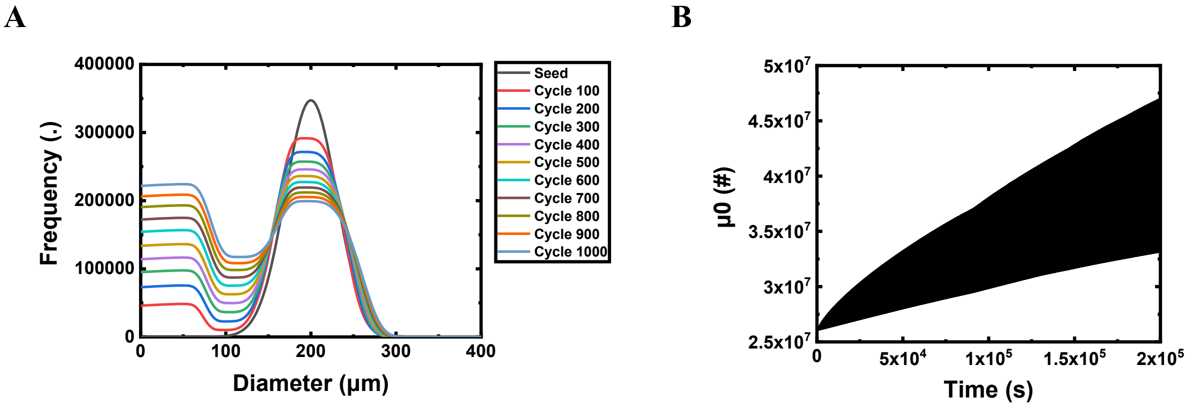

Figure 4.21: Long time simulations show the gradual disappearance and emergence of the seed and new nuclei subpopulations, respectively. This is reflected in the massive increase in number density over the course of the simulation.

All families of frequencies and amplitudes underwent $\left(\frac{N_B}{N_X}\right)$ analysis at a wide range of duty cycles, and their results are shown in **Figure 4.22** and **Figure 4.23**, respectively. All results consistently demonstrate a downward trend in $\left(\frac{N_B}{N_X}\right)$ as duty is increased as the bias toward dissolution caused greater amounts of particles to be eliminated. Kinetically limited conditions during high frequency oscillation safeguarded the nuclei from elimination, much like how smaller amplitudes maintained sufficient crystal mass to support fast nucleation rates. Both sets of dynamic conditions preserved the subpopulation of small crystallites thereby supporting Hypothesis 4 that high frequency, low amplitude oscillations create an operating window for reproducible inverse ripening.

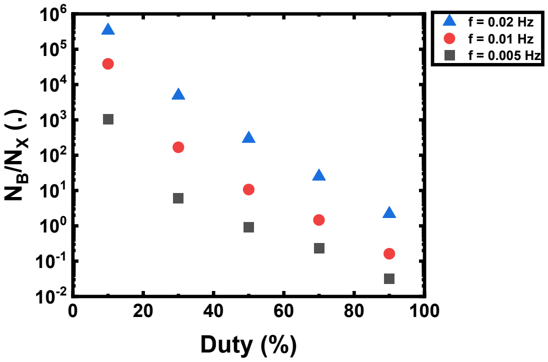

Figure 4.22: $\left(\frac{N_B}{N_X}\right)$ analysis shows a tendency for kinetically limited cycling to favor inverse ripening $\left(\left(\frac{N_B}{N_X}\right) > 1\right)$, while thermodynamically limited cycling favors traditional ripening $\left(\left(\frac{N_B}{N_X}\right) < 1\right)$.

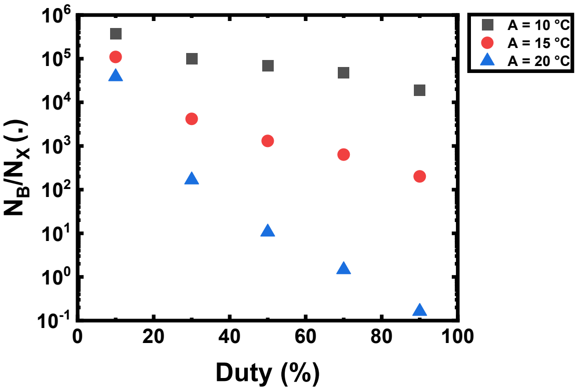

Figure 4.23: $\left(\frac{N_B}{N_X}\right)$ analysis demonstrates that narrowing the thermodynamic limits of the dynamic system favors inverse ripening $\left(\left(\frac{N_B}{N_X}\right) > 1\right)$.

Hypotheses 1 through 3 output a series of subpopulation curves whose dynamic steady state values were empirically fitted to power functions described by Equation (16). Importantly, while parameters k and b hold no derived physical meaning, their relative values across datasets hold pseudo-kinetic information connecting the experimental trajectory of the particle size distribution and the theoretical prediction of a system's fate with respect to ripening. Kinetic parameters k and b represent the intercept and slope, respectively, on the log-log plots shown in **Figure 4.24** and **Figure 4.25** for parameter sweeps of frequency and amplitude, respectively. After parsing out data where $\left(\frac{N_B}{N_X}\right) < 1$ (shown as empty markers on plots), interesting relationships between parameters k and b and the waveform parameters were revealed. Although high frequency waveforms began with the smallest number of new nuclei, the population's growth rate was drastically higher than the lowest frequency counterpart (similar trends were observed when decreasing amplitude). Trends for each kinetic parameter tended to follow a parabolic curvature until the system approached conditions where $\left(\frac{N_B}{N_X}\right) < 1$. The detectability of this key distinction means these experimental results could provide an extra layer of robustness to a predictive ripening model.

$$(16)\ p = km^b$$
$$\log p = \log k + b \log m$$

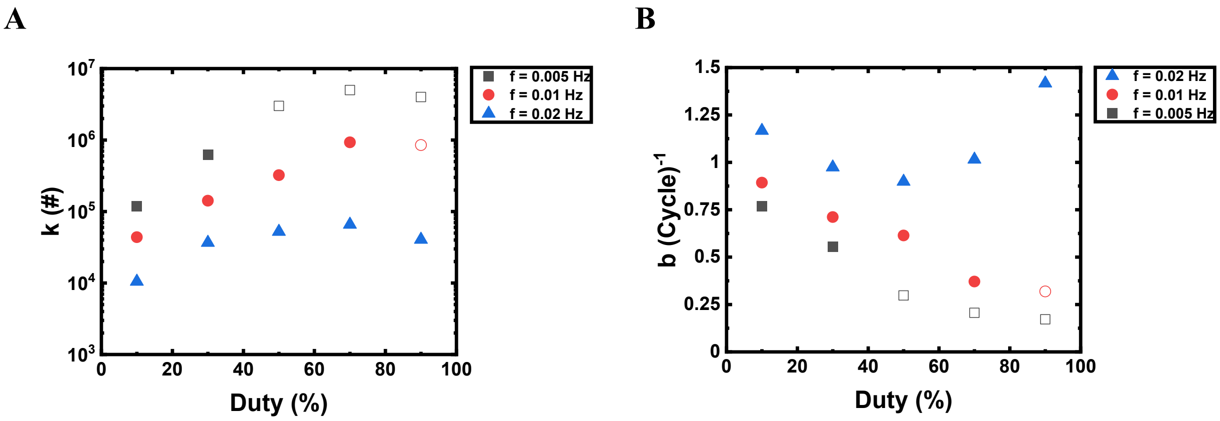

Figure 4.24: Despite starting at the lowest size, high frequency oscillations generate the fastest growth of the nuclei subpopulation.

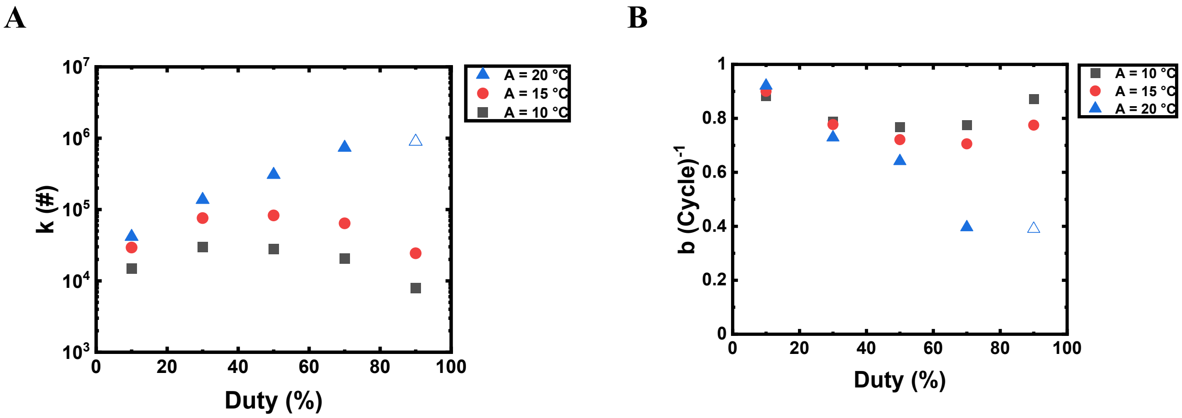

Figure 4.25: Decreasing amplitude both ensures inverse ripening and results in subpopulations that are both large and exhibit rapid growth.

The comprehensive findings discovered through the validation of Hypothesis 4 take shape in the dynamic ripening model effectively bridging the gap from theoretical calculations to experimental data. This model is composed of a series of cohesive regime maps each spanning the set of dynamic parameters studied in this manuscript. Versatility comes in the bidirectional nature of the model such that a user may begin in one half and work their way to the other and vice versa. For example, if the user wishes to understand how a dynamic system of a given duty and frequency/amplitude might behave, they will start in either **Figure 4.26** or **Figure 4.27** to ascertain the magnitude of $\left(\frac{N_B}{N_X}\right)$ and apply the criterion for ripening to determine whether traditional or inverse ripening will occur. From there, those same dynamic parameters are then input into **Figure 4.28** or **Figure 4.29** to determine the kinetics associated with the growth of the new nuclei subpopulation. Reversing these steps, i.e., starting from a desired experimental outcome and working toward possible dynamic parameters, is also possible with the caveat that some iteration may be required. If a set of experimental kinetics leads to a set of dynamic parameters that do not satisfy the criterion for inverse ripening, then those kinetics are not feasible and must be revisited and adjusted. Overall, this approach to understanding and predicting inverse ripening is an exciting beginning truly only the first step in what will shape the future of dynamic crystallization.

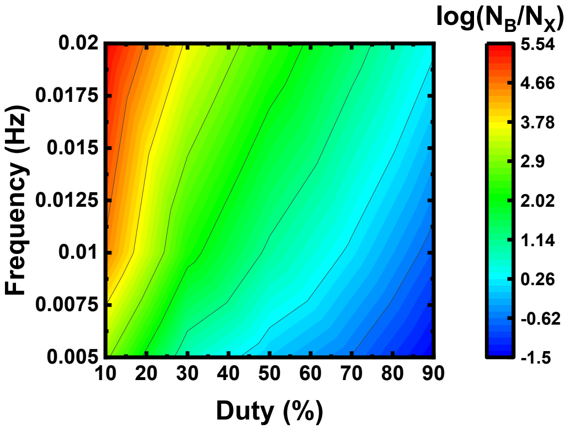

Figure 4.26: Regime map for $\left(\frac{N_B}{N_X}\right)$ as a function of both **frequency** and **duty** to determine the ripening fate of the dynamic system.

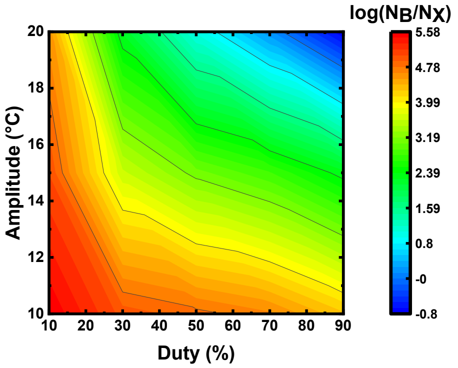

Figure 4.27: Regime map for $\left(\frac{N_B}{N_X}\right)$ as a function of both **amplitude** and **duty** to determine the ripening fate of the dynamic system.

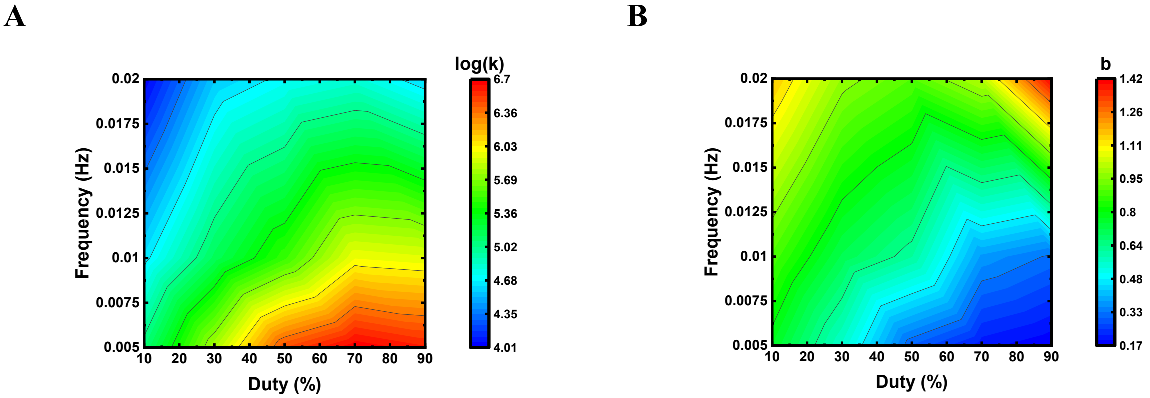

Figure 4.28: Regime maps for population growth kinetic parameters k (A) and b (B) as functions of **frequency** and **duty** to determine the trajectory of the dynamic crystallization system.

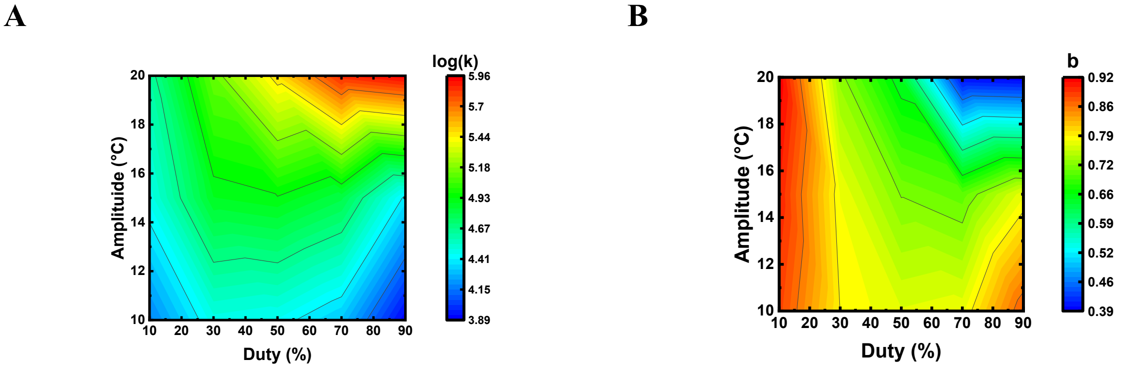

Figure 4.29: Regime maps for population growth kinetic parameters k (A) and b (B) as functions of **amplitude** and **duty** to determine the trajectory of the dynamic crystallization system.

4.6 CONCLUSION

This project utilized the high throughput benefit of population balance modeling to simulate a series of dynamic crystallization systems each overlaid with a unique square wave temperature profile. A sensitivity analysis on various waveform parameters, including duty, frequency, and amplitude, revealed the benefits of operating in kinetically limited regimes. By directly controlling the driving force through kinetic locking or manipulating the thermodynamic limits of the system, a wide breadth of conditions was generated that exhibited three different ripening motifs: inverse ripening, traditional ripening, or a convolution of the two. Correlating these results to a theory-based calculation of particle birth and death laid the groundwork for a comprehensive dynamic model to both predict the occurrence of ripening and correlate its kinetics to the input waveform parameters used for its temperature profile. The model is based on the following criterion for ripening, where N_B is the number of particles birthed and N_X is the number of particles eliminated:

- $\left(\frac{N_B}{N_X}\right) > 1$: number density of the new nuclei subpopulation increases resulting in inverse ripening;
- $\left(\frac{N_B}{N_X}\right) \leq 1$: subpopulation of new nuclei does not exist causing the system to ripen traditionally.

While these results are encouraging, this model is only the first step in accessing the full potential of dynamic crystallization. Introducing further layers of complexity would both make the model more robust and better equipped to mirror crystallization in the real world. First, reperforming the analysis described in this work simply with differently structured kinetic models would provide flexibility to the final model.

Second, incorporating more nuanced aspects of real-world crystallization, such as particle breakage and agglomeration, intermolecular effects between solute and solvent molecules, and allowing for multicomponent crystallization, would provide insight into kinetic behavior on the molecular level and help elucidate the underlying crystallization mechanism. Third, relaxing the assumption of size-dependent growth would test the sensitivity of the $\left(\frac{N_B}{N_X}\right)$ calculation and subpopulation growth kinetics. This could be achieved by introducing a hard-coded bias into the kinetic model, such as factoring in an expression that favors the growth of larger particles, or changing the growth model more broadly to one that reflects a growth rate dispersion. Lastly, expanding the population balance model to solve for higher dimensions of crystal growth would open the door to understanding how different polymorphs behave in dynamic environments. Further development of this model has the potential to change how we understand crystallization and how we use it to solve our most pressing technological challenges.

FUTURE DIRECTIONS, RECOMMENDATIONS, AND BROADER IMPACTS

FUTURE DIRECTIONS

The common throughline in each of these crystallization projects is developing new means of achieving enhanced control over the crystallization environment to learn more about the underlying mechanisms and unlock new operating windows. In this recapitulation section, each project will be addressed individually concerning immediate follow up work.

1. Zeolite Synthesis: While the microbatch work represents a major advancement in understanding the heat transfer scaling relations in zeolite synthesis, a set of design iterations could revolutionize the field with a fully continuous zeolite crystallization. First, the annular region of the droplet generator contains a bottleneck that is always under threat of clogging, which severely hinders the robustness of the reactor. Uncontrolled reagent mixing raises the risk of inaccurate feed proportions, premature gelation, and hydrodynamic failure.

   Alternatively, the microdroplet generator could be restructured such that instead of a sol-gel mixture being sheared into a dispersed microdroplet, each reactant could be fed to the crystallizer by separate segmented flow streams. This extra degree of freedom would allow the total volume and aspect ratio of the sol-gel droplets to be tuned to achieve desired feed ratios and residence times. Each stream of microdroplets would intersect a midline oil stream that would not only induce mixing of the two reagents but also increase the inert space between sol-gel droplets preventing undesired coalescence. Furthermore, this extra layer of control and flexibility would expand the operating capabilities to be able to handle more complex chemistries by teeing in additional reagent streams at different points along the crystallizer.

2. Flow Crystallization: Achieving reproducible hydrodynamics and preventing undesired secondary nucleation is possible with the correct preparation protocol. First, the system should be brought to and held at $60\,°C$ and flushed with ethanol. Ethanol serves as an effective cleaner because of its high paracetamol solubility and is miscibility with the carrier oil. This hot wash releases built up pockets that have deposited on the tubing walls that would either nucleate new crystals or obstruct the flow path. Next, the channels should be flushed with DI water to remove any excess ethanol that would otherwise disrupt the flow of oil and microdroplets. Then, the flow path should be primed with oil to uniformly coat the walls and eliminate wall effects inside the aqueous phase. Lastly, while still at the hot temperature, the mother liquor can finally begin to be sheared into microdroplets to establish stable hydrodynamics throughout the entire body of the crystallizer. While this procedure eliminates the issue of uncontrolled/unreproducible secondary nucleation, the lack of agitation within a microfluidic device means the system must rely wholly on primary nucleation to generate crystals, which is an extremely slow process. This could be circumvented by packing the inside of the flow channel with an immovable seed crystal that would promote further nucleation without itself growing out of control and causing a clog.
3. Ripening Via Dynamic Crystallization: While the regime maps created at the end of Chapter 4 are powerful for predicting the occurrence of ripening, tracking only the number density of a crystal population provides limited information on the product quality. Therefore, the next steps for this model include the incorporation of kinetic outputs related

to peak height and broadness as well as average particle sizes for the new crystallite populations. From there, a broader range of amplitudes and frequencies should be tested and incorporated into the regime map both for validation and increasing model accuracy. Furthermore, changing the initial conditions, especially the particle size distribution of seed crystals should have direct impacts on the criterion for ripening since the seeds provide the nutrients required to drive the formation of new particles. Lastly, increasing the complexity of wave forms should expand the applicability of the model and allow the system to experience a more diverse domain of operating conditions.

RECOMMENDATIONS

1. Zeolite Synthesis: Although deemed more an art than a science, a kinetic study at the various stages in zeolite synthesis would demystify this ambiguous process. The aging process is a perfect opportunity for systematically studying the changes occurring in each phase since the process usually takes place at room temperature. Understanding the intra- and intermolecular behavior of aluminosilicate precursors before they crystallize would deconvolute the strong interaction effects that exist between the two phases.

   It is well documented that the liquid phase contains subunits that undergo dehydration and polymerization reactions with each other and with functional groups on solid surfaces. Therefore, separating the phases and studying their kinetic behavior individually facilitates the elucidation of any thermodynamic, kinetic, or transport barriers that impede fast crystallization. This in situ deconvolution would require a new generation of reactors potentially involving membranes with selective permeability to suspended aluminosilicates distinctly different from the bulk solid. A flow crystallizer would be the ideal platform for this study as small microdroplet control volumes would be straightforward to flow, mix, and potentially trap in place for more intense study.

2. Flow Crystallization: The largest barrier to commercially scalable flow crystallization is the challenge of handling the constantly changing solid phase, which is where the utility of segmented flow truly stands out. When stable segmented flow is achieved, the crystals remain suspended as the advective force of the moving fluid carries them throughout the reactor. This becomes increasingly challenging at larger length scales as the instability of individual droplets increases, which threatens droplet breakup, undesired wall effects, and irreproducible hydrodynamics. A simple means of circumventing these scaling challenges is the number up method where microfluidic segmented flow crystallizers would be run in parallel to achieve competitive throughput.
3. Ripening Via Dynamic Crystallization: The future of wave-based dynamic crystallization lies in machine learning. The combinations of dynamic parameters for square wave temperature profiles are nearly endless as each parameter sweep could be a full factorial study. Simulating these conditions with population balance modeling has the potential to generate enough data to train a model to construct wave patterns based on a desired outcome. This arbitrary wave form would be extremely powerful as achieving this level of kinetic resolution could unlock the ability to ripen entire populations into a desired product with a tailor-made particle size distribution and yield.

BROADER IMPACTS

For the last few decades, advancements have been made in our ability to detect changes down to the molecular level and use that information to exert extreme levels of control over the crystallization environment. While in the past these motifs have been limited to feedback loops, the field is shifting toward a more proactive position where underlying kinetics rather than empirical data are informing operating decision making. This is seen in a number of studies that match thermal cycling to experimental data, which is then in turn explained mechanistically using population balance modeling. Dynamic crystallization is the past, present, and future of this field of research because it represents the pinnacle of control over crystallization kinetics and thermodynamics.

Ushering in this new era of crystallization will require modern methods for technical education and training. The following afterword chapter discusses the implementation of augmented reality in the undergraduate chemical engineering curriculum highlighting the importance of experiential learning by visualizing the underlying theory of real-world processes.

CHAPTER 5

ENHANCING STUDENT ENGAGEMENT IN UNIT OPERATIONS LABORATORY THROUGH AUGMENTED REALITY

5.1 ABSTRACT

A chemical engineering student's knowledge of theory, experimental design, and real-world processes is tested and enforced in the Unit Operations laboratory courses. However, instructors are facing challenges of delivering high-quality, hands-on laboratory content with limited resources and increasingly large class sizes. Limited in-lab time is often inefficiently allocated to individualized instruction, which broadly diminishes students' opportunity for learning by restricting the quantity of data they are able to collect. In addition, teaching in-person laboratories with social distancing measures during the pandemic posed significant logistical and safety challenges and required alternative techniques to be explored and adapted. The technological strategies implemented in this work aimed to manage laboratory course content more efficiently by enhancing familiarization, operation, and safety of lab equipment during and prior to class time. This work demonstrates the evolution of several technological tools that evaluated synchronous hybrid lab offerings and asynchronous prelab training using remote controlled cameras, web-interfaces, and augmented reality. The effectiveness of the implemented technologies was assessed via post course surveys and both negative and positive students' responses were discussed.

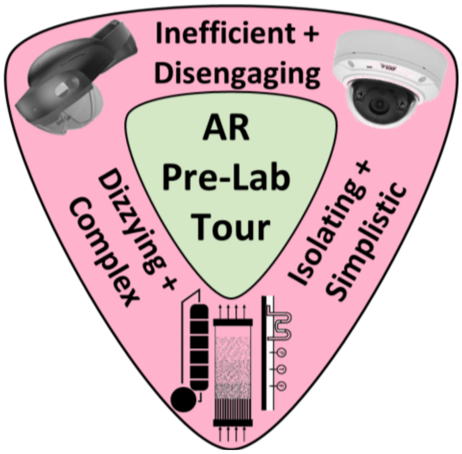

Figure 5.1: Graphical abstract illustrating the synergism of augmented reality as an educational tool. Augmented reality as a pre-lab tour immerses students in experiential learning in a way that is both fun and informative.

5.2 INTRODUCTION

The Chemical Engineering Unit Operations (UO) course is the culmination of the chemical engineering curriculum, bridging the gap from classroom theory to the real-world industrial processes.[99] In the laboratory course, students participate in various stages of experiential learning including conceptualization and experimentation followed by reflection, analysis, and interpretation of data.[100] Students apply the theory learned from other courses to enforce the underlying principles at play.[101] While equations of conservation of mass and heat transfer always hold, their conceptual and quantitative adoption to real processes must first be reconciled with the physical actions of rotating a valve or reading a temperature gauge before the content is mastered.[100]

Maintaining this safe and dynamic learning environment demands infrastructure, significant training, time, and resources.[102] These factors challenge educators to effectively deliver resource-intensive course content, especially in the wake of the COVID-19 pandemic as instructors urgently transitioned to either a fully virtual or limited hybrid instruction to mitigate the disruption.[103] Chemical engineering departments around the world brought forth several solutions to foster engaging UO experiences: in-person de-densification[104], hybrid in-person and synchronous remote lab teams[105], recorded asynchronous videos of instructor-run experiments for remote observation[106], and completely virtual simulations of lab experiments.[107,108] Notably, many of these solutions came at the sacrifice of experiential learning, an element that has proven to be most effective through in person labs[109], followed by simulations[110], and finally videos.[111] Increased demands on faculty time compounded with limited access to lab space warranted dramatic steps to pivot crucial aspects of the course e.g. lab content, tours, prelab reports, and faculty conferences, to more accessible alternatives.

Augmented reality (AR) systems superimpose a virtual space onto the user's three-dimensional real-world environment via a hologram projection. An array of sensors and supporting algorithms constantly map the space viewed through the transparent lens of a computerized headset. From the point of view of the user, their surroundings now contain holograms corresponding to specific AR functionalities that can be spatially anchored to real-world structures with high precision and reliability to effectively create a mixed reality experience.

As an educational tool, AR has only been recently implemented for higher education.[112] The potential efficacy of AR is realized when the interface between the physical and virtual worlds are leveraged together to form an experiential immersion into a mixed learning environment not possible by either individually.[113] Traditionally unidirectional activities, such as refinery facility tours, chemistry lab safety training, and industrial equipment troubleshooting, are evolving to incorporate user interactivity.[114] In a quasi-virtual setting, medical students implemented AR to interact with virtual three-dimensional objects ranging from single protein structures to full scale organs as they relate to the human body.[115–118] AR can improve students' understanding and expand accessibility through the blending the expertise of their instructors with the theory, models, and machinery of the system at hand.

In this work, AR programs via the Microsoft Hololens 2 were implemented as part of the UO course in the chemical engineering department at a private east coast university. University-wide undergraduate student demographics are as follows: White (74.8%), Asian (11.8%), Hispanic/Latino (10.1%), Black/African American (3.2%), and American Indian/Alaska Native (0.02%). While demographics are not tabulated for the Chemical Engineering department, or more specifically the CHE4401/CHE4402 courses or survey responders, the departmental demographics are consistent with the university-reported distributions. The AR technology was employed to complement the in-lab experience for both synchronous hybrid laboratory operation and asynchronous pre-laboratory training. In the synchronous hybrid format, AR enables students to engage and experience the experiment in real time. In contrast, employing AR as part of the asynchronous pre-laboratory training allows students to visualize theoretical concepts and safely explore the lab equipment beforehand. Additionally, future AR use in the curriculum is critically discussed to highlight the potential synergy between the course content and the technology.

5.3 MATERIALS AND METHODS

5.3.1 UO LABORATORY COURSES

The Unit Operations laboratory is a three-story, 6,000 square foot pilot scale facility. It houses over 18 individual unit operations, of which nine were used in the context of this study: fluid (water) flow circuit, gas flow apparatus, packed tower, fluidized bed, membrane separator, reaction scale-up, temperature control, plate heat exchanger, and pipe heat exchanger. The aforementioned experiments are part of the senior-level core undergraduate Unit Operations of Chemical Engineering I course (CHE4401), which explores traditional bench scale and pilot scale chemical engineering unit operations. It is a primer for the more intensive Unit Operations of Chemical Engineering II course (CHE4402) which looks at more integrated systems. The course operates three times per week, with student groups of four to five members. Deployment of the AR modules occurred over two years (Fall 2020 and Fall 2021). A rotation was implemented such that each group would run a single unit operation during one, four-hour lab session each week, having pre- and post-lab reports due immediately prior to and one week after completing each lab, respectively. The first, third, and last weeks of the seven-week course were reserved for orientation and oral presentations, resulting in a total of four labs run per course per student group.

Several innovative technologies were introduced to develop a comprehensive hybrid teaching laboratory with augmented reality components. The lab was first outfitted with 10 high-definition pan-tilt-zoom cameras (Axis Communications P3375-V 1080p), which were carefully mounted throughout the three-story lab to provide synchronous remote controls. In the second year, the cameras were integrated into a user-controlled web interface (Gather.Town), which allowed remote access to the facility both synchronously and asynchronously. In addition, Gather.Town, a virtual online platform equipped with synchronous meeting spaces and demonstration videos, was used to offer expert introductory tours of lab equipment that students could access on their own time and at their own pace, as shown in Figure 5.5.

The second major piece of technology used was the Microsoft HoloLens 2 (HL2) augmented reality glasses. The HL2 glasses were mounted to the base of hard hats using Velcro straps, and used in conjunction with safety glasses, as per the safety requirements of the open bay laboratory. For sanitation reasons, the glasses were washed down with isopropyl alcohol using microfiber cloths after use, then sanitized by ultraviolet radiation for 60 seconds in a Cleanbox CX1 per manufacturer instructions. The HL2 were preloaded with Microsoft Guides and Microsoft Remote Assist.

To summarize, in the first year Microsoft Remote Assist was used on the HL2 for synchronous streaming into a Teams meeting; remote access to PTZ cameras was administered through Teams. In the second year, HL2 was strictly used asynchronously with Microsoft Guides prior to the lab period; PTZ cameras were integrated into Gather.Town alongside embedded video tutorials.

Assessment of the implemented technologies was performed at the completion of the 7-week term via post-course surveys after the second year of implementation. Optional surveys were conducted using Qualtrics web interface to gauge the overall student reception of the AR technology used in the course. Complete responses were obtained for 21 out of the 89 students enrolled in the second year; the approximately 1 in 4 response rate can be attributed to the hectic nature of the transition period between academic terms and the fact that not all students who participated in CHE4401 ended up enrolling in CHE4402.

5.3.2 REMOTE MEETINGS AND LAB INTERFACING

Remote Assist was used in conjunction with Microsoft Teams in the first year of deployment to facilitate real time phone calls between students in lab wearing HL2 and remote students. The student wearing the HL2 headset worked with a groupmate in lab to operate the experimental equipment and to relay process information while communicating with remote students and instructors via a Microsoft Teams call.

Remote students could view the unit operation both through the point of view of the HL2 as well as through high-resolution PTZ cameras allowing remote students to process the raw data in parallel and recommend adjustments. Real time analysis by remote students was performed in Microsoft Excel that was shared on Microsoft cloud, but also holographically streamed during meetings to the lab HL2. The user-controlled web interface Gather.Town was introduced for further visualization of the equipment. Each piece of virtual equipment was supported with asynchronous introductory video tours and synchronous meeting spaces for students to use at their own pace.

5.3.3 GUIDES PROGRAMMING

Guides were constructed within the Microsoft Guides desktop software (version 603.2107.20001.0) to asynchronously teach key aspects for each of the nine unit operations. Figure

5.2 illustrates a side-by-side view of the programmer during the construction of the Guide and placement of the holograms in physical space tailored to their specific purpose.

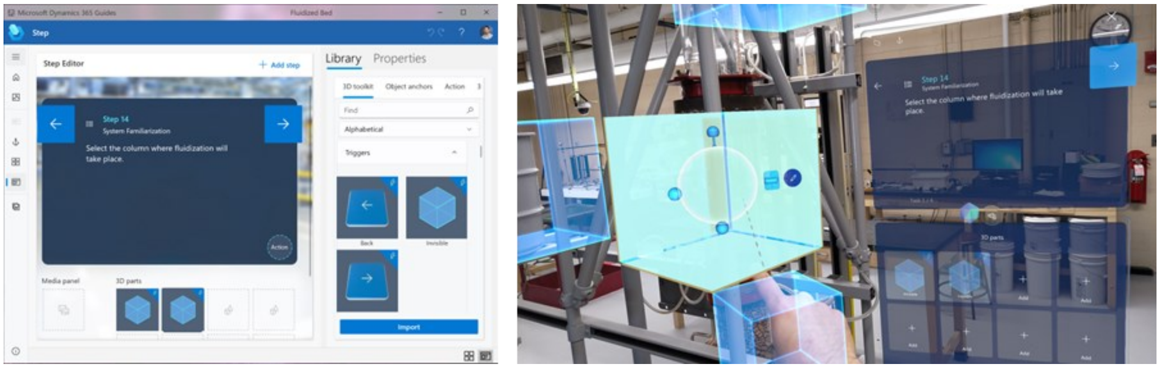

Step 14
System Familiarization
Select the column where fluidization will take place.

Figure 5.2: Programing in Microsoft Guides. (Left) desktop program writing the prompt, selecting holograms/graphics and defining actions (invisible buttons). (Right) view from programmer placing the invisible buttons in lab for the correct and incorrect selections. Buttons are shown as blue holographic boxes for programming purposes; they are invisible during student-mode.

The logic diagram depicted in Figure 5.3 was designed to ensure each Guide covers course objectives. When beginning a new Guide, a two-dimensional QR code is set to anchor the Guide in the real world. Each successive chapter tests hardware familiarization, procedure (e.g. startup, runtime, shutdown), core engineering concepts, and operational safety. Within each chapter, a series of prompts engages the user with either information or task-based questions in the form of holographic cards superimposed over the experimental setup.

Informational prompts are presented as text cards, pictures, videos, or holograms about the specific topic, while Multiple Choice questions provide the user with a bulleted list of selectable text answers. Identify tasks direct the user to physically reach out and touch objects in the lab, which are linked to holograms that are shown as blue boxes in author mode (programmer view) and invisible in operator mode (user view), as shown in Figure 5.2. Supplemental video tutorials, equipment schematics, background theory graphics, and model animations were produced separately and integrated throughout each Guide to promote visualization and facilitate critical thinking. From a user experience, Guides only reacts to user inputs, such as selecting an object, requesting a hint, or going backward. Furthermore, forward progress can only be achieved by selecting the correct answers or identifying the correct components. When implemented as a pre-laboratory activity, the AR Guide delivers the professors' expertise in a tailored training module to streamline the students' in-lab experience thereby expanding what is possible within the limited four-hour lab period.

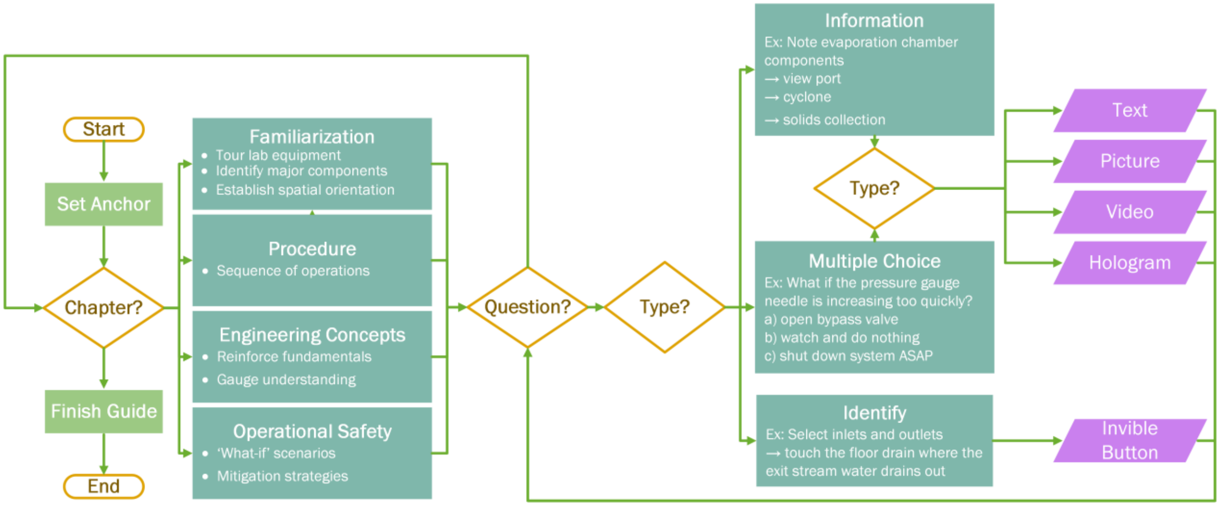

Figure 5.3: Logic diagram used for programing unit operations in Microsoft Guides.

5.4 RESULTS AND DISCUSSION

5.4.1 SYNCHRONOUS HYBRID LAB OPERATION

AR in UO was first implemented to expand lab accessibility during the COVID-19 pandemic by enabling remote users to actively engage with their in-person lab partners for safe hybrid operation. One in-person user per group wore the HL2 to stream their real-time point of view to their remote counterparts, while their partner primarily operated the experimental equipment in lab with instructor supervision similar to the strategy executed at Hampton

University.[107] Two other teammates were remote, operating cameras and participating in a Microsoft Teams meeting. The role of the remote users was to primarily perform calculations in real time and make recommendations for operating parameters. These roles within the team would be alternated weekly following the semester schedule of experiments while accommodating COVID-19 de-densification and quarantine protocols. Figure 5.4 shows a screen capture from a remote user receiving a live feed from HL2 wearer. In addition to video calling, synchronous data analysis performed in Microsoft Excel by remote users is shared via holographic projections in the video call. A video demonstration of AR Remote Assist during CHE4401 has been posted for public viewing on Youtube.com.[119]

Synchronous AR was scaled back in the second year, while hybrid learning resources were expanded to enhance the learning of students who were unable to attend the course in person. The online Gather.Town platform shown in Figure 5.5 had a streamlined interface, offering students uninterrupted access to virtual private areas for remote meetings and a virtual two-dimensional floorplan of the UO lab equipped with strategically placed PTZ cameras.

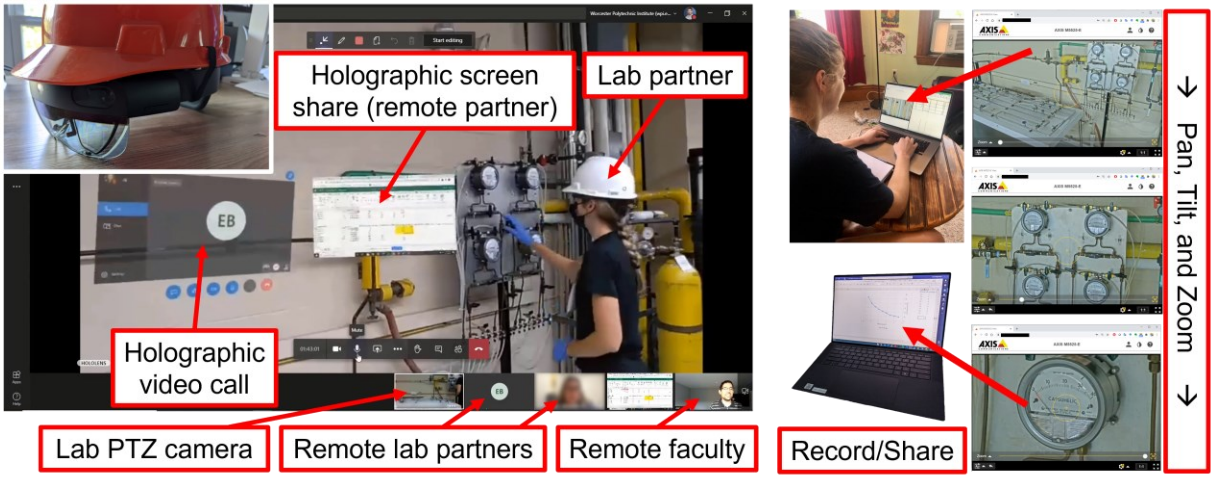

Figure 5.4: Left: Screenshot from remote user showing view from student wearing the HoloLens 2. Holograms of the video call and screenshare (Excel spreadsheet) are superimposed onto the lab apparatus. A second student is in lab conducting experiments, and two remote students and

one faculty member are on the Teams call. Right: Lab camera is also being streamed by one user. Top Left: photograph of HoloLens 2 fixed beneath bump cap.

5.4.2 SYNCHRONOUS OUTCOMES/DISCUSSIONS

Synchronous implementation of AR via Microsoft Remote Assist, Excel, and Teams was met with successes and setbacks. Overcoming the obstacles of substantial occupancy limits and forced remote work for students and professors due to COVID-19 isolation was by no means a small task. Doing so allowed remote students to actively engage in the experiment and cultivate cooperative group dynamics that are paramount to the UO course.[105] However, technical and logistical challenges persisted in the launch of the synchronous AR. Licensing and login procedures resulted in substantial in-class delays, up to 20 or 30 minutes in some cases. Prolonged streaming also quickly depleted the HL2 battery, limiting the user to <2 hours of continuous operation. Furthermore, stationary remote-controlled PTZ cameras were preferred over a continuous first-person feed as head motion by the HL2 operator often caused chaotic, dizzying video streams. Consequently, identifying that the AR technology benefited the HL2 wearer over the remote users motivated the omission of synchronous headset streaming in favor of a more concentrated offline experience in subsequent course offerings.

Notably, however, the UO lab remained loud, so video chatting worked best with Bluetooth headsets. In both years, remote students were most engaged with data analysis and periodic discussions with students and faculty, though some groups did opt to also have them perform data collection when reasonable. More creative methods for remote engagement can explore more heavy integration with LabVIEW or similar automation platforms, though automation was intentionally minimized in most units in CHE4401 in favor of physical controls for pedagogical reasons.

5.4.3 ASYNCHRONOUS PRELAB EXPERIENCE

The disruption and subsequent adjustments made in response to the COVID-19 pandemic revealed that initial in-lab familiarization was a consistent bottleneck in facilitating the resource-intensive UO course. Rather than continuing to consume valuable in-lab time with hybrid techniques, a more sustainable pedagogical approach was sought to take advantage of pre-lab time to deliver course content asynchronously while promoting deeper understanding of the UO experiments.

High precision PTZ cameras capable of resolving millimeter-scale measurements were coupled with video tours and made available to students via the Gather.Town platform shown in Figure 5.5. Floor maps from Gather.Town (left) as well as a larger view of the 1st floor are listed with one participant engaging with a lab camera. The camera feed is shown inlay (top middle), while embedded faculty videos are distributed throughout the map, and stream when engaged (top right). A video tutorial outlining the navigation and operation of the Gather.Town platform has been posted for public viewing on Youtube.com.[120]

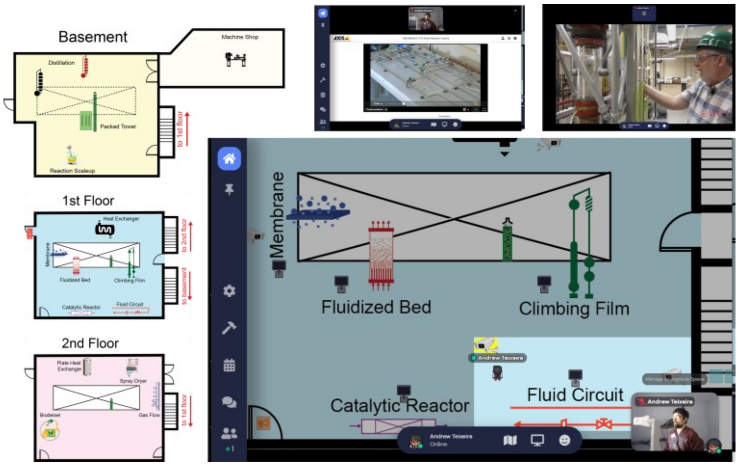

Figure 5.5: Students 'walk' through a map of the UO lab in Gather.Town web interface with embedded pre-recorded video tours from faculty (top right), live PTZ cameras (top middle), and synchronous group video conferencing space (main window).

AR Guides were interactive tutorials designed to simultaneously teach and test familiarization of a given unit operation prior to their scheduled lab period. Guides were written to sequentially lead the user through a hands-on tour of the equipment underscoring key components involved in operation, startup and shutdown, theory, and lab safety. Text, pictures, videos, and holograms (arrows, circles, boxes, etc.) supplemented tasks where appropriate. Guide development is outlined in Figure 5.3, and each element of Figure 5.6 highlights characteristic aspects of the user experience as they relate to course objectives. Invisible buttons depicted in Figure 5.6A required the user to physically reach out and touch the regulator used to control the steam pressure. Pre-lab AR tours were strategically designed such that even when the Guide did not directly require physical action, the user was still interacting with course content as depicted in the instructor-led video describing startup procedures featured in Figure 5.6B. Conceptual questions were introduced typically as multiple choice, often aided by metadata shown holographically as a picture. Figure 5.6C shows an example of this where the student observes a marked-up Ergun equation and is prompted to analyze the expression. Finally, safety was introduced by asking students to identify hazards, select relevant personal protective equipment, or reflect on potential ‘what-if’ scenarios that could occur in the lab. Figure 5.6D demonstrates an example of a student being tested on responding to a flooding column and how to drain it before it overflows. A holographic arrow and holographic hand reveal the necessary mitigation steps needed to be performed on the physical column to the user. A walkthrough of Guide design and hologram placement has been posted to Youtube.com for public viewing.[119]

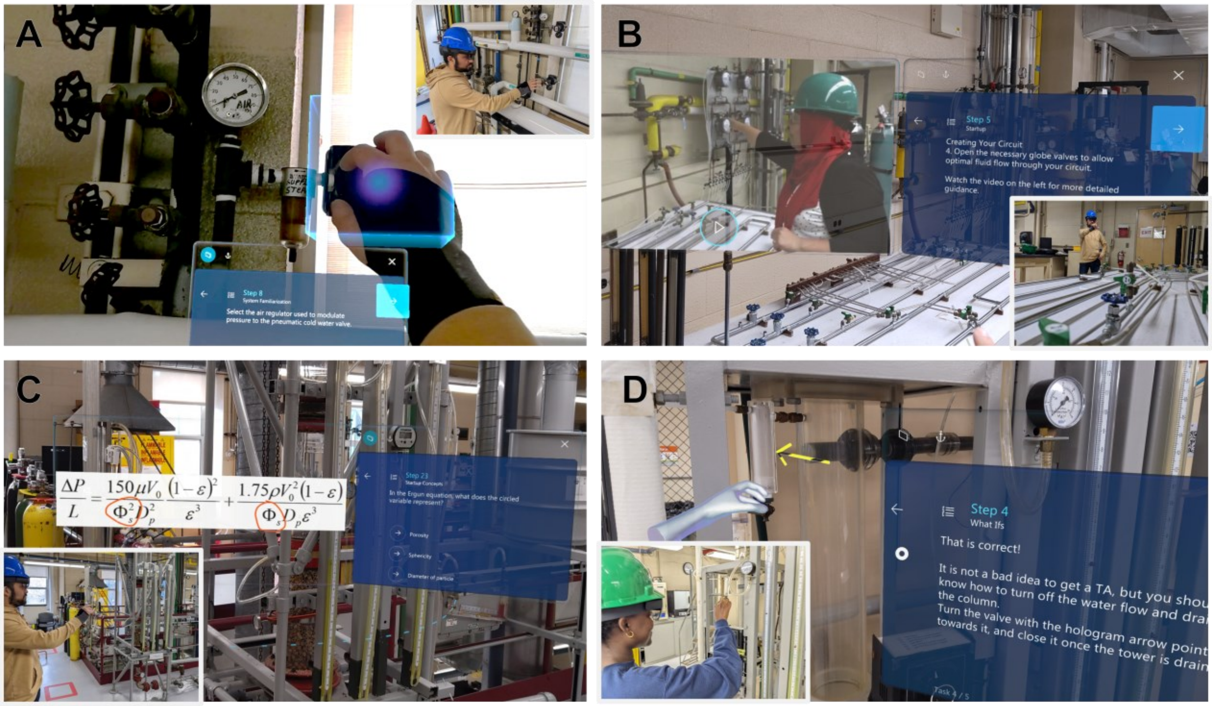

Step 8
System Familiarization
Select the air regulator used to modulate pressure to the pneumatic cold water valve.

Step 5
Startup
Creating Your Circuit
4. Open the necessary globe valves to allow optimal fluid flow through your circuit.
Watch the video on the left for more detailed guidance.

$$\frac{\Delta P}{L}=\frac{150\mu V_0}{\Phi_s^2 D_p^2}\frac{(1-\varepsilon)^2}{\varepsilon^3}+\frac{1.75\rho V_0^2(1-\varepsilon)}{\Phi_s D_p\varepsilon^3}$$

Step 23
Startup Concepts
In the Ergun equation, what does the circled variable represent?
→ Porosity
→ Sphericity
→ Diameter of particle

Step 4
What Ifs
That is correct!
It is not a bad idea to get a TA, but you shou
know how to turn off the water flow and dra
the column.
Turn the valve with the hologram arrow point
towards it, and close it once the tower is drain
Task 4 / 5

Figure 5.6: AR captures and photographs (insets) of the user experience for (A) Familiarization (Identify: Invisible Button) of shell and tube heat exchanger, (B) Procedural (Information: Video) of the fluid flow circuit, (C) Conceptual (Multiple Choice: Picture) of the fluidized bed, and (D) Safety (Information: Hologram) of the packed tower.

5.4.4 ASYNCHRONOUS OUTCOMES/DISCUSSIONS

Pre-lab Guides were explicitly implemented to improve learning by equipping users with the resources to understand the equipment, procedures, theory, and safety of any given unit operation. When executed correctly, students reported that they felt prepared before the start of the lab period and were less intimidated by the experiment setup, as supported in **Table 5.2** where the most effective aspect of AR was “familiarization with lab equipment and components.” Based on discussions with faculty, students, teaching assistants (TAs), and technicians, the following key benefits were identified for the asynchronous tools:

1. Gather.Town and AR Guides should not replace written lab instructions, physical access to the lab, or group-level meetings with instructors but rather augment these course elements to bolster the effectiveness of those course contents and sessions.
2. AR was most effective as a pre-lab tool to reduce startup time and decrease individualized faculty demand at the beginning of lab.
3. The use of short, specific pre-recorded videos in the Guides and posted online by subject-area experts are important to balance written materials.
4. AR should primarily be used to deliver familiarization, procedural, and safety information for time-efficiency and user interactivity with course content. Advanced application may be expanded to cover conceptual content secondarily.

Unfortunately, AR Guide programs were not constructed with equal rigor across the nine unit operations. While some emphasized familiarization and run-time procedures, others delved into underlying and working theory with videos and simulations. Polished Guides on complicated unit operations offered the most benefit to users especially programs whose prompts required the user to not only guess but also think about their outcome. A variety of informational, multiple choice, and identify-type questions aimed to ensure students' interaction with the system and reinforce concepts.

5.4.5 STUDENT RESPONSES

To assess the effectiveness of the new pilot technology implementations, student surveys were conducted after the second year offering of CHE4402 course. These results represent mean experiences over the semester, and it should be noted that substantial standard deviations were recorded, likely due to varying degree of program detail for each UO experiment and the technological delivery challenges discussed later.

Students evaluated their experiences with the AR technology in the UO lab in their responses to the online end-of-term survey. When reflecting on the various elements of the AR Guides, students were asked to rank the effectiveness of each, where higher scores correspond to beneficial aspects of the programs. Results shown in **Table 5.1** highlight that participants identified the pre-recorded video introductions as their top learning aid prior to start the lab period followed by the written lab protocols, access to lab (in person), meeting with faculty/TA, AR experience, and access to lab (remote), respectively. Interestingly, standard deviation varied inversely with average ranking value. Upon closer examination, it appears that this trend aligns with how similar types of information are presented across the set of lab experiments. Concrete elements that are straightforward and inherently helpful such as instructor demonstrations are ranked higher, while those subject to variability like amounts of underlying theory between experiments are ranked lower. Tools that are extremely helpful in some instances may not be as crucial in others. Responses cover the term in its entirety, rather than a single experiment, which further accounts for the wider distributions.

Table 5.1: Students rank the effectiveness of each resource in preparation for starting the lab period.

	AVG	**STDEV**
Pre-recorded video introductions	4.52	0.66
Written lab protocols	4.29	0.88
Access to lab (in person)	3.90	0.97
Meeting with faculty/TA	3.33	1.08
Augmented reality experience	2.95	1.25
Access to lab (remote cameras)	2.26	1.21

A portion of students completed the two UO courses (CHE4401 Unit Operations I/CHE4402 Unit Operations II), of which the AR was only implemented in CHE4401, and their specific insight is captured in the survey responses shown in **Table 5.2**. These students were once again asked to rank their experiences with AR but this time specifically concerning how the in-lab experience compared to those labs that lacked the AR Guide training. The most beneficial outcomes for AR were observed in 1) familiarization with lab equipment and components, and 2) preparing the prelab report. To a lesser extent, students identified in decreasing effectiveness, 3) reducing time to startup, 4) reducing time with faculty/TA during lab, and 5) understanding key concepts/theory for the UO. It is worth noting that experiences varied substantially, and, in many instances, there was a bimodal distribution, indicating that students either found the tool very useful or not useful at all.

Table 5.2: Students rank the effectiveness of the AR compared to labs without the AR component (e.g. CHE4402).

	AVG	**STDEV**
Familiarization with lab equipment and components	3.43	1.47
Preparing the pre-laboratory report	3.05	1.21
Reducing the time to startup/start collecting data	2.76	1.23
Reducing time with faculty/TA during lab	2.71	1.39
Understanding key concepts/theory for the UO	2.62	1.17

Overall, students' experience with the AR was generally positive as outlined in Table 5.3. Survey participants were asked to rate the holistic aspects of the AR Guides on a whole number scale from 1 to 5 with higher numbers corresponding to agreement with the prompt. The top response was that it was fun to use. After that, high ratings were given for clarity of graphics/videos/audio and active engagement with the program. Low ratings were given for the time for familiarization and ease of use, attributed to the glitches discussed earlier.

Table 5.3: Students rate their experience for the operation of the AR program (not the sign-in portion).

	AVG	**STDEV**
Fun to use	3.71	1.03
Clarity of graphics/videos/audio	3.52	1.14
Active engagement with the program	3.48	1.18
Time for familiarization	2.90	1.27
Ease of use	2.52	0.91

In written survey responses, two recurring rationales become evident. First, students identified other platforms (e.g. online quizzes or reports) to be better for evaluating conceptual questions. Secondly, the overwhelming number of responses identified a substantial amount of glitches either during initial program startup or operation. In the optional written responses, 3 of 7 identified major glitching problems, but in their same response they also wrote, the technology was a “really useful tool;” “AR is great and helps me familiarize myself with the physical set up prior to lab;” and “it is a great idea that, when working, is extremely helpful in understanding the lab.” The specific glitches in order of prevalence were: a) slow sign-in processes (5-20 minutes) were initially experienced due to licensing difficulties, b) poor internet connectivity due to campus network security, c) misaligned anchors/holographic objects when using different HL devices, d) blurry graphics due to poor re-calibration when switching users. Anecdotally, the cameras were primarily used after the lab period (e.g. if they missed something in a schematic) or during the lab period (e.g. if one student was remote).

5.5 CONCLUSION

Although AR was initially incorporated into the UO lab in response to the COVID-19 pandemic, successive iterations on the technology and techniques generated pedagogical insight as more deliberate systematic course design was considered. AR maximized in-lab time for large, resource-intensive laboratory courses by minimizing startup and faculty time. Guides served as a technical aid for preparing pre-lab reports and offered independent equipment familiarization and procedural overview prior to lab periods. AR proved less effective at delivering conceptual content than conventional instruction, as mixed reality added unnecessary features to already complicated material. Synchronous remote access was also identified to perform best when the remote users were in control, namely through a web interface with integrated PTZ camera controls; the use of live streaming devices (HL2) proved challenging for the lab student and chaotic for the remote student for prolonged periods of time.

Deliberate mixed reality course design will be needed to leverage the potential for student engagement, procedural training, and conceptual content delivery. The successful use and integration of holograms, picture/video content, and interactive mixed reality actions were demonstrated in this work; future work must take it beyond this scope to challenge the students to think critically in mixed reality space by incorporating simulations, visualization beyond the macroscopic hardware, and assessment during the program. Ultimately, the potential for mixed reality in the laboratory environment is just beginning to be realized.

Acknowledgements: The researchers would like to acknowledge funding by the Department of Energy RAPID award DE-EE0007888-3.2.6 and National Science Foundation CBET 1944619. They also acknowledge the course delivery support from fellow faculty (David DiBiasio, Walter Zurawsky), laboratory technicians (Tom Partington, Douglas White) and TAs (Caroline Rauber).

REFERENCES

1 T. Prasomsri, W. Jiao, S. Z. Weng and J. Garcia Martinez, *Chem. Commun.*, 2015, **51**, 8900–8911.

2 I. Z. Association, *Database Zeolite Struct.*, 2021.

3 T. F. Degnan, G. K. Chitnis and P. H. Schipper, *Microporous Mesoporous Mater.*, 2000, **35**–**36**, 245–252.

4 E. M. Flanigen, in *Studies in Surface Science and Catalysis*, 1991, vol. 58, pp. 13–34.

5 X. Zhang, D. Liu, D. Xu, S. Asahina, K. A. Cychosz, K. V. Agrawal, Y. Al Wahedi, A. Bhan, S. Al Hashimi, O. Terasaki, M. Thommes and M. Tsapatsis, *Science (80-.).*, 2012, **336**, 1684–1687.

6 I. Díaz, E. Kokkoli, O. Terasaki and M. Tsapatsis, *Chem. Mater.*, 2004, **16**, 5226–5232.

7 L. C. Boudreau, J. A. Kuck and M. Tsapatsis, *J. Memb. Sci.*, 1999, **152**, 41–59.

8 T. M. Davis, T. O. Drews, H. Ramanan, C. He, J. Dong, H. Schnablegger, M. A. Katsoulakis, E. Kokkoli, A. V. Mccormick, R. L. Penn and M. Tsapatsis, *Nat. Mater.*, 2006, **5**, 400–408.

9 M. E. Davis, *Ind. Eng. Chem. Res.*, 1991, **30**, 1675–1683.

10 R. F. Lobo, S. I. Zones and M. E. Davis, *J. Incl. Phenom. Mol. Recognit. Chem.*, 1995, **21**, 47–78.

11 M. E. Davis, *Nature*, 2002, **417**, 813–821.

12 G. Feng, P. Cheng, W. Yan, M. Borona, X. Li, J. H. Su, J. Wang, Y. Li, A. Corma, R. Xu and J. Yu, *Science (80-.).*, 2016, **351**, 1188–1191.

13 A. Corma, *Chem. Rev.*, 1997, **97**, 2373–2419.

14 A. Corma, *J. Catal.*, 2003, **216**, 298–312.

15 M. Moliner, Y. Román-Leshkov and A. Corma, *Acc. Chem. Res.*, 2019, **52**, 2971–2980.

16 V. Nikolakis, E. Kokkoli, M. Tirrell, M. Tsapatsis and D. G. Vlachos, *Chem. Mater.*, 2000, **12**, 845–853.

17 J. D. Rimer, J. M. Fedeyko, D. G. Vlachos and R. F. Lobo, *Chem. - A Eur. J.*, 2006, **12**, 2926–2934.

18 R. W. Thompson, *Synthesis (Stuttg).*, 2007, **1**, 1–33.

19 R. W. Thompson and A. Dyer, *Zeolites*, 1985, **5**, 202–210.

20 M. Kumar, H. Luo, Y. Román-Leshkov and J. D. Rimer, *J. Am. Chem. Soc.*, 2015, **137**, 13007–13017.

21 J. D. Rimer, *Nat. Catal.*, 2018, **1**, 488–489.

22 R. Li, A. Chawla, N. Linares, J. G. Sutjianto, K. W. Chapman, J. G. Martínez and J. D. Rimer, *Ind. Eng. Chem. Res.*, 2018, **57**, 8460–8471.

23 S. Kumar, Z. Wang, R. Lee Perm and M. Tsapatsis, *J. Am. Chem. Soc.*, 2008, **130**, 17284–17286.

24 J. Ju, C. Zeng, L. Zhang and N. Xu, *Chem. Eng. J.*, 2006, **116**, 115–121.

25 E. N. Coker, A. G. Dixon, R. W. Thompson and A. Sacco, *Microporous Mater.*, 1995, **3**, 637–646.

26 C. T. Chen, K. Iyoki, H. Yamada, S. Sukenaga, M. Ando, H. Shibata, K. Ohara, T. Wakihara and T. Okubo, *J. Phys. Chem. C*, 2019, **123**, 20304–20313.

27 S. Askari, S. Miar Alipour, R. Halladj and M. H. Davood Abadi Farahani, *J. Porous Mater.*, 2013, **20**, 285–302.

28 L. C. Porcher F, Dusausoy Y, Souhassou M, *Mineral. Mag. 64*, 2000, **64**, 1–8.

29 M. Kumar, M. K. Choudhary and J. D. Rimer, *Nat. Commun.*, , DOI:10.1038/s41467-018-04296-4.

30 W. Qin, R. Jain, F. C. Robles Hernández and J. D. Rimer, *Chem. - A Eur. J.*, 2019, **25**, 5893–5898.

31 A. Moreno and M. E. Mendoza, *Crystallization in Gels*, Elsevier B.V., 2015, vol. 2.

32 M. Kumar, R. Li and J. D. Rimer, *Chem. Mater.*, 2016, **28**, 1714–1727.

33 S. Alfaro, C. Rodríguez, M. A. Valenzuela and P. Bosch, *Mater. Lett.*, 2007, **61**, 4655–4658.

34 A. A. Chernov, *Modern Crystallogrpahy III*, Springer-Verlag, Berlin, Heidelberg, New York, Tokyo, 1984, vol. 7.

35 D. Rossi, R. Jamshidi, N. Saffari, S. Kuhn, A. Gavriilidis and L. Mazzei, *Cryst. Growth Des.*, 2015, **15**, 5519–5529.

36 N. Yazdanpanah and Z. K. Nagy, Eds., Royal Society of Chemistry, 2020.

37 Z. Liu, T. Wakihara, D. Nishioka, K. Oshima, T. Takewaki and T. Okubo, *Chem. Commun.*, 2014, **50**, 2526–2528.

38 J. Zhang, K. Wang, A. R. Teixeira, K. F. Jensen and G. Luo, *Annu. Rev. Chem. Biomol.*

Eng., 2017, **8**, 285–305.

39 Z. Liu, K. Okabe, C. Anand, Y. Yonezawa, J. Zhu, H. Yamada, A. Endo, Y. Yanaba, T. Yoshikawa, K. Ohara, T. Okubo and T. Wakihara, *Proc. Natl. Acad. Sci.*, 2016, **113**, 14267–14271.

40 L. Yu, Y. Pan, C. Wang and L. Zhang, *Chem. Eng. J.*, 2013, **219**, 78–85.

41 A. Gualtieri, P. Norby, G. Artioli and J. Hanson, *Phys. Chem. Miner.*, 1997, **24**, 191–199.

42 R. W. Thompson, *Zeolites*, 1992, **12**, 680–684.

43 C. J. J. den Ouden and R. W. Thompson, *Ind. Eng. Chem. Res.*, 1992, **31**, 369–373.

44 J. Mullin, *Crystallization*, Elsevier Science, 2001.

45 S. Karthika, T. K. Radhakrishnan and P. Kalaichelvi, *Cryst. Growth Des.*, 2016, **16**, 6663–6681.

46 R. Gaillac, S. Chibani and F. X. Coudert, *Chem. Mater.*, 2020, **32**, 2653–2663.

47 P. Cubillas and M. W. Anderson, *Synthesis Mechanism: Crystal Growth and Nucleation*, 2010, vol. 1.

48 J. Coronas, *Chem. Eng. J.*, 2010, **156**, 236–242.

49 J. Grand, H. Awala and S. Mintova, *CrystEngComm*, 2016, **18**, 650–664.

50 T. Brar, P. France and P. G. Smirniotis, 2001, 1133–1139.

51 L. Gora, *Zeolites*, 1997, **18**, 132–141.

52 J. Bronić and B. Subotić, *Microporous Mater.*, 1995, **4**, 239–242.

53 J. Warzywoda, R. D. Edelman and R. W. Thompson, *Zeolites*, 1991, **11**, 318–324.

54 W. Fan, M. A. Snyder, S. Kumar, P. S. Lee, W. C. Yoo, A. V. McCormick, R. Lee Penn, A. Stein and M. Tsapatsis, *Nat. Mater.*, 2008, **7**, 984–991.

55 M. Gharibeh, G. Tompsett and W. C. Conner, *AIChE Annu. Meet. Conf. Proc.*, 2008, 12506–12520.

56 S. L. Burkett and M. E. Davis, *Chem. Mater.*, 1995, **7**, 920–928.

57 A. I. Lupulescu and J. D. Rimer, *Science (80-.).*, 2014, **344**, 729–732.

58 P. S. Lee, X. Zhang, J. A. Stoeger, A. Malek, W. Fan, S. Kumar, W. C. Yoo, S. Al Hashimi, R. L. Penn, A. Stein and M. Tsapatsis, *J. Am. Chem. Soc.*, 2011, **133**, 493–502.

59 A. Arafat, J. C. Jansen, A. R. Ebaid and H. van Bekkum, *Zeolites*, 1993, **13**, 162–165.

60 L. Bonaccorsi and E. Proverbio, *Microporous Mesoporous Mater.*, 2008, **112**, 481–493.

61 Z. Liu, J. Zhu, T. Wakihara and T. Okubo, *Inorg. Chem. Front.*, 2019, **6**, 14–31.

62 S. Yang, A. Navrotsky and B. L. Phillips, *Microporous Mesoporous Mater.*, 2001, **46**, 137–151.

63 A. Ghazal, J. P. Lafleur, K. Mortensen, J. P. Kutter, L. Arleth and G. V. Jensen, *Lab Chip*, 2016, **16**, 4263–4295.

64 D. M. Roberge, L. Ducry, N. Bieler, P. Cretton and B. Zimmermann, *Chem. Eng. Technol.*, 2005, **28**, 318–323.

65 C. Sudha and K. Srinivasan, *CrystEngComm*, 2013, **15**, 1914–1921.

66 E. P. K. Ottens, A. H. Janse and E. J. De Jong, *J. Cryst. Growth*, 1972, **13**–**14**, 500–505.

67 S. L. Poe, M. A. Cummings, M. P. Haaf and D. T. McQuade, *Angew. Chemie*, 2006, **118**, 1574–1578.

68 M. Movsisyan, E. I. P. Delbeke, J. K. E. T. Berton, C. Battilocchio, S. V. Ley and C. V. Stevens, *Chem. Soc. Rev.*, 2016, **45**, 4892–4928.

69 B. Gutmann, D. Cantillo and C. O. Kappe, *Angew. Chemie - Int. Ed.*, 2015, **54**, 6688–6728.

70 R. L. Hartman, *Org. Process Res. Dev.*, 2012, **16**, 870–887.

71 C. N. Baroud, F. Gallaire and R. Dangla, *Lab Chip*, 2010, **10**, 2032–2045.

72 S. R. L. Gobert, S. Kuhn, L. Braeken and L. C. J. Thomassen, *Org. Process Res. Dev.*, 2017, **21**, 531–542.

73 M. Lake, C. Narciso, K. Cowdrick, T. Storey, S. Zhang, J. Zartman and D. Hoelzle, *Protoc. Exch.*, , DOI:10.1038/protex.2015.069.

74 M. Schmalenberg, L. K. Weick and N. Kockmann, *J. Flow Chem.*, 2021, **11**, 303–319.

75 M. Jiang, X. Zhu, M. C. Molaro, M. L. Rasche, H. Zhang, K. Chadwick, D. M. Raimondo, K. K. K. Kim, L. Zhou, Z. Zhu, M. H. Wong, D. O'Grady, D. Hebrault, J. Tedesco and R. D. Braatz, *Ind. Eng. Chem. Res.*, 2014, **53**, 5325–5336.

76 M. T. Roberts, A. Mohraz, K. T. Christensen and J. A. Lewis, *Langmuir*, 2007, **23**, 8726–8731.

77 A. Majumder and Z. K. Nagy, *AIChE J.*, 2013, **59**, 4582–4594.

78 D. Kashchiev, *Nucleation*, 2000, 9–16.

79 Z. K. Nagy, E. Aamir and C. D. Rielly, *Cryst. Growth Des.*, 2011, **11**, 2205–2219.

80 B. Szilágyi, *Chem. Eng. Process. - Process Intensif.*, , DOI:10.1016/j.cep.2022.109074.

81 K. H. Heinig, B. Schmidt, M. Strobel and H. Bernas, *Mater. Res. Soc. Symp. - Proc.*, , DOI:10.1557/proc-650-r9.6/o14.6.

82 W. Omar, S. Al-Sayed, A. Sultan and J. Ulrich, *Cryst. Res. Technol.*, 2008, **43**, 22–27.

83 T. Van Westen and R. D. Groot, *Cryst. Growth Des.*, 2018, **18**, 4952–4962.

84 K. V. R. Prasad, R. I. Ristic, D. B. Sheen and J. N. Sherwood, *Int. J. Pharm.*, 2002, **238**, 29–41.

85 S. Höving, B. Oldach and N. Kockmann, *Processes*, , DOI:10.3390/pr10061047.

86 K. Robertson, P. H. Seeberger and K. Gilmore, *React. Chem. Eng.*, 2022, **8**, 77–83.

87 B. Ahn, L. Bosetti and M. Mazzotti, *Cryst. Growth Des.*, 2022, **22**, 74–86.

88 N. A. Mitchell, C. T. Óciardhá and P. J. Frawley, *J. Cryst. Growth*, 2011, **328**, 39–49.

89 S. Kim, C. Wei and S. Kiang, *Org. Process Res. Dev.*, 2003, **7**, 997–1001.

90 and M. F. D. Ryan C. Snyder, Stephan Studener, *AIChE J.*, 2007, **53**, 1510–1517.

91 W. Li, C. Zhao, B. Zou, X. Zhang, J. Yu, X. Zhang and J. Jie, *CrystEngComm*, 2012, **14**, 8124–8127.

92 M. R. A. Bakar, Z. K. Nagy and C. D. Rielly, *Org. Process Res. Dev.*, 2009, **13**, 1343–1356.

93 A. Saleemi, C. Rielly and Z. K. Nagy, *CrystEngComm*, 2012, **14**, 2196–2203.

94 M. O. Besenhard, P. Neugebauer, O. Scheibelhofer and J. G. Khinast, *Cryst. Growth Des.*, 2017, **17**, 6432–6444.

95 M. A. Ardagh, O. A. Abdelrahman and P. J. Dauenhauer, *ACS Catal.*, 2019, **9**, 6929–6937.

96 T. Rosenbaum, L. Tan, M. Dummeldinger, N. Mitchell and J. Engstrom, *Org. Process Res. Dev.*, 2019, **23**, 2666–2677.

97 N. A. Mitchell and P. J. Frawley, *J. Cryst. Growth*, 2010, **312**, 2740–2746.

98 Y. Kim, Y. Kawajiri, R. W. Rousseau and M. A. Grover, *Ind. Eng. Chem. Res.*, 2023, **62**, 2866–2881.

99 M. Á. Ballesteros, J. S. Sánchez, N. Ratkovich, J. C. Cruz and L. H. Reyes, *Educ. Chem. Eng.*, 2021, **35**, 8–21.

100 R. M. Baldwin and B. M. Olds, .

101 A. M. Abu-Khalaf, *Int. J. Eng. Educ.*, 2001, **17**, 593–599.

102 T. L. Carter, S. A. Wilson, S. Azarin, J. Brennan, A. J. Karlsson and C. J. Barr, *ASEE Annu. Conf. Expo. Conf. Proc.*, , DOI:10.18260/1-2--33578.

103 L. Jimenez, J. Font, J. Bonet and X. Farriol, *Chem. Eng. Educ.*, 2002, **36**, 150–154.

104 C. P. Luks, *2021 ASEE Midwest Sect. Conf.*

105 A. Maxson, *2021 ASEE Virtual Annu. Conf. Content Access*.

106 N. Dietrich, K. Kentheswaran, A. Ahmadi, J. Teychene, Y. Bessie, D. Bastoul, K. Loubie, M. Sperandio, L. Barna, E. Paul, C. Cabassud, A. Line and G. He, , DOI:10.1021/acs.jchemed.0c00717.

107 R. Dua, *2021 ASEE Virtual Annu. Conf. Content Access*.

108 A. M. Elkhatat and S. A. Al, *SN Soc. Sci.*, 2021, **1**, 1–16.

109 T. Wiesner and W. Lan, *Res. J. Eng. Educ.*, 2004, **93**, 195–204.

110 J. Glassey and F. D. Magalhães, *Educ. Chem. Eng.*, 2020, **33**, 76–77.

111 T. W. Smith, N. Souto-melgar and E. C. Clausen, *2021 ASEE Midwest Sect. Conf.*

112 J. Martín-Gutiérrez, P. Fabiani, W. Benesova, M. D. Meneses and C. E. Mora, *Comput. Human Behav.*, 2015, **51**, 752–761.

113 S. Solmaz, J. L. D. Alfaro, P. Santos, P. Van Puyvelde and T. Van Gerven, *Educ. Chem. Eng.*, 2021, **35**, 81–93.

114 B. Zhu, M. Feng, H. Lowe, L. Harrison and R. E. Dempski, *J. Chem. Educ.*, 2018, **95**, 1747–1754.

115 C. Kamphuis, E. Barsom, M. Schijven and N. Christoph, *Perspect. Med. Educ.*, 2014, **3**, 300–311.

116 C. Juan, F. Beatrice and J. Cano, *Eighth IEEE Int. Conf. Adv. Learn. Technol.*, 2008, 186–188.

117 R. Layona, R. Layona, B. Yulianto and Y. Tunardi, *Procedia Comput. Sci.*, 2018, **135**, 457–464.

118 S. Dreimane and L. Daniela, *Technol. Knowl. Learn.*, 2021, **26**, 763–788.

119 A. Teixeira, WPI Microsoft Guides/Augmented Reality in Chemical Engineering, https://youtu.be/1YMQcvZISjU.

120 A. Teixeira, WPI CHE Augmented Reality - Remote Assist, https://youtu.be/UUk7AL9s6Ok.

121 B. T. Incropera FP, DeWitt DP, Lavine AS, *Fundamentals of Heat and Mass Transfer*, John Wiley & Sons, Incorporated, 2010.

122 D. (ETH Z. Ochsenbein and M. (ETH Z. Iggland, 2016.

APPENDIX 1

HEAT TRANSFER CALCULATIONS

The following model is used to estimate the heat up time for each reactor from $T_i = 20\ °C$ to $T_\infty = 65\ °C$. The values obtained are used in calculating theoretical τ_{conv}, τ_{cond} and Bi. All Nusselt number correlations were taken from the Incropera textbook for the appropriate geometry and conditions.[121] First, the Biot number was calculated to assess whether the heat transfer gradient existed within the reactor or in the heat transfer medium external do the reactor. For each reactor-heater pair, the Biot number was calculated assuming the external domain was water or air, and the internal domain (reactor wall + sol-gel) approximated a single resistance with properties approximated by those of water.

PHYSICAL PARAMETERS:

$k_{air}(65\ °C) = 0.029\ W\ m^{-1}\ K^{-1}$, $\beta_{air}(65\ °C) = 2.97 \times 10^{-3}\ K^{-1}$, $v_{air}(65\ °C) = \mu/\rho = 19.5 \times 10^{-6}\ m^2\ s^{-1}$, $\alpha_{air}(65\ °C) = 27 \times 10^{-6}\ m^2/s$

$k_{water}(65\ °C) = 0.655\ W\ m^{-1}\ K^{-1}$

REACTOR PARAMETERS:

For the batch reactor, the characteristic length is taken to be the radius of the polypropylene bottle, while the tubing outside diameter was taken for the microbatch.

$L_{batch} = 0.1\ m$

$L_\mu = 0.001\ m$

FREE CONVECTION IN AIR: BATCH

$$\overline{Nu}_D = \frac{\bar{h}D}{k} = CRa_D^n$$

$$Ra_D = \frac{g\beta(T_s - T_\infty)D^3}{v\alpha} = \frac{(9.81\ m\ s^{-2})(2.97\times10^{-3}\ K^{-1})(65-20\ K)(0.1\ m)^3}{(19.5\times10^{-6}\ m^2 s^{-1})(27\times10^{-6}\ m^2\ s^{-1})} = 2.5 \times 10^6$$

Incropera Table 9.1: $C = 0.480,\ n = 0.250$

$$\bar{h} = \frac{k}{D}\ CRa_D^n = \frac{0.029\ W\ m^{-1}K^{-1}}{0.1\ m}(0.480)(2.5 \times 10^6)^{0.250} = 5.53\ W\ m^{-2}\ K^{-1}$$

$$Bi = \frac{\bar{h}_{air}\ D/2}{k_{water}} = \frac{(5.53\ W\ m^{-2}K^{-1})(0.05\ m)}{(0.655\ W\ m^{-1}\ K^{-1})} = 0.42$$

FORCED CONVECTION IN AIR: BATCH

Cylinder in cross flow (Incropera eqn. 7.52)[121]:

$$\overline{Nu}_D = \frac{\bar{h}D}{k} = CRe_D^m Pr^{1/3}$$

$$Re_D = \frac{\rho VD}{\mu} = \frac{VD}{\nu}$$

For air with $V{\sim}1\ m\ s^{-1}$

$$Re_D = \frac{(1\ m\ s^{-1})(0.1\ m)}{19.5{\times}10^{-6}\ m^2s^{-1}} = 5130$$

$$Pr = \frac{\nu}{\alpha} = \frac{19.5{\times}10^{-6}\ m^2\ s^{-1}}{27{\times}10^{-6}\ m^2\ s^{-1}} = 0.72$$

$$\overline{Nu}_D = C\ Re_D^m Pr^{1/3} = (0.193)(5130)^{(0.618)}(0.72)^{1/3} = 34.0$$

$$\bar{h} = \frac{k}{D}\overline{Nu}_D = 9.9\ W\ m^{-2}\ K^{-1}$$

$$Bi = \frac{\bar{h}_{air}D/2}{k_{water}} = \frac{(9.9\ W\ m^{-2}K^{-1})(0.1\ m)/2}{(0.655\ W\ m^{-1}\ K^{-1})} = 0.75$$

FORCED CONVECTION IN WATER: BATCH

$$Re_D = \frac{(1\ m\ s^{-1})(0.001\ m)}{4.4{\times}10^{-7}\ m^2s^{-1}} = 2.27 \times 10^3$$

$$Pr = \frac{\nu}{\alpha} = \frac{(4.4{\times}10^{-7}m^2\ s^{-1})}{(1.59{\times}10^{-7}m^2\ s^{-1})} = 2.77$$

$$\overline{Nu}_D = C\ Re_D^m Pr^{1/3} = (0.027)(2.27 \times 10^5)^{(0.805)}(2.77)^{1/3} = 778$$

$$\bar{h} = \frac{k}{D}\overline{Nu}_D = 5.1 \times 10^3\ W\ m^{-2}\ K^{-1}$$

$$Bi = \frac{\bar{h}_{air}D/2}{k_{water}} = \frac{(5.1{\times}10^3\ W\ m^{-2}K^{-1})(0.1\ m)/2}{(0.655\ W\ m^{-1}\ K^{-1})} = 389$$

FORCED CONVECTION IN AIR: MICRO-BATCH

$$\overline{Nu}_D = \frac{\bar{h}D}{k} = CRe_D^m Pr^{1/3}$$

$$Re_D = \frac{\rho VD}{\mu} = \frac{VD}{\nu}$$

For air with $V \sim 1\ m\ s^{-1}$

$$Re_D = \frac{(1\ m\ s^{-1})(0.001\ m)}{19.5\times10^{-6}\ m^2 s^{-1}} = 51.3$$

$$Pr = \frac{\nu}{\alpha} = \frac{19.5\times10^{-6}\ m^2\ s^{-1}}{27\times10^{-6}\ m^2\ s^{-1}} = 0.72$$

$$\overline{Nu}_D = C\ Re_D^m Pr^{1/3} = (0.193)(51.3)^{(0.618)}(0.72)^{1/3} = 3.84$$

$$\bar{h} = \frac{k}{D}\overline{Nu}_D = 111\ W\ m^{-2}\ K^{-1}$$

$$Bi = \frac{\bar{h}_{air}D/2}{k_{water}} = \frac{(111\ W\ m^{-2}K^{-1})(0.001\ m)/2}{(0.655\ W\ m^{-1}\ K^{-1})} = 0.085$$

FORCED CONVECTION IN WATER: MICRO-BATCH

$$Re_D = \frac{(1\ m\ s^{-1})(0.1\ m)}{(4.4\times10^{-7}\ m^2 s^{-1})} = 2.27\times10^3$$

$$Pr = \frac{\nu}{\alpha} = \frac{(4.4\times10^{-7} m^2\ s^{-1})}{(1.59\times10^{-7} m^2\ s^{-1})} = 2.77$$

$$\overline{Nu}_D = C\ Re_D^m Pr^{1/3} = (0.683)(2.27\times10^3)^{(0.466)}(2.77)^{1/3} = 35.1$$

$$\bar{h} = \frac{k}{D}\overline{Nu}_D = 2.3\times10^4\ W\ m^{-2}\ K^{-1}$$

$$Bi = \frac{\bar{h}_{air}D/2}{k_{water}} = \frac{(35.1\ W\ m^{-2}K^{-1})(0.001\ m)/2}{(0.655\ W\ m^{-1}\ K^{-1})} = 17.6$$

The characteristic times for the two constitutive heat transfer steps—internal heat conduction through the crystallizer and external convective heating from a hot fluid—were both individually estimated. The including heating modes range in heat transfer control between externally slow heating causing the crystallizer to be effectively isothermal, albeit slow heating ($Bi < 1$) to the opposite case, where internal heating is slow relative to the fast external heating ($Bi > 1$), causing internal heat transfer gradients. The following table summarizes the scenarios examined here.

$\tau_{cond} = \frac{L^2}{\alpha_w}$, $\tau_{conv} = \frac{L\rho c_p}{h}$

Where L is the characteristic length for the crystallizer (diameter) and α_w is the thermal diffusivity of the internal domain, in this case approximated as water. The external convection time constant (τ_{conv}) was estimated using properties of the respective heat transfer fluid (air or water) and was calculated as $\tau_{conv} = Bi \,/\, \tau_{cond}$.

The heat transfer extends between externally slow heating, causing the crystallizer to be effectively isothermal, albeit slow heating ($Bi < 1$) to the opposite case, where internal heating is slow relative to the fast external heating ($Bi > 1$), causing internal heat transfer gradients. The following table summarizes the scenarios examined in this work.

Table A1.1: Heat transfer time characterization for various reactor configurations, highlighting the appearance of internal gradients as Biot number increases.

Case	**h ($Wm^{-2}K^{-1}$)**	**Bi**	**τ_{cond} (s)**	**τ_{conv} (s)**	**Note**
Batch Oven	5.53	0.42	6.3×10^4	1.5×10^5	Slow heating with thermal gradients in both phases
Batch Convection Oven	9.9	0.75	6.3×10^4	8.4×10^4	Faster heating, with internal gradients
Batch Water Bath	5.1×10^3	389	6.3×10^4	1.6×10^2	Fast heating with substantial internal gradients
Microbatch Convection Oven	111	0.085	6.3	7.4×10^1	Very fast heating, gradients in both phases
Microbatch Water Bath	2.3×10^4	17.6	6.3	3.6×10^{-1}	Extremely fast heating with internal gradients

HEAT TRANSFER FITTING

The next step is to determine the characteristic time for heat up. This is done by first determining the form of the heat transfer expression, then performing the respective fits. In this case, the Biot number ranges from 10^{-1} – 10^2, meaning both internal and external heat transfer modes must be considered. In the case of lumped capacitance ($Bi < 1$), the transient system can approximately be modeled as:

$$\frac{T(t)-T_\infty}{T_i-T_\infty} = \exp[-Bi \times Fo] = \exp\left[\frac{t}{\tau}\right]$$

$$\tau = \frac{\rho V c}{h A_s}$$

$$Fo = \frac{\alpha t}{L^2}$$

The resulting equation is fit to the experimental curves for the batch oven and microbatch convection oven ($Bi \ll 1$). In the other extreme ($Bi \gg 1$), external convection is fast, and the internal transient profile must be resolved. The exact solution is an infinite expansion solved with a Bessel function. The first term approximation for the infinite cylinder is (Incropera eq 5.52)[121]:

$$\frac{T(t)-T_\infty}{T_i-T_\infty} = C_1 \exp[-\zeta_1^2 Fo]\, J_0\left(\zeta_1 \frac{r}{R}\right) = C_1 J_0\left(\zeta_1 \frac{r}{R}\right) \exp\left[-\frac{t}{\tau}\right]$$

$$\tau = \frac{L^2}{\zeta_1^2 \alpha}$$

Note, an exponential fit can again be performed to fit the time constant, τ. As the subsequent analysis requires only an approximation of the time constants (not pre-exponential) to perform the nondimensional analysis, a single expression is fit for all reactor configurations:

$$\frac{\bar{T}(t)-T_\infty}{T_i-T_\infty} = C \exp\left[-\frac{t}{\tau_{heat}}\right]$$

EVIDENCE OF HEAT TRANSFER LIMITATIONS

Batch crystallizations were performed under sensitive conditions (i.e. near t_{50}) to demonstrate the impact on external heating modes. Oven heating was slower, yielding lower crystallinity and a substantial scatter in date (+/- 20%) across 20 identical trials. The identical experiment performed with a water bath for heating was fully crystalline with little deviation.

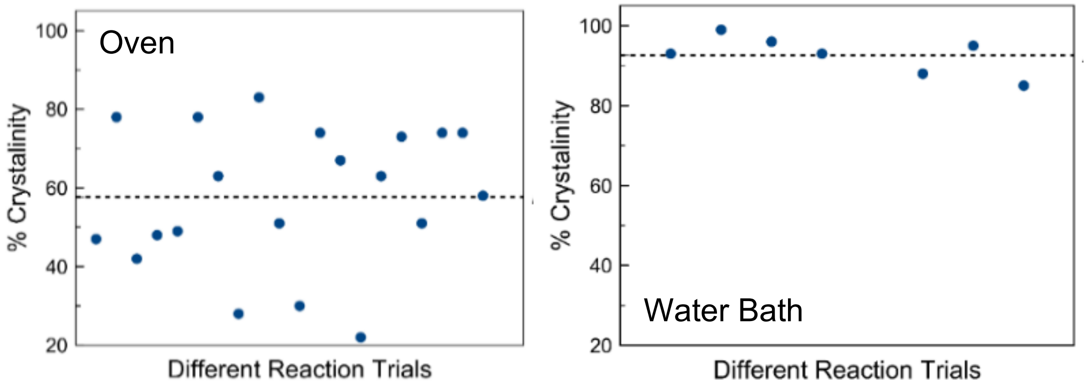

Figure A1.1: Heat Transfer Limitation in Batch. LTA crystallinity in a 25 mL polypropylene bottle after 12 hours of aging at 20 °C and 60 min at 65 °C. Oven trials (left) show slower rates and higher scatter, while water bath (right) are fast and reproducible. 1 SiO_2 : 0.18 Al_2O_3 : 8.6 NaOH : 150 H_2O

XRD PATTERNS

XRD patterns for all reactor configurations at each time point.

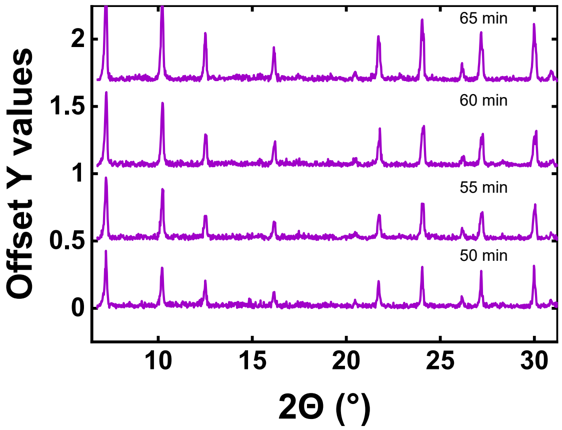

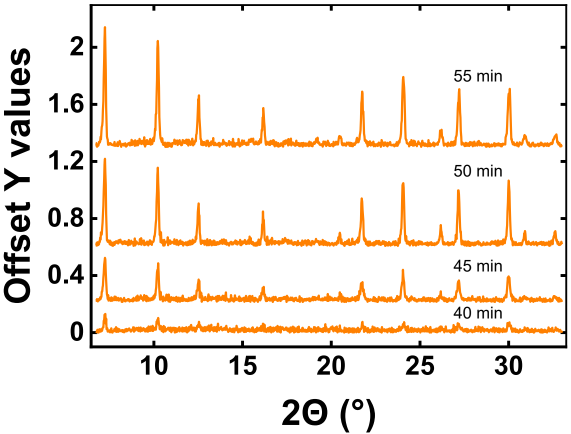

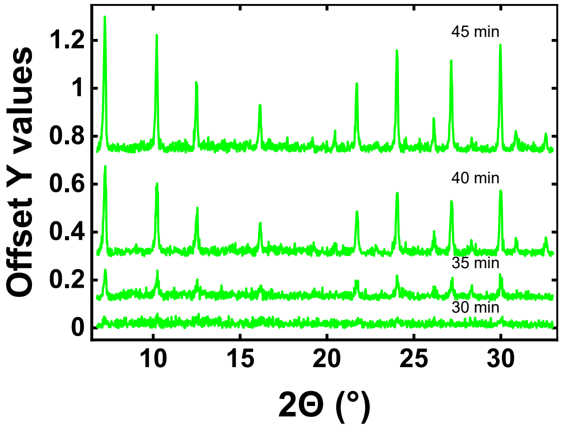

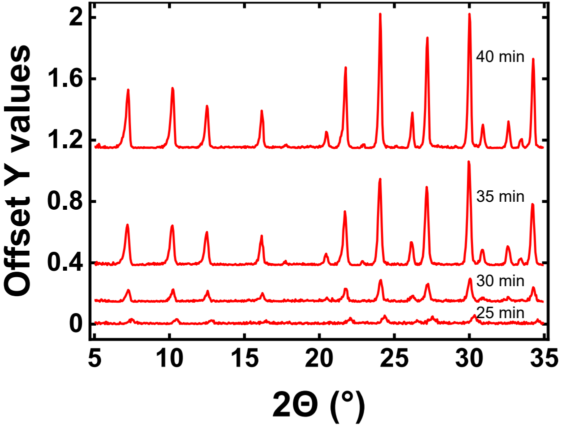

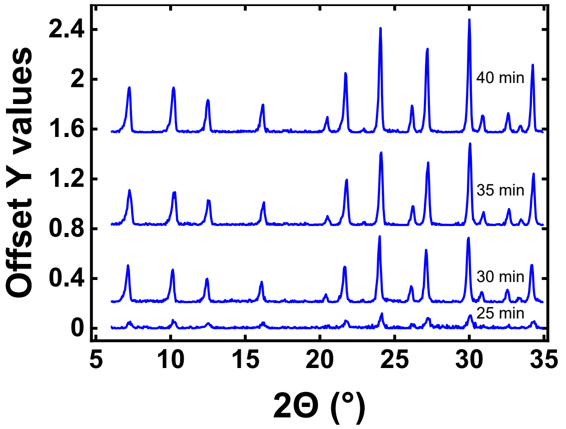

Figure A1.2: XRD patterns for all reactor configurations and times. Top row: batch oven (left), batch convection oven (right). Middle row: batch water bath (left), microbatch convection oven (right). Bottom row: microbatch bath.

N_2 ISOTHERMS

Nitrogen isotherms were obtained as described in the methods of the manuscript. Characteristic isotherms are shown here for select samples.

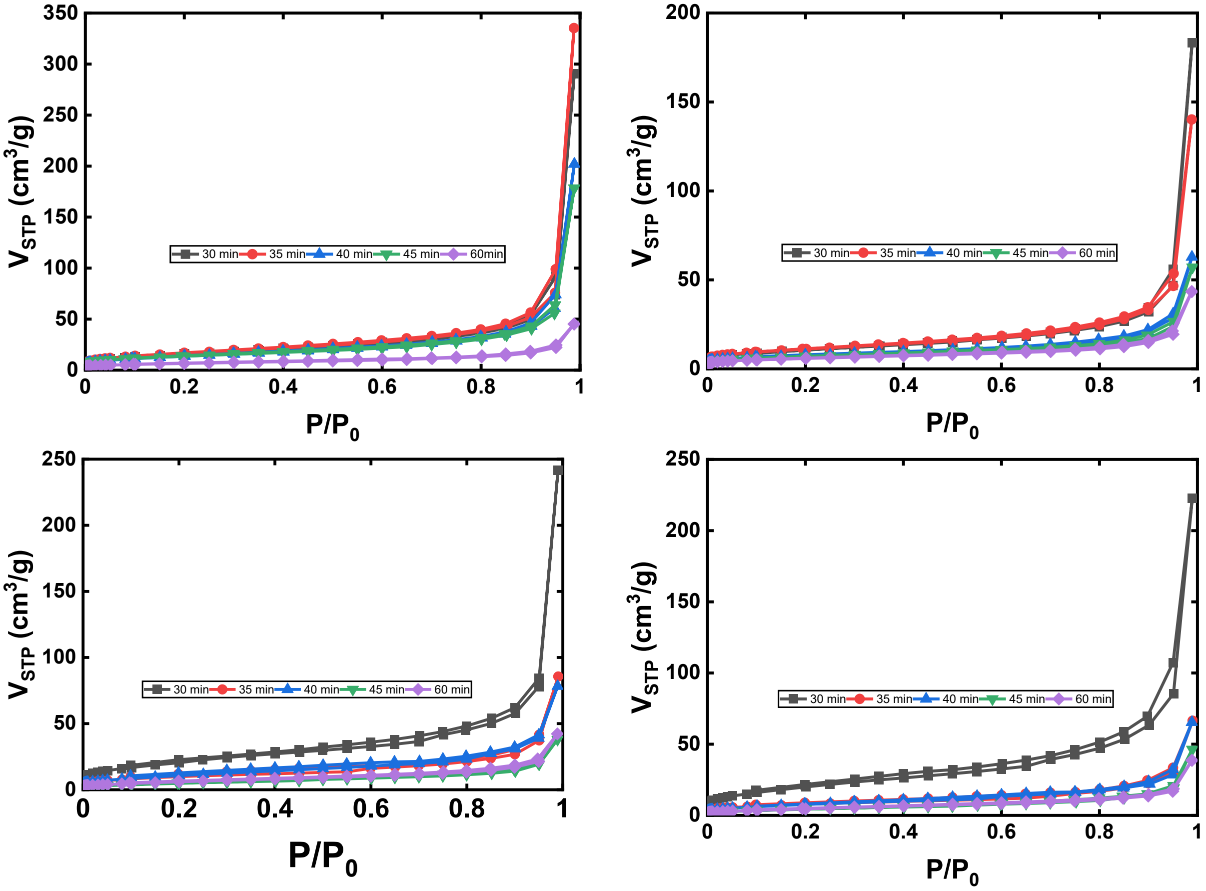

Figure A1.3: Nitrogen isotherms for batch convection oven (top left), batch bath (top right), microbatch convection oven (bottom left), and microbatch bath (bottom right).

AVRAMI FITS

Linearization of the crystallinity versus time plots was achieved with the Avrami plot approach. The resulting fitting parameters (k, n) are tabulated in Table A1.2.

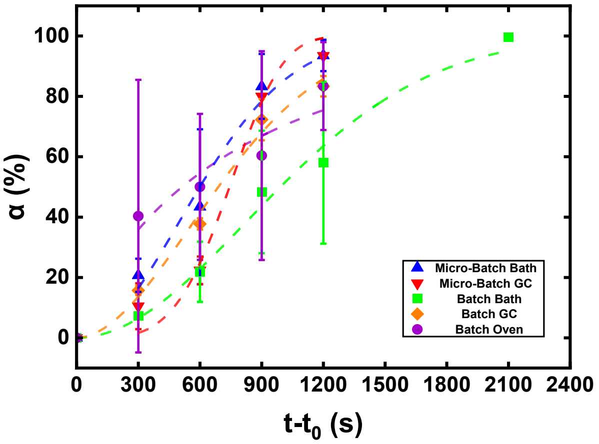

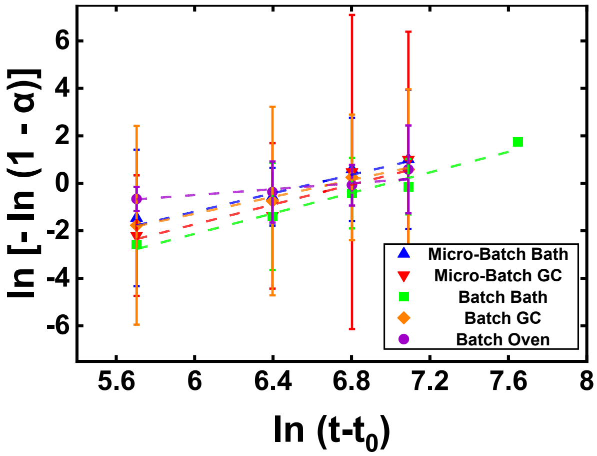

Figure A1.4A Avrami kinetics show rate enhancement via micro-crystallization
Figure A1.4B Linearized Avrami data simplifies parameter estimates

Table A1.2: Experimental times and Avrami kinetic parameters

Reactor	***t_0* (s)**	***t_{50}* (s)**	***k* (s^{-1})**	***n***
Batch Oven	2700	3210	3.88×10^{-3}	0.831
Batch Convection Oven	2100	2780	3.52×10^{-6}	1.87
Batch Bath	1500	2680	9.47×10^{-7}	1.96
Microbatch Convection Oven	1200	1950	9.44×10^{-13}	4.13
Microbatch Bath	1200	1810	2.59×10^{-6}	1.95

MICRODROPLET GENERATOR STATISTICS

Microdroplets were photographed and 371 particles were individually measured. The resulting histogram is shown below with tabulated analysis data to demonstrate monodispersity of the microbatch droplets.

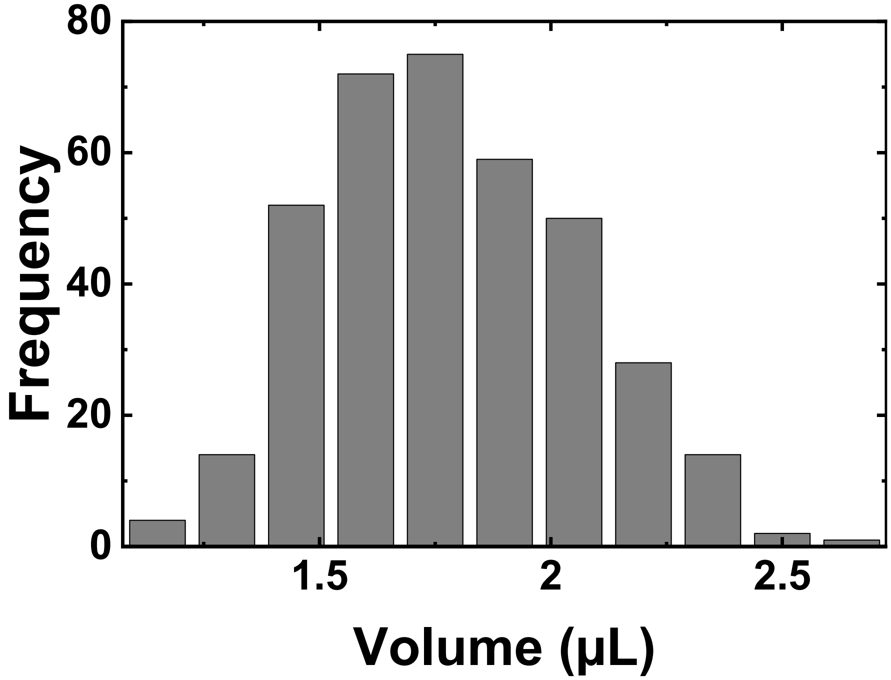

Figure A1.5 Histogram of microdroplet volumes.

Table A1.3: Microdroplet statistics

Descriptive Statistics (μL)	
Mean	1.71
Median	1.69
Mode	1.81
Standard Deviation	0.275
Kurtosis	-0.365
Skewness	0.248
Range	1.53
Minimum	1.03
Maximum	2.55
Count	371
Confidence Level (95.0%)	0.0281

APPENDIX 2

CRYSTALLIZATION ANALYSIS TOOLBOX (CAT)

The Crystallization Analysis Toolbox is a population balance equation solver coded into a MATLAB graphical user interface designed by Dave Ochsenbein and Martin Iggland.[122] All inputs are defined in units of kilograms, microns, and degrees Celsius. Outputs for the solver include 3D time-resolved particle size distributions for number density and volume distribution, each normalized to the integrated value of the input particle size distribution; a series of time-resolved plots of the zeroth and third moments (μ_0 and μ_3) and the average particle size; a set of plots depicting time-resolved concentration, supersaturation, temperature, and antisolvent profiles; a phase diagram showing the trajectory of the crystallization; and a plot of the integrated error of the solver. A high resolution solving method is employed to solve the PBE based on user defined inputs listed below:

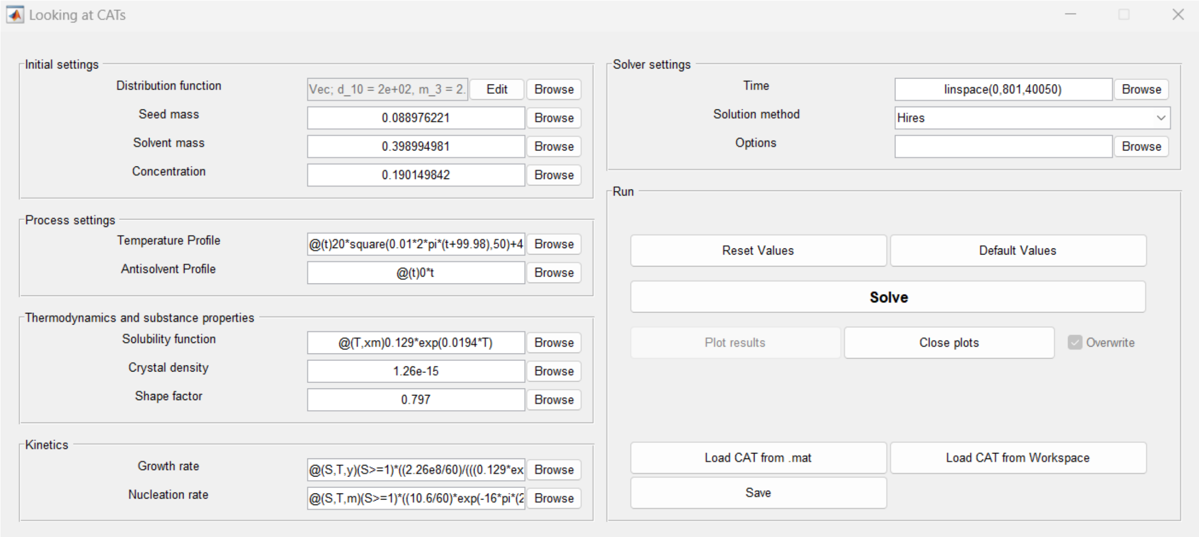

Initial settings
Distribution function: Vec; d_10 = 2e+02, m_3 = 2.
Seed mass: 0.088976221
Solvent mass: 0.398994981
Concentration: 0.190149842

Process settings
Temperature Profile: @(t)20*square(0.01*2*pi*(t+99.98),50)+4
Antisolvent Profile: @(t)0*t

Thermodynamics and substance properties
Solubility function: @(T,xm)0.129*exp(0.0194*T)
Crystal density: 1.26e-15
Shape factor: 0.797

Kinetics
Growth rate: @(S,T,y)(S>=1)*((2.26e8/60)/(((0.129*ex
Nucleation rate: @(S,T,m)(S>=1)*((10.6/60)*exp(-16*pi*(2

Solver settings
Time: linspace(0,801,40050)
Solution method: Hires
Options:

Run

Figure A2.1: GUI interface for CAT solver

- Initial settings: CAT system default particle size distribution caused the solver to converge consistently and yielded realistic outputs, so simulations were structured around this condition. Concentration was chosen as the equilibrium condition at the initial temperature to remove any uncontrolled artifacts related to transience at the start of the simulation. A mass balance was performed around the particle size distribution to determine the seed mass and solution mass required to fully dissolve the solid phase when equilibrated at the highest temperature condition.

- Process settings: Antisolvent profile was set to 0 since this study focused solely on cooling crystallization. The temperature profile was constructed using the square function in MATLAB with an offset to set the low temperature to $20\ °C$.
- Thermodynamic and substance properties: Solubility was extracted from a plot found in literature for paracetamol dissolved in ethanol. Crystal density was converted to the proper units. Shape factor was also referenced from literature.
- Kinetics: Growth rate incorporated both growth and dissolution with the stipulation that growth could only occur for supersaturation values greater than or equal to 1, and dissolution could only occur for supersaturation values less than 1. Similarly, nucleation is composed of primary and secondary nucleation that could only occur for supersaturation levels greater than or equal to 1.

NUCLEATION KINETICS

Secondary nucleation is a function of both supersaturation and crystal mass as depicted in the following figures:

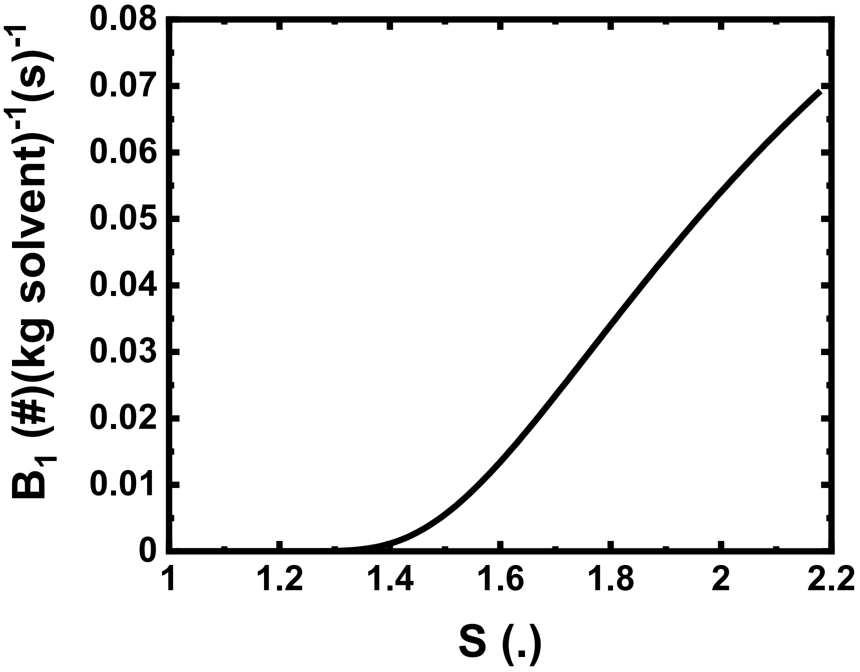

Figure A2.2: Primary nucleation kinetics as a function of supersaturation.

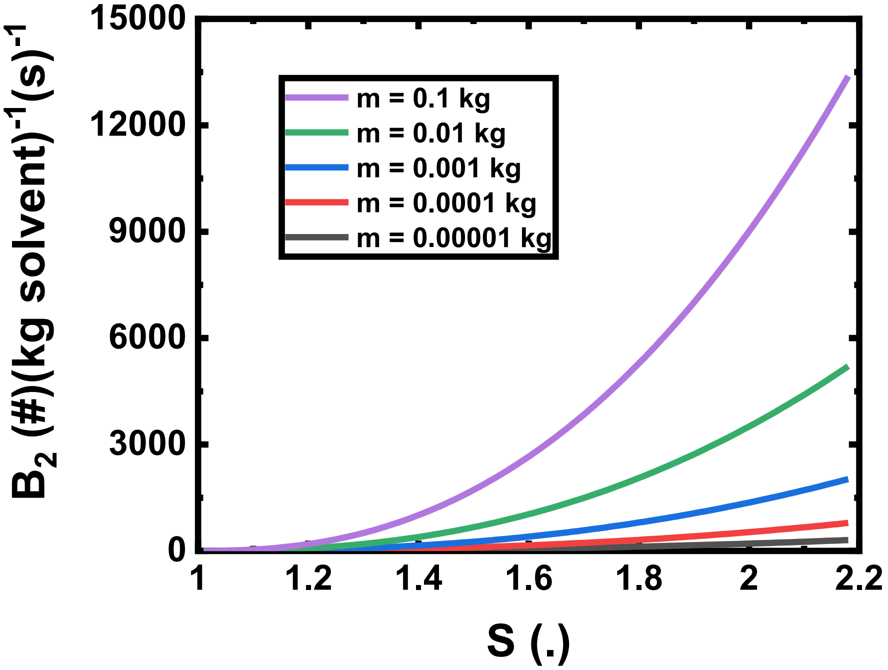

Figure A2.3: Secondary nucleation kinetics as a function of supersaturation for a family of crystal masses.

THERMAL CYCLING PARTICLE SIZE DISTRIBUTION RESULTS

PARTICLE SIZE DISTRIBUTIONS FOR HYPOTHESIS 1

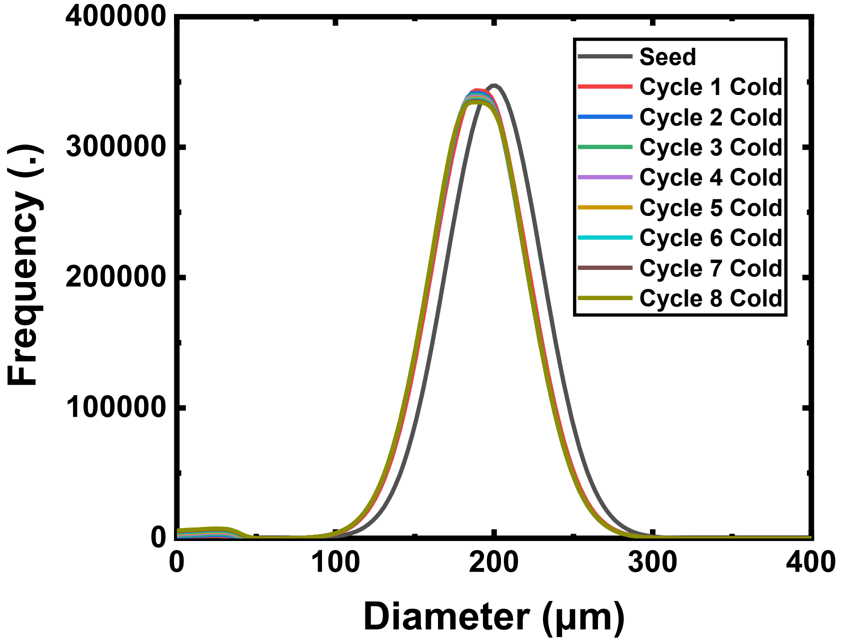

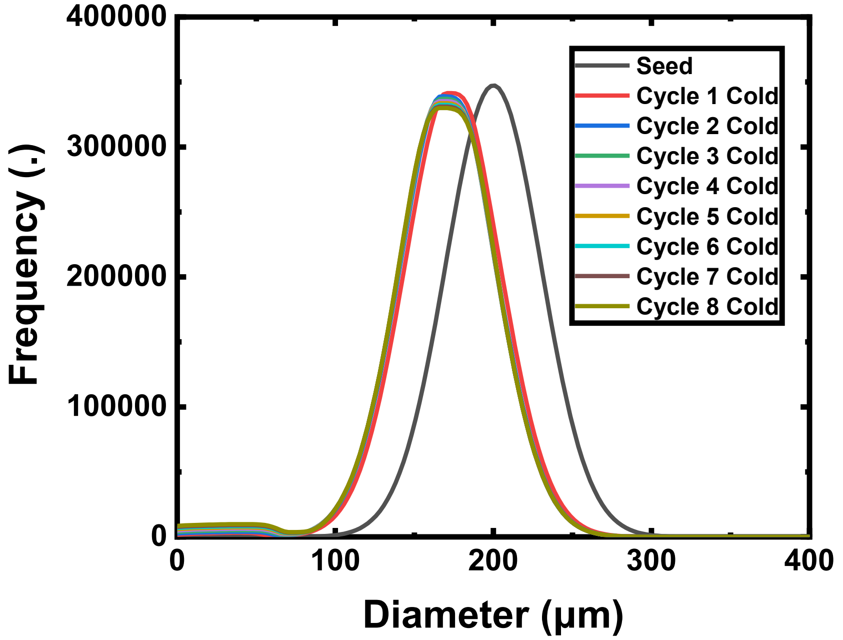

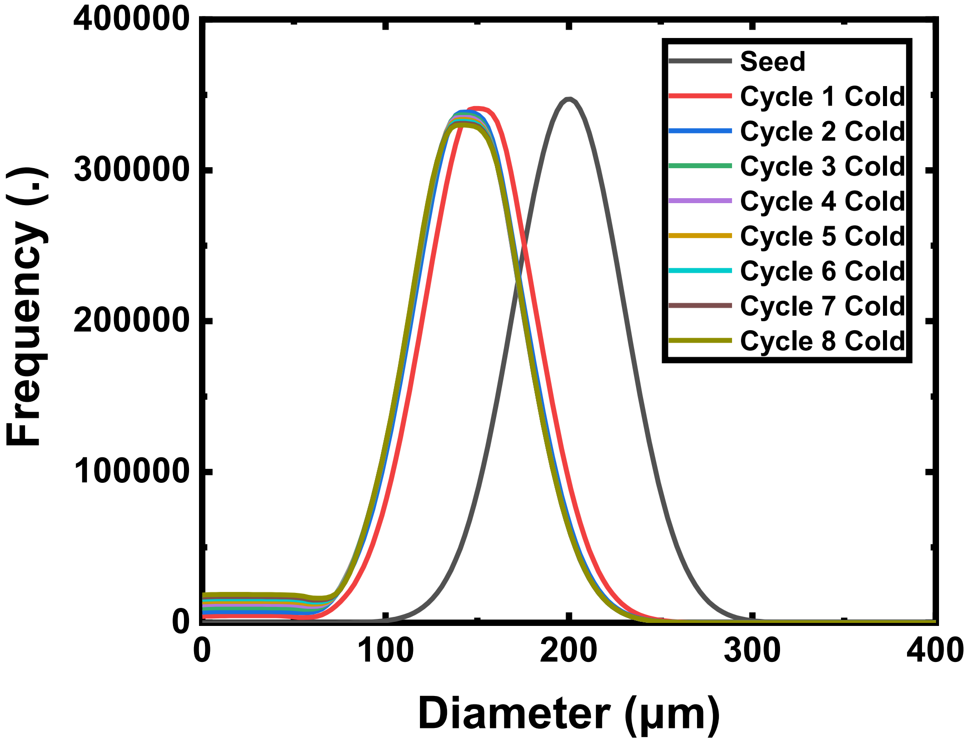

Frequency (.)
400000
300000
200000
100000
0
0
100
200
300
400
Diameter (μm)
Seed
Cycle 1 Cold
Cycle 2 Cold
Cycle 3 Cold
Cycle 4 Cold
Cycle 5 Cold
Cycle 6 Cold
Cycle 7 Cold
Cycle 8 Cold

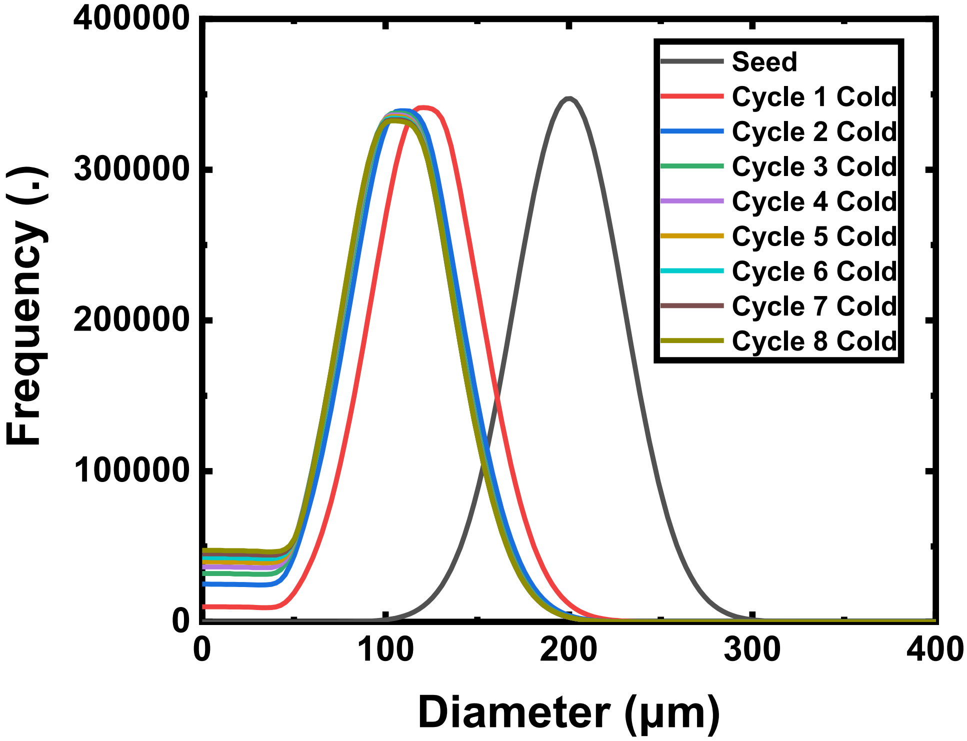

Frequency (.)
400000
300000
200000
100000
0
0
100
200
300
400
Diameter (μm)
Seed
Cycle 1 Cold
Cycle 2 Cold
Cycle 3 Cold
Cycle 4 Cold
Cycle 5 Cold
Cycle 6 Cold
Cycle 7 Cold
Cycle 8 Cold

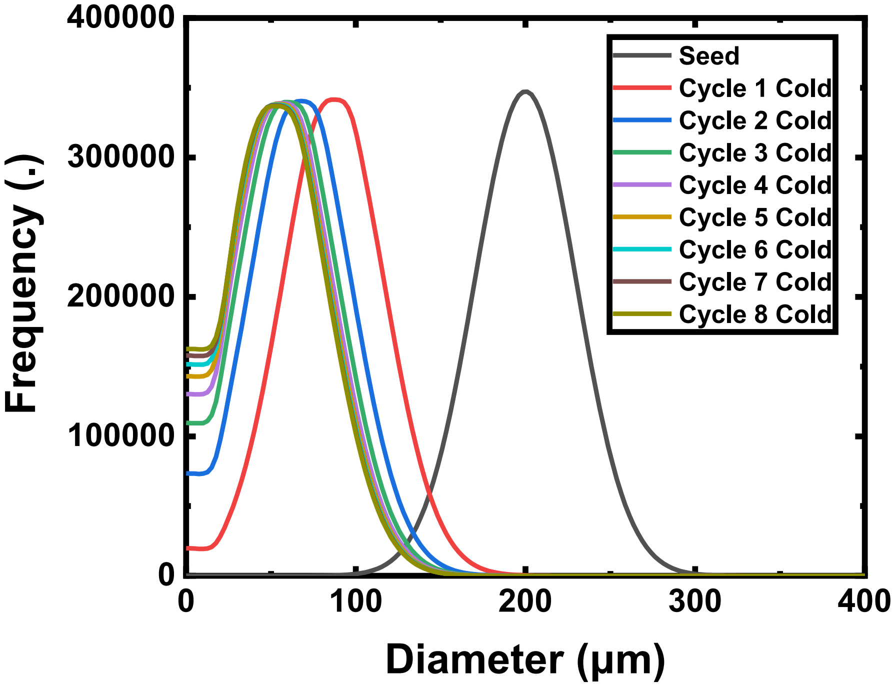

Figure A2.4: Cold cycle particle size distributions for duties $D = 10\ \%$ through $D = 90\ \%$. Frequency and amplitude are set constant at $f = 0.01\ Hz$ and $A = 20\ °C$, respectively.

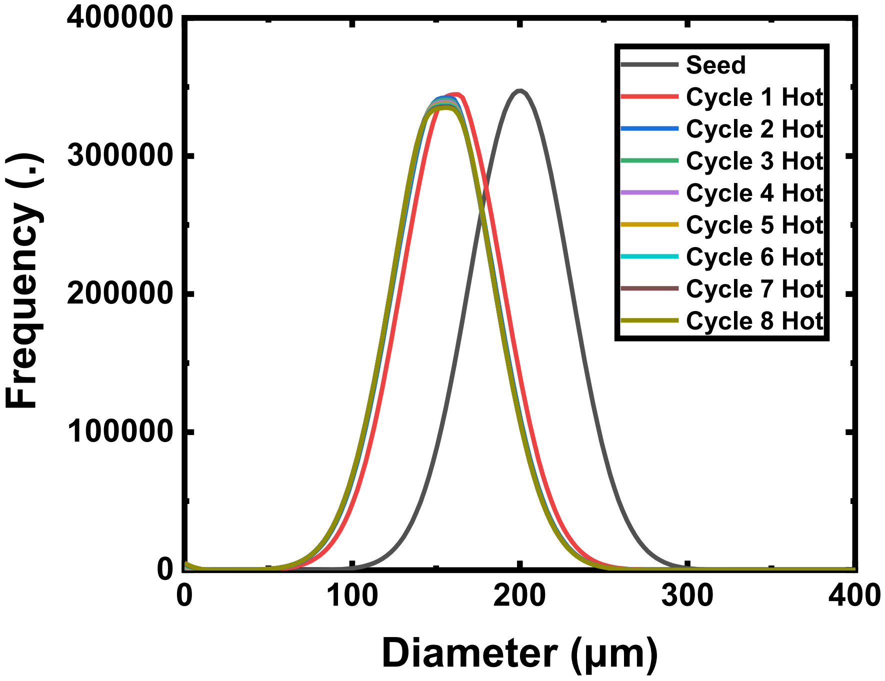

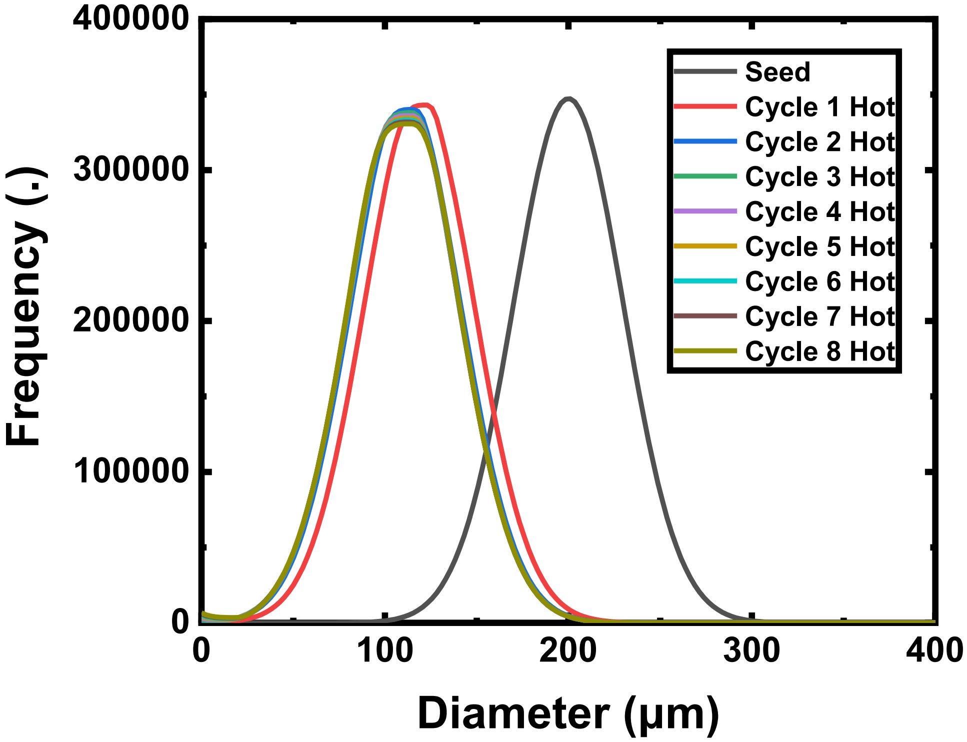

Frequency (.)
400000
300000
200000
100000
0
0
100
200
300
400
Diameter (µm)
Seed
Cycle 1 Hot
Cycle 2 Hot
Cycle 3 Hot
Cycle 4 Hot
Cycle 5 Hot
Cycle 6 Hot
Cycle 7 Hot
Cycle 8 Hot

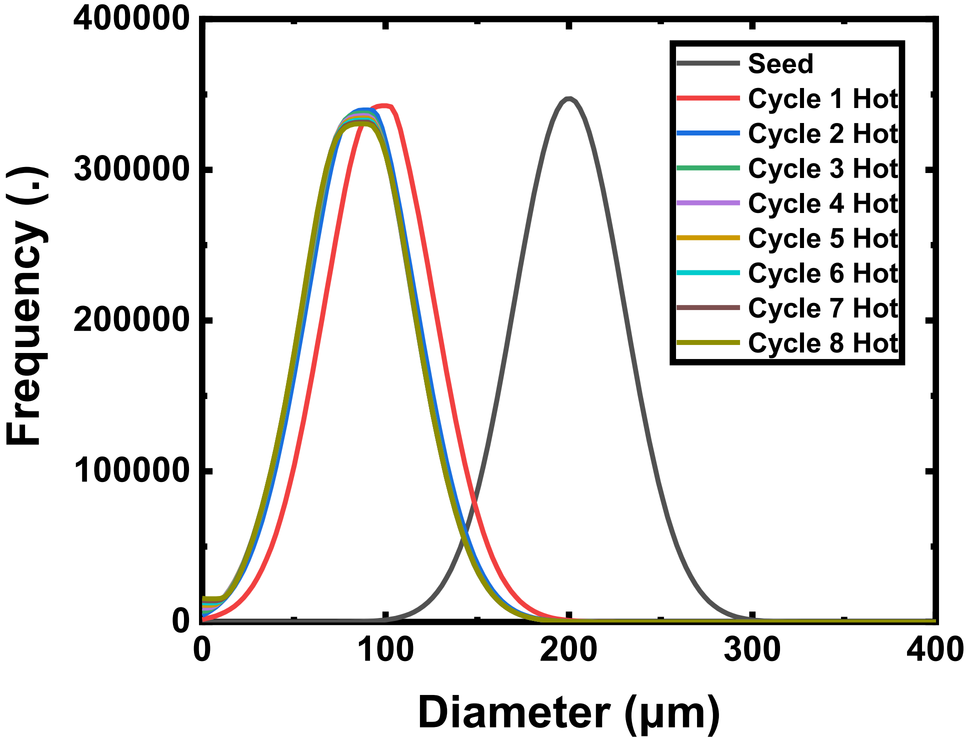

Frequency (.)
400000
300000
200000
100000
0
0
100
200
300
400
Diameter (µm)
Seed
Cycle 1 Hot
Cycle 2 Hot
Cycle 3 Hot
Cycle 4 Hot
Cycle 5 Hot
Cycle 6 Hot
Cycle 7 Hot
Cycle 8 Hot

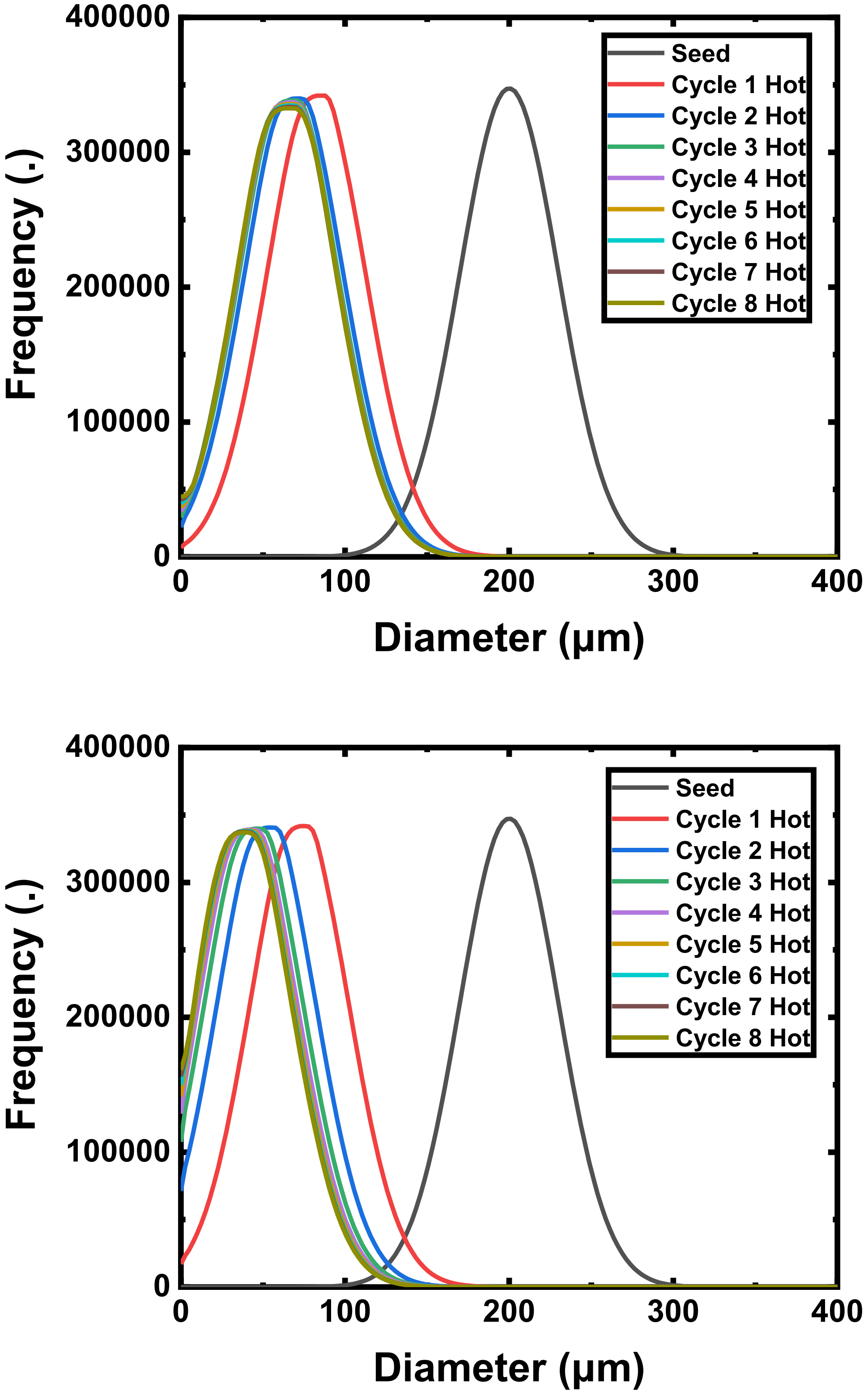

Figure A2.5: Hot cycle particle size distributions for duties $D = 10\ \%$ through $D = 90\ \%$. Frequency and amplitude are set constant at $f = 0.01\ Hz$ and $A = 20\ °C$, respectively.

PARTICLE SIZE DISTRIBUTIONS FOR HYPOTHESIS 2

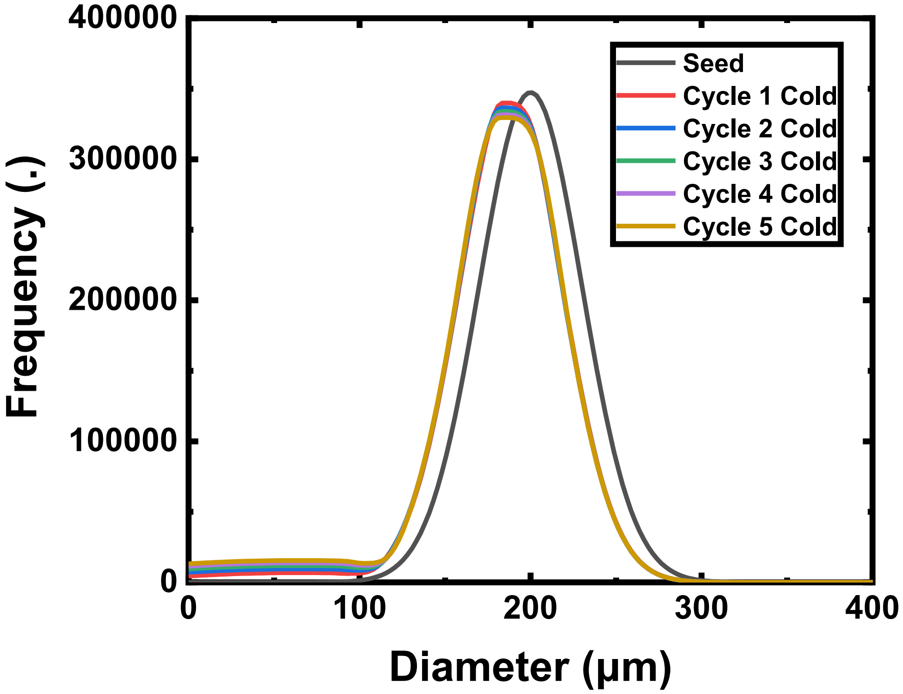

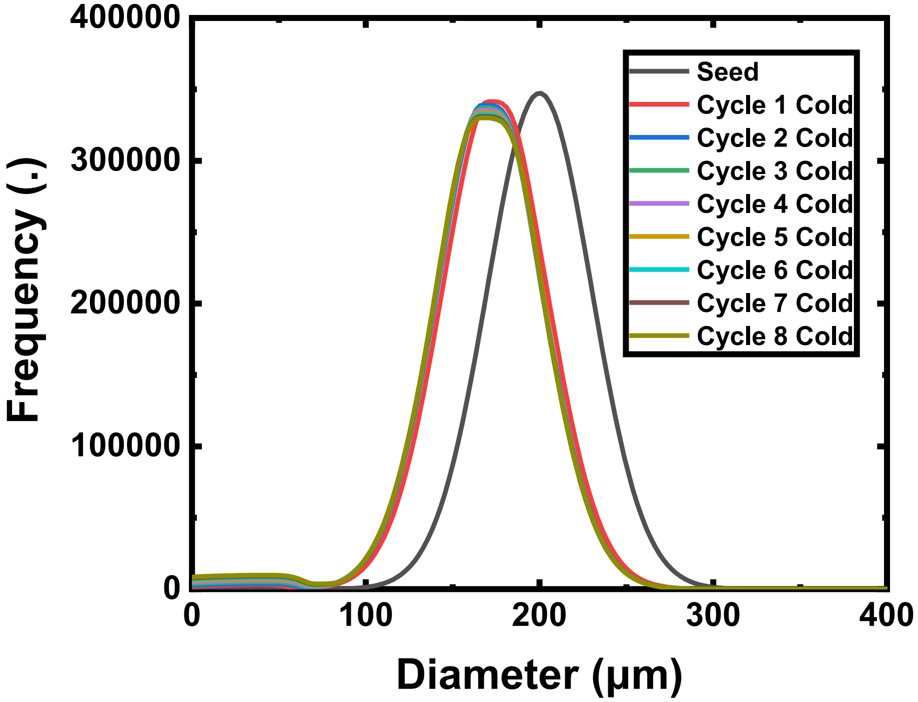

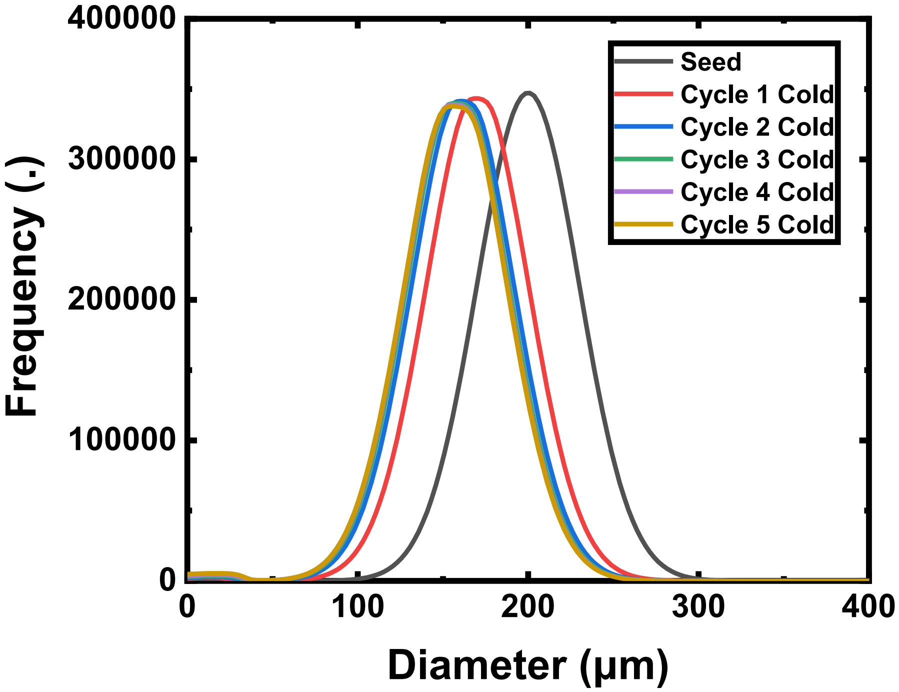

Figure A2.6: Cold cycle particle size distributions for frequencies $f = 0.005\ Hz$, $f = 0.01\ Hz$, and $f = 0.02\ Hz$. Duty and amplitude are set constant at $D = 30\ \%$ and $A = 20\ °C$, respectively.

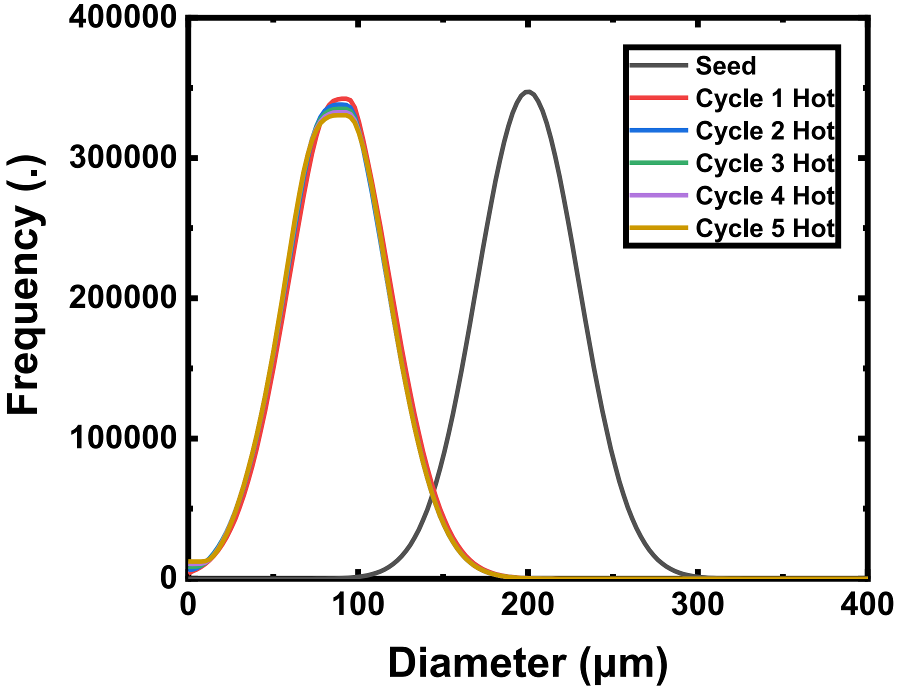

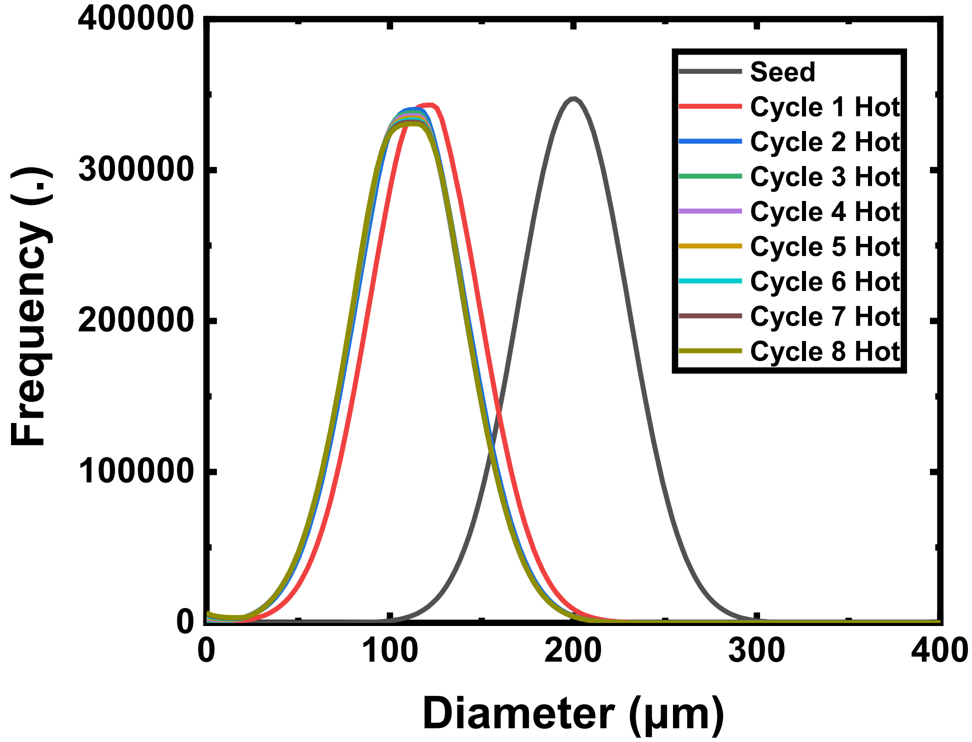
Frequency (.)
400000
300000
200000
100000
0
0
100
200
300
400
Diameter (µm)
Seed
Cycle 1 Hot
Cycle 2 Hot
Cycle 3 Hot
Cycle 4 Hot
Cycle 5 Hot
Cycle 6 Hot
Cycle 7 Hot
Cycle 8 Hot

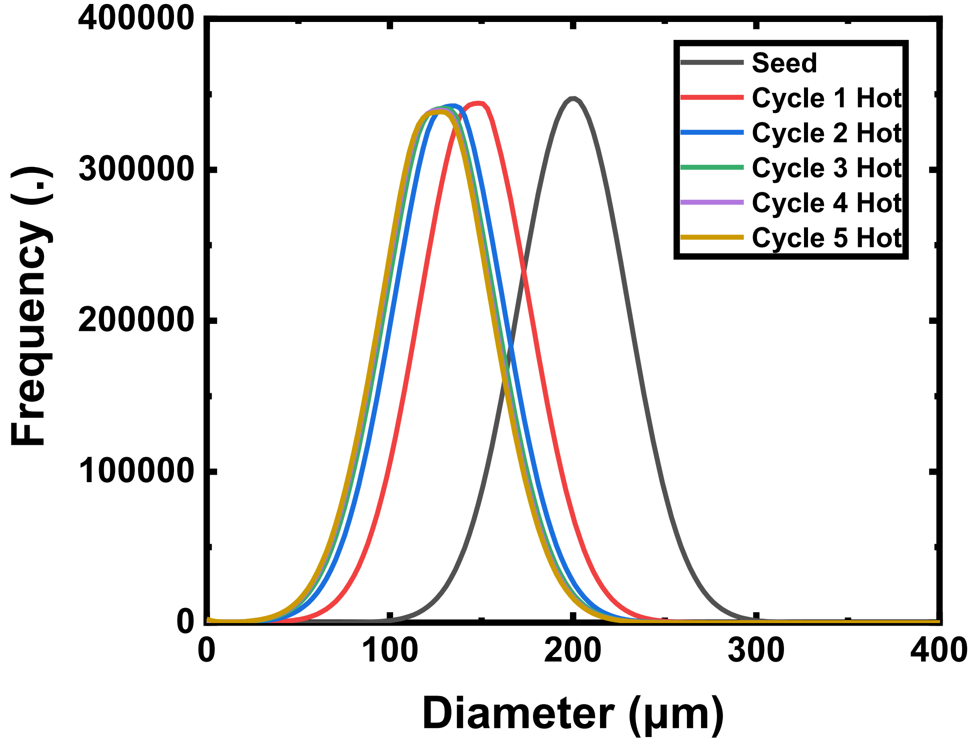
Frequency (.)
400000
300000
200000
100000
0
0
100
200
300
400
Diameter (µm)
Seed
Cycle 1 Hot
Cycle 2 Hot
Cycle 3 Hot
Cycle 4 Hot
Cycle 5 Hot

Figure A2.7: Hot cycle particle size distributions for frequencies $f = 0.005\ Hz$, $f = 0.01\ Hz$, and $f = 0.02\ Hz$. Duty and amplitude are set constant at $D = 30\ \%$ and $A = 20\ °C$, respectively.

PARTICLE SIZE DISTRIBUTIONS FOR HYPOTHESIS 3

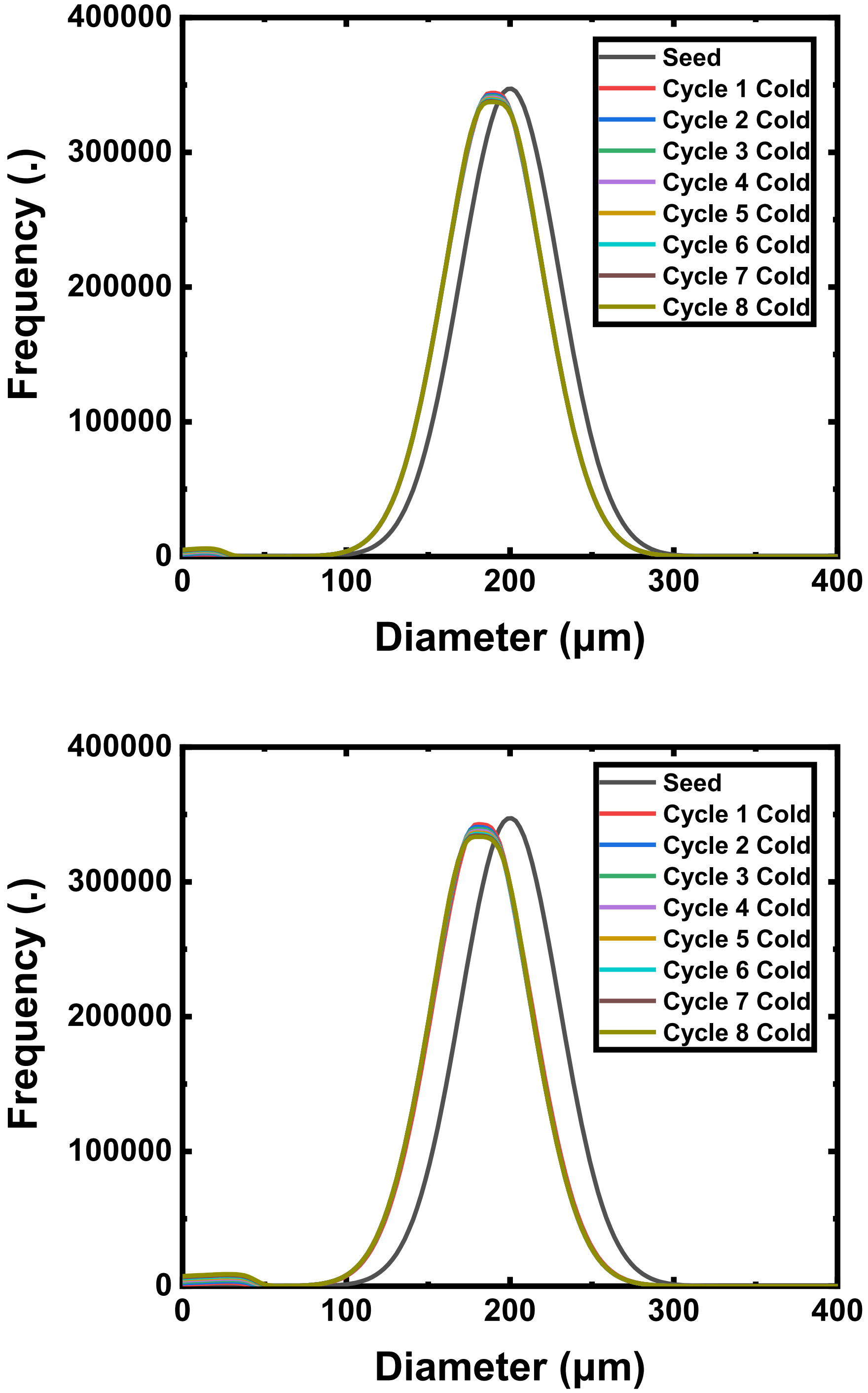

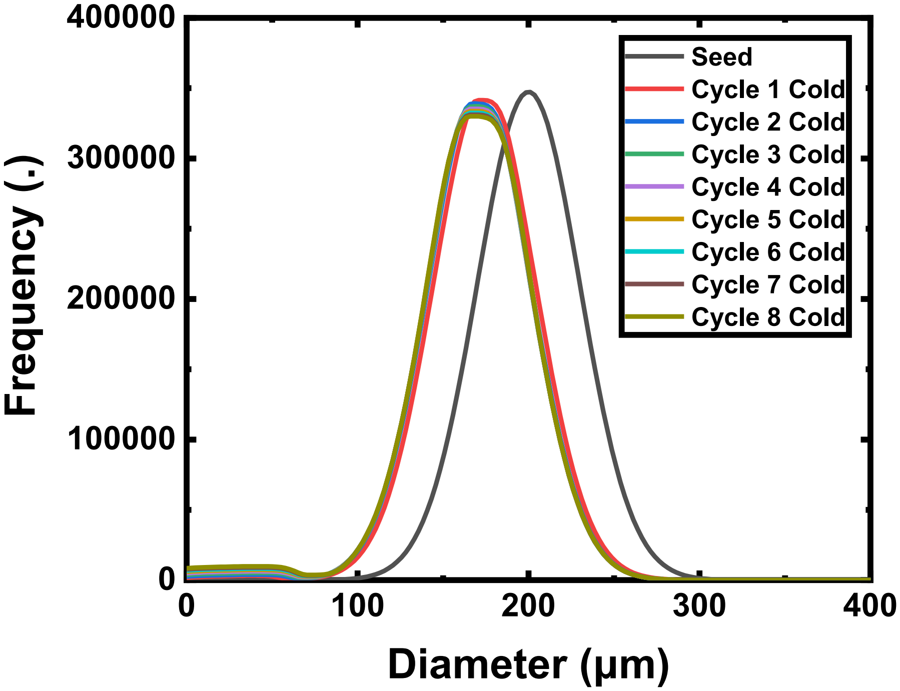

Figure A2.8: Cold cycle particle size distributions for amplitudes $A = 10\ °C$, $A = 10\ °C$, and $A = 20\ °C$. Duty and amplitude are set constant at $D = 30\ \%$ and $f = 0.01\ Hz$, respectively.

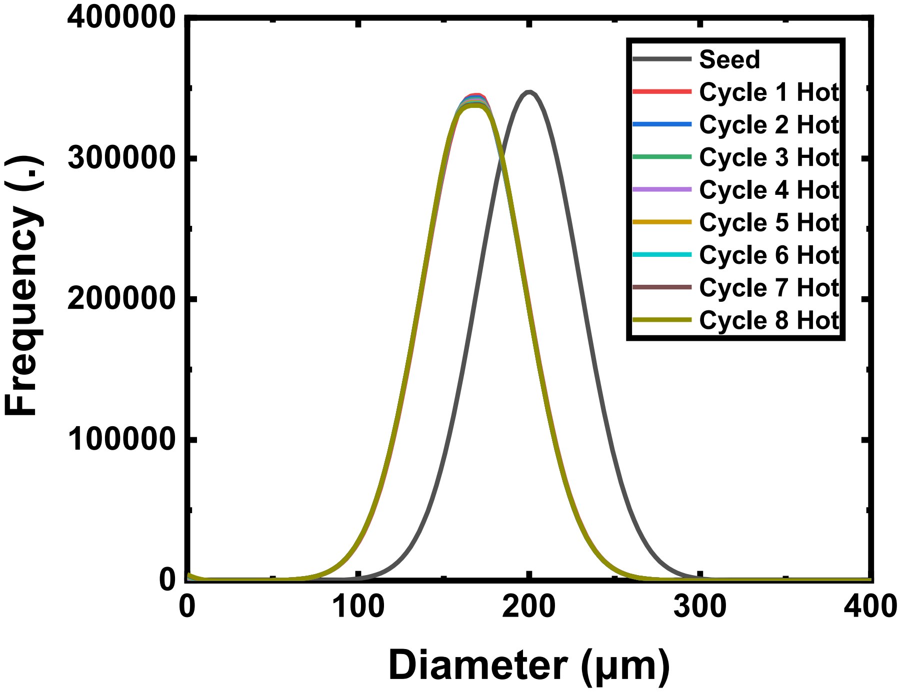

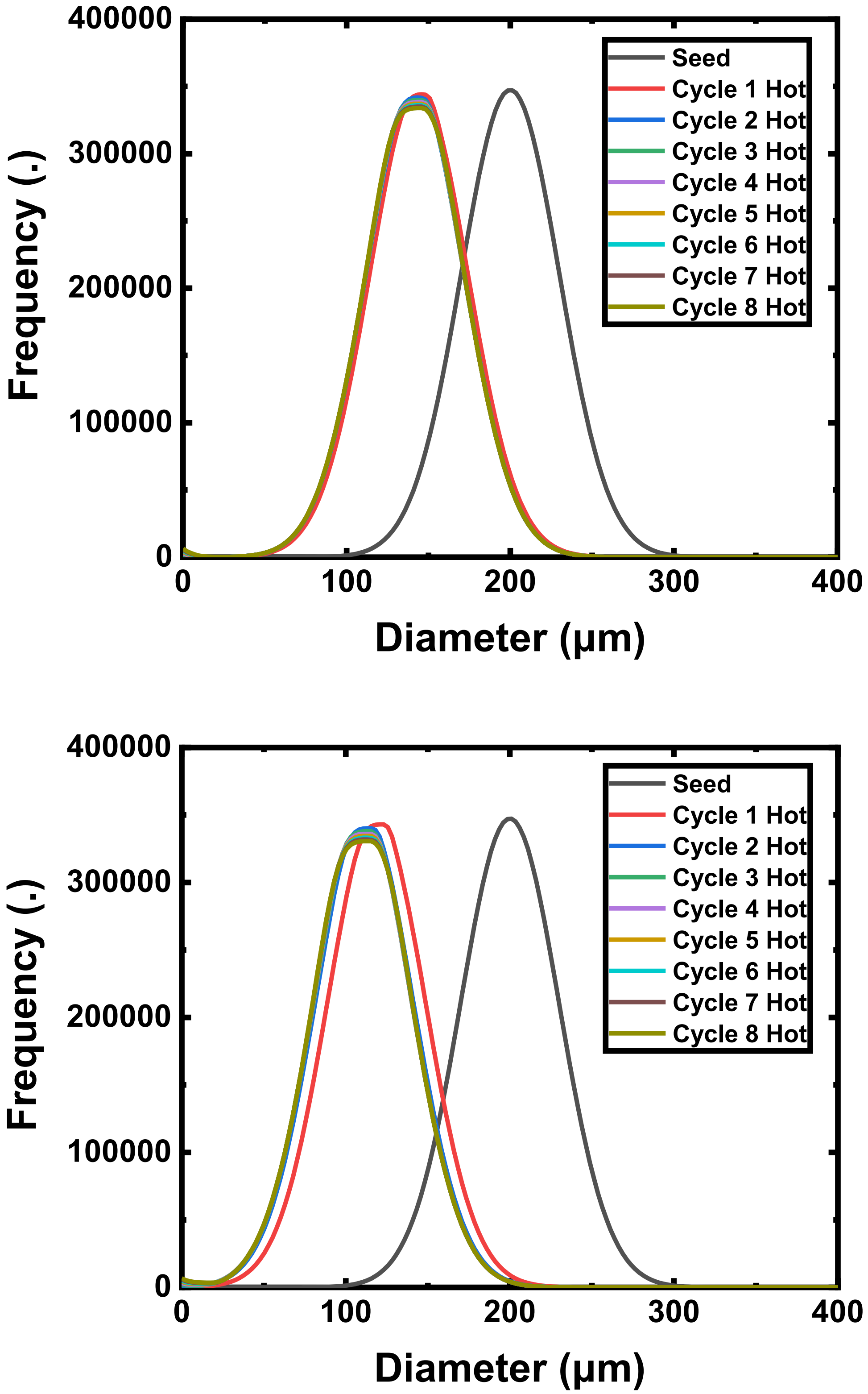

Figure A2.9: Hot cycle particle size distributions for amplitudes $A = 10\ °C$, $A = 10\ °C$, and $A = 20\ °C$. Duty and amplitude are set constant at $D = 30\ \%$ and $f = 0.01\ Hz$, respectively.

ISOTHERMAL DISSOLUTION KINETICS

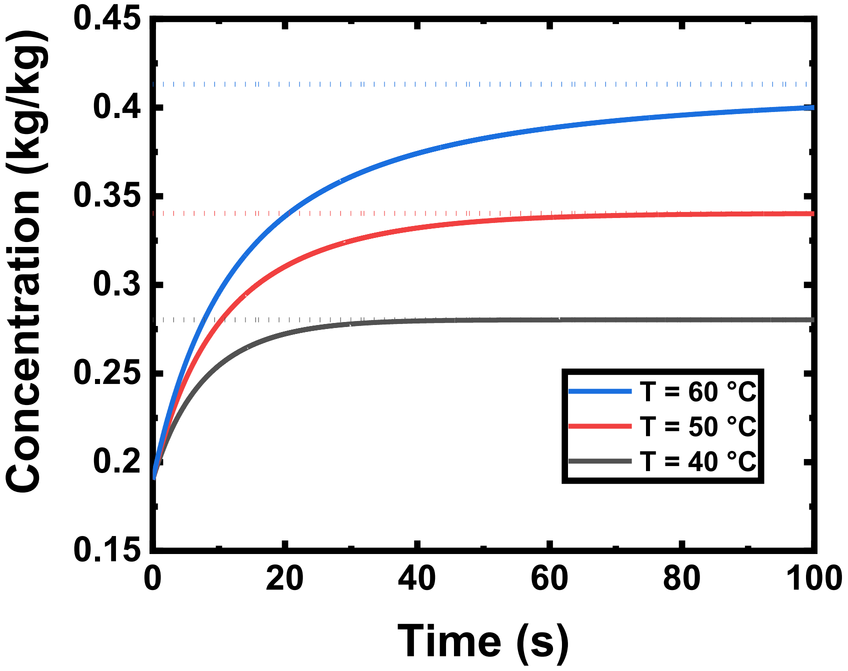

Figure A2.10: Isothermal dissolution kinetics for amplitudes $A = 10\ °C$, $A = 15\ °C$, and $A = 20\ °C$.